

1-1-2020

# Development Of Photoacoustic Tomographic Systems For Brain Hemorrhage Detection

Karl Kratkiewicz  
*Wayne State University*

Follow this and additional works at: [https://digitalcommons.wayne.edu/oa\\_dissertations](https://digitalcommons.wayne.edu/oa_dissertations)



Part of the [Bioimaging and Biomedical Optics Commons](#)

---

## Recommended Citation

Kratkiewicz, Karl, "Development Of Photoacoustic Tomographic Systems For Brain Hemorrhage Detection" (2020). *Wayne State University Dissertations*. 2453.  
[https://digitalcommons.wayne.edu/oa\\_dissertations/2453](https://digitalcommons.wayne.edu/oa_dissertations/2453)

This Open Access Embargo is brought to you for free and open access by DigitalCommons@WayneState. It has been accepted for inclusion in Wayne State University Dissertations by an authorized administrator of DigitalCommons@WayneState.

**DEVELOPMENT OF PHOTOACOUSTIC TOMOGRAPHIC SYSTEMS FOR BRAIN  
HEMORRHAGE DETECTION**

by

**KARL JOHN KRATKIEWICZ**

**DISSERTATION**

Submitted to the Graduate School

of Wayne State University,

Detroit, Michigan

in partial fulfillment of the requirements

for the degree of

**DOCTOR OF PHILOSOPHY**

2020

MAJOR: BIOMEDICAL ENGINEERING

Approved By:

---

Advisor

---

Date

---

---

---

---

## **DEDICATION**

Without the support of the following people, the work performed to culminate in this final dissertation would never have been possible.

To my parents, John and Christine Kratkiewicz, for your unconditional love and support. You were my role models to learn how to be responsible and diligent in my work. This has shaped me into who I am today and has kept me strong in my pursuit of new knowledge. To my brothers, Jake and Kyle Kratkiewicz, who have always been my comic relief. Whenever stress felt high, I knew I could turn to them to keep me stable and smiling.

I also dedicate this to my grandparents, Robert and Marion Lemke and Norbert and Alice Kratkiewicz. They have always pushed me to be the best that I could be. Through praise in success or support in failure, they have helped me reach goals I had never thought possible.

I dedicate this to my fiancée's family, Igor, Inna, Brendan, and Sean Beim, who have treated me like family through all of this time. Always celebrating my progress through this journey and supporting me in any way they can.

Finally, this work is a direct result of the love and companionship of my fiancée, Jane Beim. You have been by my side through my entire college career, supporting all of my decisions. We have been through this all together and this success is as much yours as it is mine.

## **ACKNOWLEDGEMENTS**

Throughout this Ph.D. journey I have had the privilege of working with some brilliant investigators who have shaped the way that I perform research.

Firstly, to my advisor, Dr. Kamran Avanaki, for his tireless effort in guiding my research. He has helped me grow to become an independent researcher who asks the right questions first and emphasizes sound experimental design before trying to find the answers to those questions. He has always sought out research events to give me opportunity to disseminate my work and improve my presentation skills. Without him, I would not have had the ability to understand professionalism in research.

I also want to thank my fellow lab colleagues, Dr. Rayyan Manwar, Qiuyun Xu, and Mohsin Zafar. Their collaboration amongst a range of projects has given me a wider understanding of my research area that I would not have been able to achieve on my own. They provided tireless assistance with working various devices and developing experimental setups. Many parts of this work were not possible without them.

Many thanks to my committee members, Dr. Eishi Asano, Dr. Chaoyang Chen, Dr. Gholam-Abbas Nazri, and Dr. Zhifeng Kou. They have provided me feedback on my research design and timeline of experiments to facilitate my work. They have also provided collaboration and insights that improved our experimental design.

To collaborators Sadreddin Mahmoodkalayeh and Mohsen Ranjbaran who have provided guidance and aided in many of the studies during my graduate career.

I also must thank a mentor, Dr. Juri Gelovani, who provided the foundation and guidance for much of Chapter 4 of this work.

## TABLE OF CONTENTS

Dedication .....	ii
Acknowledgements .....	iii
List of Tables .....	viii
List of Figures .....	ix
CHAPTER 1: INTRODUCTION .....	1
1.1 Photoacoustic imaging development .....	1
1.2 Scientific gap and objectives .....	3
1.3 Major contributions and outline .....	4
CHAPTER 2: OVERVIEW ON LINEAR ARRAY-BASED PHOTOACOUSTIC IMAGING .....	7
2.1 Introduction .....	7
2.2 Software and hardware setup .....	7
2.2.1 Script analysis .....	7
2.2.2 Transducer setup .....	10
2.2.3 US/PA sequencing .....	13
2.2.4 US/PA experimental setup .....	15
2.3 Experimental setup considerations .....	17
2.3.1 Synchronization .....	17
2.3.2 Frame averaging .....	19
2.3.3 Illumination angle .....	19
2.3.4 Modifying sampling rate .....	20
2.3.5 US/PA simultaneous display .....	22
2.3.6 Comparing US and PA signals received by the transducer .....	25

2.3.7 US/PA image resolution analysis .....	26
2.3.8 US image quality improvement through beam steering .....	28
2.3.9 Photoacoustic signal amplification .....	30
2.3.10 Fluence compensation .....	33
2.3.11 Water as photoacoustic imaging couplant .....	35
2.4 PA Image reconstruction .....	36
2.4.1 Evolution of PA image reconstruction algorithms.....	36
2.4.2 Evaluation of performance of DS-DMAS algorithm .....	38
2.5 Discussion and conclusions.....	40
CHAPTER 3: A NOVEL METHOD TO AVOID THERMAL DAMAGE IN PHOTOACOUSTIC IMAGING .....	42
3.1 Introduction.....	42
3.2 Materials and methods .....	45
3.3 Results.....	48
3.3.1 In vivo experiments .....	48
3.3.2 Simulation results.....	51
3.4 Discussion and conclusions.....	54
CHAPTER 4: DEVELOPMENT OF TRANSFONTANELLE PHOTOACOUSTIC IMAGING.....	56
4.1 Introduction.....	56
4.2 Materials and methods .....	59
4.2.1 Equipment specifications and Wavelength Selection.....	59
4.2.2 Development of simulation model .....	61
4.2.3 Blood fluence decay curve quantification .....	65

4.2.4 Probe resolution analysis .....	67
4.2.5 Sensitivity analysis .....	68
4.2.6 Oxygen saturation measurement .....	68
4.2.7 Ex-vivo sheep brain hemorrhage imaging study .....	70
4.2.8 Vessel rupture and edema detection using Evans Blue contrast agent.....	71
4.3 Results.....	73
4.3.1 Light delivery optimization through simulation .....	73
4.3.2 Blood fluence decay curve quantification .....	78
4.3.3 Probe resolution analysis .....	79
4.3.4 Sensitivity analysis .....	81
4.3.5 Oxygen saturation measurement .....	82
4.3.6 Ex-vivo sheep brain hemorrhage imaging study .....	85
4.3.7 Vessel rupture and edema detection using Evans Blue contrast agent.....	87
4.4 Discussion and conclusions.....	89
CHAPTER 5: TOWARD 3-DIMENSIONAL PHOTOACOUSTIC IMAGING FOR IMPROVED HEMORRHAGE DETECTION .....	93
5.1 Introduction.....	93
5.2 Materials and methods .....	96
5.2.1 Simulation study.....	97
5.2.2 Experimental setup .....	102
5.3 Results.....	105
5.3.1 Simulation results.....	105
5.3.2 Experimental results .....	108

5.3.3 System calibration.....	110
5.4 Discussion and conclusions.....	112
CHAPTER 6: CONCLUSIONS AND FUTURE WORK.....	116
6.1 Conclusions.....	116
6.2 Future Work.....	118
Appendix .....	120
References.....	123
Abstract.....	150
Autobiographical Statement .....	152



## LIST OF TABLES

Table 1. Specifications of linear array transducers.....	11
Table 2. Modifications to recognize new probes .....	11
Table 3. Recognizable transducers .....	12
Table 4. High frequency Vantage 128 system specifications .....	15
Table 5. Sampling rate script modifications.....	21
Table 6. 2 window display script modifications.....	23
Table 7. Reconstruction algorithm performance comparison .....	38
Table 8. Thermal simulation parameters used .....	48
Table 9. Laser irradiation process and biopsy results .....	50
Table 10. Different 3D PA signal detection configuration .....	95
Table 11. 3D HA-PACT System specification .....	103
Table 12. Estimated cost of the proposed system.....	114

## LIST OF FIGURES

Figure 1. Photoacoustic principle .....	2
Figure 2. Simplified system architecture of the Vantage Research System .....	14
Figure 3. Timing diagram of US/PA sequencing in Vantage .....	15
Figure 4. Example time-domain and frequency domain PA signal .....	16
Figure 5. Photoacoustic signal “jitter” comparison.....	18
Figure 6. PA signal SNR improvement with averaging.....	19
Figure 7. Importance of illumination angle.....	20
Figure 8. Signal quality of different sampling rates.....	22
Figure 9. Comparing absolute magnitude of PA and US signal .....	26
Figure 10. US/PA resolution study .....	28
Figure 11. US image quality with increasing number of steered angles .....	30
Figure 12. PA signal amplification .....	32
Figure 13. Fluence Compensation algorithm validation.....	34
Figure 14. Analysis of water optical absorption spectrum .....	36
Figure 15. Block diagram of DS-DMAS algorithm .....	38
Figure 16. DS-DMAS reconstruction against Verasonics standard US and PA .....	39
Figure 17. Temperature rise profile in biological tissue due to laser exposure.....	43
Figure 18. Thermal imaging setup.....	45
Figure 19. Absorption and scattering coefficients of skin .....	47
Figure 20. No cooling irradiation results .....	49
Figure 21. Irradiation with cooling results .....	50
Figure 22. 532nm experimental/simulation comparison .....	51

Figure 23. Simulation results for varied pulse repetition rate and pulse energy .....	53
Figure 24. Simulation results for various heat transfer coefficients .....	54
Figure 25. TFMPI probe and associated optics .....	60
Figure 26. Example TFMPI optical fiber configurations .....	63
Figure 27. Blood fluence decay experimental setup .....	67
Figure 28. Light microscopy image of human hair for resolution study .....	68
Figure 29. TFMPI Simulation Study .....	77
Figure 30. Fluence decay characterization of the TFMPI probe .....	79
Figure 31. Point spread function characterization for axial and lateral resolution .....	80
Figure 32. TFMPI resolution summary .....	81
Figure 33. TFMPI and US blood sensitivity .....	82
Figure 34. Oxygenation evaluation summary .....	83
Figure 35. More detailed oxygenation data .....	84
Figure 36. Ex vivo feasibility study of the TFMPI in detecting pseudo-hemorrhage model .....	86
Figure 37. Evaluation of use of Evan's Blue to identify edema .....	88
Figure 38. Hemispherical simulation results .....	107
Figure 39. Hemispherical experimental results .....	109
Figure 40. Optimization of single element spatial location .....	111
Figure 41. Other simulations of varying number and sized transducer elements on reconstruction quality .....	113

## **CHAPTER 1: INTRODUCTION**

In section 1.1, the photoacoustic modality is introduced and explained with respect to biomedical photoacoustic imaging. Section 1.2 describes the scientific gap and objectives of this research. Section 1.3 discusses the major contributions that this dissertation presents from system and probe designs to reconstruction developments and applications, as well as provides an outlines for the entire dissertation.

### **1.1 Photoacoustic imaging development**

Photoacoustic imaging (PAI), also called optoacoustic imaging, is a three-dimensional (3-D) imaging modality, working based on photoacoustic (PA) effect [1]. The sample (light absorbent) to be imaged is optically excited, leading to a transient temperature rise, resulting in a thermoelastic expansion of the absorber followed by emission of acoustic waves. The absorber could be an endogenous protein such as hemoglobin, myoglobin, melanin, or an exogenous contrast agent such as nano particles or dyes [2]. The emitted acoustic waves from the absorber are eventually detected by ultrasound (US) transducers. The transducer signals are then given to an image reconstruction algorithm to generate the absorption map of the tissue. The PAI process steps are illustrated in Figure 1.

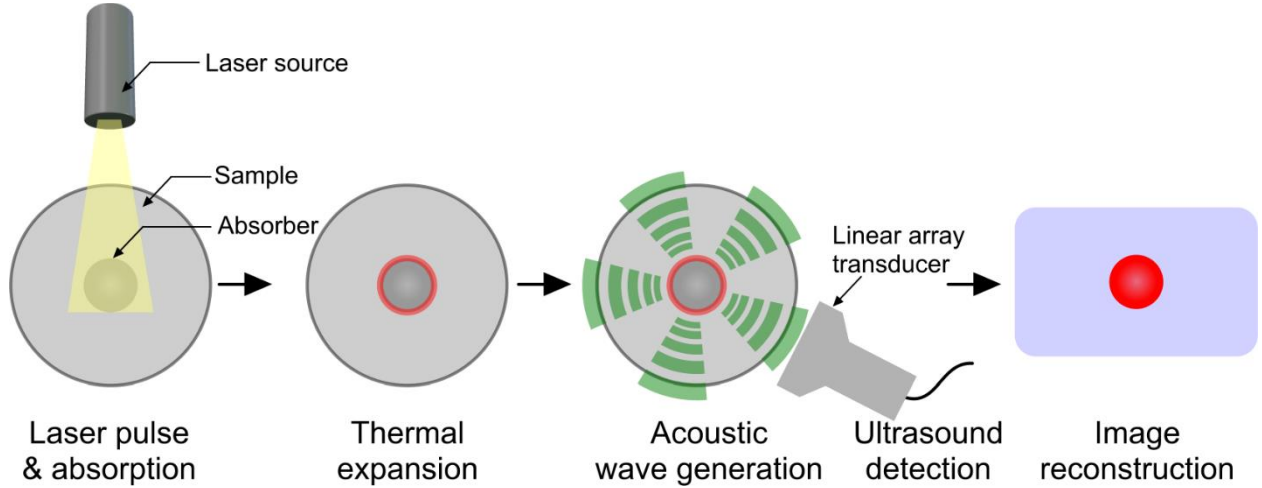


**Figure 1. Photoacoustic principle.** Principle of PA signal generation, detection, and image reconstruction.

Due to strong optical scattering, pure optical imaging modalities have a shallow imaging depth in biological tissues [1, 3]. Acoustic waves experience far less tissue scattering, thus they propagate a greater distance [4, 5]. Although ultrasound imaging can image deep biological tissues with a high spatial resolution, its acoustic contrast is incapable of providing certain physiological parameters. In PAI, optical excitation travels within the tissue far beyond the diffusion limit, i.e., optical quasi-diffusive or diffusive regimes, and generates acoustic waves. Sensitivity of PAI in deep tissues is orders of magnitude higher than that of pure optical imaging modalities [6]; the highest penetration depth reported is ~12 cm [7-9].

PAI is an ideal modality for measuring/monitoring tissue physiological parameters by imaging the concentration of tissue chromophores [10], which are changed during the course of a disease [11]. PAI has been evaluated in preclinical and recently clinical applications for disease detection and monitoring purposes [12-29]. For instance, it has been used to study human skin abnormalities [30-32], brain disease detection [33, 34],

human breast tumor detection [11, 35-38], retina disease diagnosis [39, 40], and atherosclerosis evaluation of vessel walls [22, 41, 42].

## **1.2 Scientific gap and objectives**

Preterm neonates (<32 weeks gestational age) and/or with low birth weight (<1500g) are at high risk for intracranial hemorrhage (ICH) with the incidence of 30%-35% [1]. TransFontanelle Ultrasound Imaging (TFUSI) is a routine diagnostic brain imaging method for infants younger than 6 months, whose skull bones have fontanelles [2-4]. Open fontanelles provide acoustic windows, allowing the ultrasound beam to freely pass through [5]. TFUSI is widely used due to its low cost, safety, accessibility, and noninvasive nature [6-8]. Nevertheless, the accuracy of TFUSI is limited. Up to 85% of survivors of neonatal brain hemorrhage will exhibit major cognitive dysfunction. Magnetic resonance imaging (MRI) [9, 10], computed tomography (CT) [11], and positron emission tomography (PET) [12] also have limited implementation in neonatal intensive care unit (NICU) patients. Near infrared spectroscopy (NIRS) can potentially assist clinicians in assessing functional changes in cerebral perfusion and oxygenation [13-15], but it has a poor spatial resolution, especially for the small neonate head, and a poor penetration depth, which both limit its use to cortical mapping [16]. Therefore, there is a clinical need to develop novel imaging methods for early diagnosis of preterm infant hemorrhage. Improved diagnosis will hasten treatment and potentially limit neurological deficit in the patient.

To address several limitations of current clinical neuroimaging, we aim to develop 2 photoacoustic systems for preterm neonatal hemorrhage detection. One system being a novel TransFontanelle Multispectral Photoacoustic Imaging (TFMPI) method. TFMPI

can be used for parametric imaging of brain perfusion-oxygenation in a manner similar to blood-oxygen-level dependent (BOLD) imaging in functional MRI [17-19]. The other being a 3D hemispherical array photoacoustic computed tomography (HA-PACT) system for 3D volumetric imaging of infant brain.

Further, prior to development of these novel systems, we investigate utility of a common preclinical photoacoustic platform and confirm its performance for our specific purposes. We also investigate safety of PAI for thermal tissue damage in a mouse model.

The long-term goal of this research is to provide a cost-effective, portable, point-of-care diagnostic imaging method for neonates with potential for ICH. Our central hypothesis is that both systems will provide improved, clinically relevant, diagnostic information over the current neonatal ultrasound imaging systems; improving point-of-care diagnosis, leading to an earlier postnatal intervention and improved management of ICH in neonates.

### **1.3 Major contributions and outline**

To align with the scientific gap we have observed, we have been actively investigating methods of translating photoacoustic imaging to the clinic for hemorrhage detection. The major contributions can be broken down into the following where this order is followed throughout the remainder of this dissertation:

- **Verasonics Vantage system comprehensive review.** Here, we precisely define all aspects of implementing a photoacoustic imaging linear array system in Verasonics architecture, a common preclinical photoacoustic imaging platform. This includes hardware and software discussion. Experimental design is

discussed with a myriad of considerations – laser synchronization, frame averaging, illumination angle onto sample, display methods, US beam steering for improving reconstruction, 3<sup>rd</sup> party PA amplifier hardware for improving sensitivity, fluence compensation, and water as a PA couplant. We then characterized one of our systems and discuss image reconstruction.

- **Photoacoustic thermal Safety assessment.** Here, we evaluate thermal safety of photoacoustic imaging on mouse model. We briefly discuss a bio-heat transfer model. Thermal damage of irradiated spot was assessed by histology following biopsy for different pulse repetition rate lasers (10Hz and 30Hz) for different durations (20s, 60s, 300s). Efficacy of using cooling bag during laser irradiation for improved thermal damage result was evaluated. Results of skin temperature increase throughout irradiation is compared to simulation.
- **Development of TransFontanelle Multi-spectral Photoacoustic Imaging (TFMPI) probe for neonatal hemorrhage detection.** Here, we discuss linear array TFMPI probe development including light delivery optimization through optical simulation. We investigated fluence decay estimation of blood at various imaging depths. We characterize our probe for resolution throughout the imaging window. Experimentally we determine the sensitivity of PA to low blood concentrations compared to US to demonstrate sensitivity to detecting hemorrhage. We then create an intraventricular hemorrhage model in *ex-vivo* sheep head and demonstrated ability of detection. Finally, we demonstrate ability to differentiate edematous regions from hemorrhage through use of exogenous contrast agent Evan's Blue.



- **3D hemispherical array photoacoustic computed tomography (HA-PACT).**

Here, we investigated how element number effected reconstruction quality in terms of contrast to noise ratio (CNR) equidistantly spaced around a hemispherical array. We further evaluated image quality amongst multiple reconstruction methods. We experimentally imaged two *in-vitro* phantoms to confirm feasibility of 3D imaging within the hemisphere as well as compare two methods of illumination technique (single fiber overhead versus homogenous fiber bundle). We also implement a continuous sequential algorithm for element spatial placement optimization within the reconstruction.

## **CHAPTER 2: OVERVIEW ON LINEAR ARRAY-BASED PHOTOACOUSTIC IMAGING**

In this Chapter, we precisely define all aspects of implementing a photoacoustic imaging linear array system in Verasonics architecture, a common preclinical photoacoustic imaging platform. This includes hardware and software discussion. Experimental design is discussed with a myriad of considerations – laser synchronization, frame averaging, illumination angle onto sample, display methods, US beam steering for improving reconstruction, 3<sup>rd</sup> party PA amplifier hardware for improving sensitivity, fluence compensation, and water as a PA couplant. We then characterized one of our systems and discuss image reconstruction.

### **2.1 Introduction**

In recent years, many researchers have used the Vantage Verasonics® system for simultaneous ultrasound (US) and photoacoustic (PA) imaging. Vantage system is a MATLAB-friendly programmable platform that can produce co-registered US and PA images; the PA image represents the optical absorption map of the tissue while the US image represents the tissue acoustic impedance map. Here, we describe the subtle details of US/PA imaging system setup including modifications to MATLAB script, sequencing of the US/PA signal generation, details required for efficient use of the hardware of the system and data processing protocols.

### **2.2 Software and hardware setup**

#### **2.2.1 Script analysis**

The following are the details of the MATLAB code for real-time data acquisition, data processing, image reconstruction, and display in order of variable appearance in the script. First, commonly modified parameters can be set. Start and end depth of

imaging can be set for both US and PA with  $P(1).startDepth$  and  $P(1).endDepth$  and  $P(2).startDepth$  and  $P(2).endDepth$ , respectively. In the code,  $na$  sets the number of steered US angles that are transmitted for a single US frame. The default number is 7.  $oneway$  sets whether or not the system runs in simulation mode: 0 for simulation mode is on or 1 for simulation mode is off. Simulation mode ignores hardware and simulates transducer elements and a virtual object to create virtual signals and test if the MATLAB loader program VSX is communicating correctly with *RunAcq*, the simultaneously run C program which communicates with the US hardware. *Flash2Qdelay* is the time between trigger input and start of acquisition in microseconds and must equal the time delay between the flash lamp output and Q-switch output from the laser. We used an oscilloscope to find the exact delay time and set the time value to the *flash2Qdelay* variable. Lastly,  $PA\_PRF$  must be set to the pulse repetition rate of the laser. The next section of the code involves setting up system parameters, such as data buffers, and the transducer array specifications. For Vantage 128 system and a 128-element linear array transducer,  $Resource.Parameters.numTransmit$  and  $Resource.Parameter.numRcvChannels$  are set to 128.  $Trans.name$  is specified as the name of the transducer array that will be operated for the given script. For the two linear array transducer we used (explained later in more details),  $Trans.name$  must be set to either 'L7-4' or 'L22-14v'.  $computeTrans(Trans)$  populates all the attributes of the specified transducer. These attributes include: position of the elements in the probe coordinate system, probe central frequency, element spacing, and other specifications.  $PData$  defines the pixel grid to be manipulated by the image reconstruction software.  $PData(n).PDelta$  defines the spacing between pixels in all dimensions,  $PData(n).Size$

defines rows, columns, and sections of the data, and *PData(n).Origin* defines the x,y,z coordinate of the left corner of the reconstructed image, where  $n$  is 1 for the US image and  $n$  is 2 for the PA image. *RcvBuffer*, *InterBuffer* and *ImageBuffer* are defined to store US and PA data and image reconstructions. Next, the transmit objects (*TW*, *TX*, and *TPC*) are specified. The *TW* structure array is used to define specification of a transmit waveform (type, frequency, duty cycle, duration, and polarity), where *TW(1)* is for US and *TW(2)* is for PA. The *TX* structure array is used to define the specification of the beam characteristics of each transmit action, including which transmitters are active in the aperture (apodization), and the delay time before transmit for each active transmitter. With 7 US transmits, *TX(1:7)* is defined for US transmit events. For PA, only one *TX* struct is needed, so we define *TX(8)* for this event. In *TX(8)*, all transmitters are turned off for the receive-only beamformer. *TPC(1)* for US and *TPC(2)* for PA are defined, where *TPC* (Transmit Power Controller) sets the transmit power level for each specific transmit event. *Receive* objects are defined next and populate all the characteristics of the receive phase of an acquisition event. The Transmit and Receive periods both start at the beginning of acquisition. Next, the *TGC* object defines the time-gain-compensation curve for the receive portion of the acquisition event. To define a *TGC* waveform, the user specifies the *TGC.CntrlPts* array and *TGC.rangeMax*. *TGC.Waveform* is then synthesized and applied to the received data.

The next section describes the reconstruction protocol of the script. The *Recon* structure provides the general attributes of the reconstruction, including the source and destination buffers to use. *Recon.senscutoff* is a value from 0.0 to 1.0 that sets the threshold of sensitivity below which an element is excluded from the reconstruction

summation for a given pixel. We set the cutoff value as 0.975. *Recon.pdatanum(n)* specifies the number of the PData structure that defines the pixel locations of the reconstructed data, where  $n$  is 1 for the US image and  $n$  is 2 for the PA image. *Recon.RcvBufFrame* is an optional attribute that when provided, overrides the frame number specified by the *ReconInfo* structures. Setting *Recon.RcvBufFrame* to -1 allows the last acquisition frame transferred into the *RcvBuffer* to be used in the reconstruction and be displayed for real-time imaging. *Recon.IntbufDest* and *Recon.ImgBufDest* each specify the destination buffer and frame that will receive the reconstructed output. *Recon.RINums* is a row vector that specifies the *ReconInfo* structure indices associated with the most recent reconstruction. For each *Recon*, there is an associated set of *ReconInfo* objects which contain information on how to perform that reconstruction. *Process* objects are used to describe the type of processing to apply to the acquired data. The *Process* object is a structure that specifies a processing task to be executed at a specific point in the event list. After defining the sequence control objects, event objects, and some graphical user interface (GUI) controls, the script is complete for collecting and displaying US and PA data.

### 2.2.2 Transducer setup

The Verasonics software package provides an example PA script named *SetUpL11\_4vFlashAngPA.m*, for the 128-element linear array L11-4v probe. This script is modified to be used with other probes. Two commonly used ultrasound transducers with Vantage system are ATL/Philips L7-4 and Verasonics L22-14v. The specifications of these transducers are listed in Table 1.

**Table 1. Specifications of linear array transducers.** ATL/Philips L7-4, and Verasonics L22-14v.



Model (Unit)	L7-4	L22-14v
Lens Correction	0.8870	0.6804
Central frequency (MHz)	5.2080	15.6250
Bandwidth [Max, Min] (MHz)	[4, 7]	[14, 22]
Number of Elements	128	128
Element Width (mm)	0.2500	0.0800
Spacing (mm)	0.2980	0.1
Max High Voltage (V)	50	30
Focal length (mm)	25	6
Photograph of the device		
(Dimension)	(11cm × 6.0cm × 3.0cm)	(9cm × 3.5cm × 2.5cm)

Table 2 lists the modifications on the original code of the L11-4v needed for the L7-4 and L22-14v. The remainder of the script is compatible as long as the probe is a 128-element linear array.

**Table 2. Modifications to recognize new probes.** Modifications to original L11-4 script provided by Verasonics, for Phillips L7-4, and Verasonics L22-14v probes.

Parameters	Original Script	Modified Script
Imaging Depth	<i>P(1).startDepth = 2;</i> <i>P(1).endDepth = 192;</i> <i>P(2).startDepth = 0;</i> <i>P(2).endDepth = 128;</i>	<i>P(1).startDepth = 0;</i> <i>P(1).endDepth = 192;</i> <i>P(2).startDepth = 0;</i> <i>P(2).endDepth = 192;</i>
Laser Parameters	<i>oneway = 0;</i> <i>flash2Qdelay = 200;</i> <i>PA_PRF = 100;</i>	<i>oneway = 1;</i> <i>flash2Qdelay = 188;</i> <i>PA_PRF = 10;</i>
Active Transducer	<i>Trans.name = 'L11-4';</i> <i>Trans.units = 'mm';</i> <i>Trans = computeTrans(Trans);</i> <i>nElem = Trans.numelements;</i> <i>Trans.maxHighVoltage = 50;</i>	<i>Trans.name = 'L7-4';*</i> <i>Trans.units = 'mm';</i> <i>Trans = computeTrans(Trans);</i> <i>nElem = Trans.numelements;</i> <i>Trans.maxHighVoltage = 50;*</i>

\*Trans.name = 'L22-14v' and Trans.maxHighVoltage = 30 in the case of the L22-14v.

Vantage system supports transducers from different companies. The list of different transducer arrays that can be used with Vantage system is given in Table 3.

**Table 3. Recognizable transducers.** List of immediately recognizable transducers for the Vantage system.

Company	Transducer Model Number	
<b>Philips</b>	L7-4	C8-4V*
	L11-5	C8-5*
	L12-5 38mm	C9-5ICT
	L12-5 50mm	P3-2*
	CL10-5	P4-1
	CL15-7	P4-2
	C4-2	P5-3*
	C5-2	P6-3
	C7-4*	P7-4
<b>Verasonics</b>	L10-4v	L22-14vX
	L11-4v	L22-14vX-LF
	L11-5v	L35-16vX
	L12-3v	L38-22v
	L22-8v	C5-2v
	L22-14v	P4-2v
	L22-14vLF	
<b>GE</b>	GE9LD	GEIC5-9D
	GEC1-6D	GEL3-12D
	GE4CD	GEM5ScD
<b>Siemens</b>	L10-5	
<b>Vernon</b>	4DL7*	

\*These transducers are recognizable by the system, but the system does not have the transducer's attributes which must be manually entered into the computeTrans.m MATLAB file.

If an unrecognized transducer needs to be used, the transducer attributes must be determined independently and input into the computTrans.m script under a new custom transducer case. Key attributes include the central frequency, bandwidth, number of elements, element width, element spacing, element position, and connector pinout arrangement. In addition to unrecognized linear arrays not listed in Table 3, single element-based arrays, ring arrays, or hemispherical arrays can also be connected to the Cannon connector mounted on Vantage system via a custom-made converter.

### 2.2.3 US/PA sequencing

The MATLAB script contains all of the structures for US and PA run-time and is the main source of user control. These structures are communicated to the C-program, runAcq, through activation of the MATLAB loader function VSX. RunAcq then communicates all of the run-time transmit (Tx generation) and receive (Rx generation) structures with the hardware through the hardware abstraction layer (HAL) as the host controller (PC) and Vantage hardware (silver box) are connected through a PCI cable. The hardware also has a built-in A/D conversion and signal conditioning unit. RunAcq, receives the raw data in the RcvBuffer and performs image reconstruction. Once VSX is run, it opens up a GUI including imaging windows of the reconstructed images from RunAcq (US and PA), time gain control, US voltage transmit, and many other processing parameters for real-time user modification to the imaging sequence. These modifications take effect on the hardware between cycles of hand-offs between VSX and RunAcq. Raw data of US and PA are accessible after the completion of the imaging sequence [43]. Vantage system architecture is shown in Figure 2.



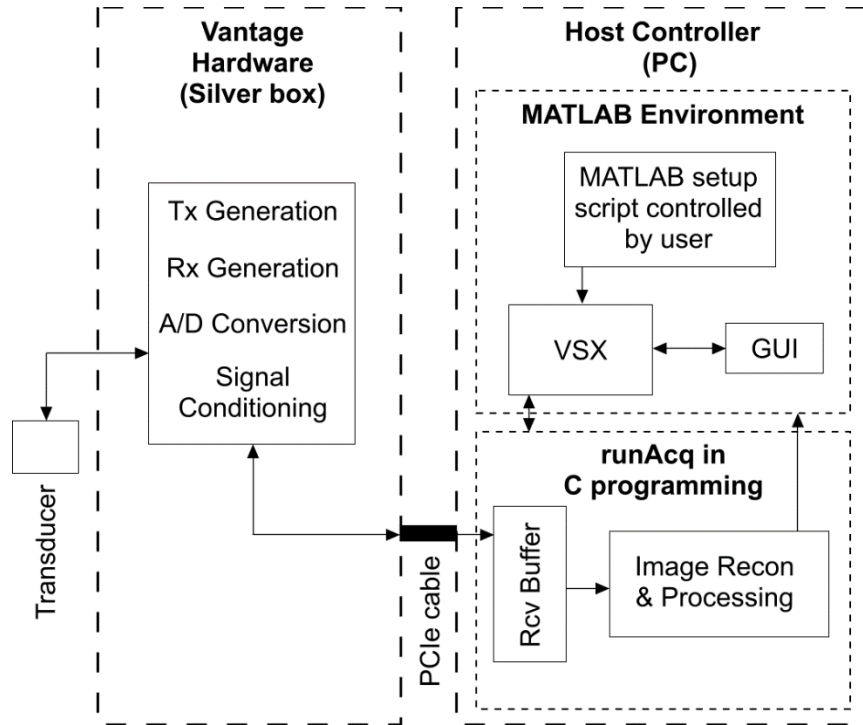


**Figure 2. Simplified system architecture of the Vantage Research System.** TX: transmit, RX: receive, A/D: analog to digital, VSX: Verasonics Script execution, GUI: graphical user interface, Rcv Buffer: receive buffer, CPU: central processing unit.

The timing sequence in US and PA data acquisition, illustrated in Figure 3, is as follows. US acquisition requires a user defined number of steered angles. By default, 7 steered angles are defined for the imaging sequence. Between each set of US acquisitions, the system waits for a trigger input to begin one receive-only PA event. After PA acquisition, US and PA data are transferred to the host controller (indicated as PC in Figure 2). RunAcq then individually performs one US reconstruction on the averaged data of all of the steered angles and one receive-only PA reconstruction. These reconstructed images are then displayed in the MATLAB VSX GUI.

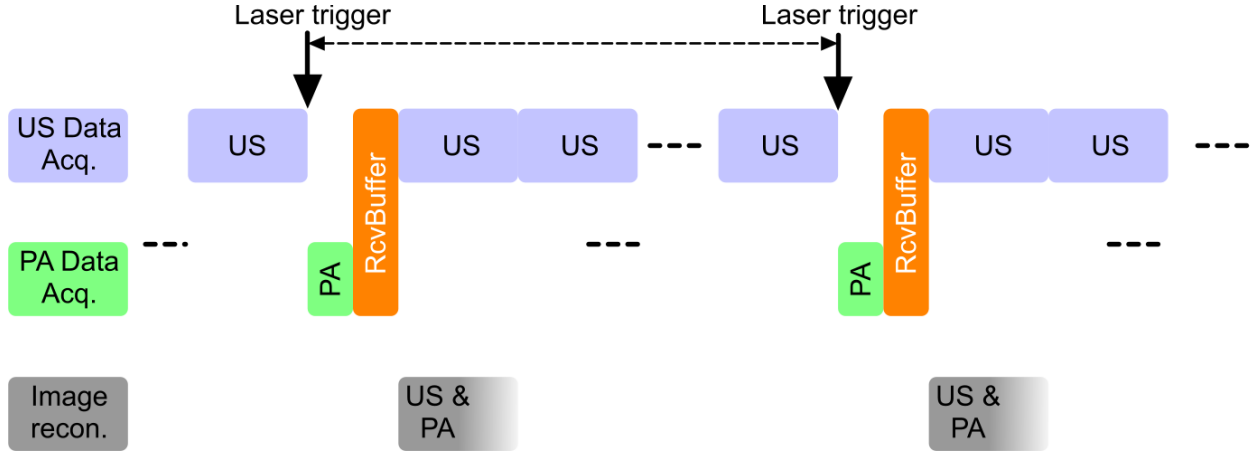


**Figure 3. Timing diagram of US/PA sequencing in Vantage.** US: Ultrasound, PA: Photoacoustic, Recon.: Reconstruction. RcvBuffer is the predefined buffer where the US and PA data is stored, Acq: acquisition.

#### 2.2.4 US/PA experimental setup

To perform an US/PA experiment, an Nd:YAG laser (PhocusMobil, Opotek Inc., CA, USA) with a repetition rate of 10Hz and a pulse width of 8ns was used. The laser uses an optical parametric oscillator (OPO) to tune the wavelength of light between 690-950nm. For light delivery, we used a custom fiber bundle (Newport Corporation, Irvine, CA, USA). For data acquisition, a Verasonics Vantage 128 system was used. The specifications of the vantage system are listed in Table 4.

**Table 4. High frequency Vantage 128 system specifications.** (checked with Verasonics' technical support).

<b>Channels</b>	128 Tx / 128 Rx
<b>Power requirements</b>	100V-240V (50-60 Hz)
<b>Frequency</b>	1 MHz – 50 MHz
<b>Programmable pulser voltage</b>	2 to 190 V p-p
<b>Time delay resolution</b>	4.0 ns
<b>HIFU capability</b>	Yes
<b>A/D resolution</b>	14 bits
<b>Max Sampling rate</b>	62.5MHz
<b>Fastest external trigger</b>	100 KHz
<b>Maximum trigger voltage level</b>	5.5 V
<b>Single transmit event</b>	~ $\mu$ sec
<b>Data pre-amplification</b>	18dB

<b>Second stage Amplification</b>	24 dB
<b>Noise Figure</b>	1.5 to 3.0 dB
<b>Data transfer to host computer</b>	via 8 lanes PCIe 3.0 sustained data transfer rates up to 6.6 GB/s

Vantage system is connected to a host computer using a PCI express cable. A transducer is connected to the 260pin Cannon connector mounted on the Vantage system. On the imaging end, the transducer was placed and held perpendicularly to the sample. To demonstrate the PA signal characteristics in both time and frequency domains, a 2mm diameter carbon lead phantom in water was imaged at 690 nm. The energy after the fiber bundle was measured as  $\sim 15\text{mJ/cm}^2$ . L22-14v transducer array was used in this experiment. The time domain signal obtained from the central transducer (i.e., 64th element), is shown in Figure 4A. In Figure 4B, the single-sided Fast Fourier Transform (FFT) of the time domain signal is shown.

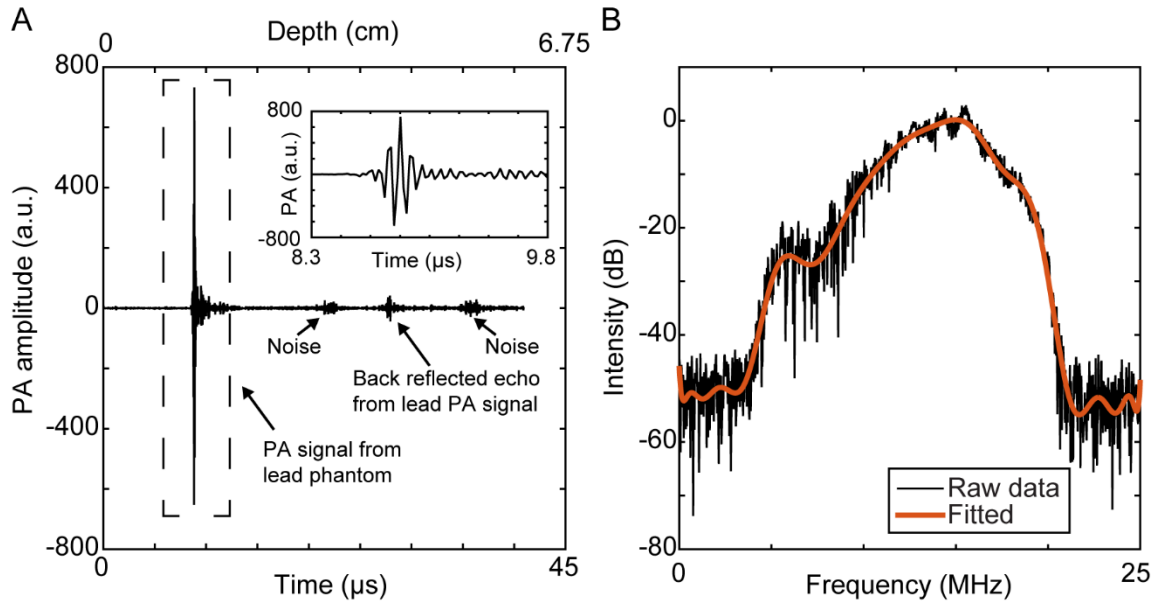


**Figure 4. Example time-domain and frequency domain PA signal.** Photoacoustic signal in (A) time-domain, and (B) frequency-domain, obtained from a 2mm diameter carbon lead phantom, imaged with L22-14v transducer at 690nm illumination wavelength.

## 2.3 Experimental setup considerations

Here, we discuss many experimental setup situations that should be considered prior to any experimentation. Utilizing, the optimal configuration for the following considerations will improve experimental results.

### 2.3.1 Synchronization

Photoacoustic imaging relies on careful timing of data acquisition and laser firing to accurately reconstruct photoacoustic depth information. In Q-switched Nd:YAG lasers, the timing involves triggering of the flash lamps to stimulate the emission medium (Nd:YAG) followed by time for optical buildup and subsequent opening of the Q-switch for release of the laser beam. A straightforward triggering method (see Figure 5A(i)) involves using internal flash lamp and Q-switch triggers built into the laser being used, and using the flash lamp out port to trigger data acquisition on the Vantage trigger in-1 port. Upon receipt of the flash lamp trigger, the Vantage waits for a user-specified delay time equal to the known optical build-up time for the laser and then begins recording approximately when the laser fires. The major drawback to this triggering method is that the optical build-up time for the laser will “jitter” between tens of nanoseconds and will cause the peak PA signal to fluctuate between a few sample numbers. This will cause issues in data averaging between subsequent frames. We have implemented a more optimal triggering method following the method described in [44] (see Figure 5B(i)). In this method the flash lamp and Q-switch of the laser are both externally triggered. Using a function generator (ATF20B, Shenzhen Atten Electronics Co., Ltd., Nanshan, China) a trigger of 10Hz, 5Vpp, 2.5V offset, 50% duty cycle was simultaneously sent to the flash lamp-in of the Nd:YAG laser (PhocusMobil, Opotek,

CA, USA) and the trigger in-1 of the Vantage system. Within the Vantage MATLAB script, the flash2Qdelay parameter is set to the external Q-switch delay time specified by the laser retailer (290  $\mu$ s). This allows the Vantage to then trigger the Q-switch by connecting the Vantage's trigger-out to the Q-switch-in on the laser. We have compared the performance of the two triggering methods by imaging a 2 mm diameter carbon lead, when L7-4 US probe was used and the fiber bundle we described earlier was used for illumination at 690nm. Five sequential photoacoustic frames were recorded and overlaid with both methods (see Figures 5A(ii) and 5B(ii)). The results show a greater “jitter” in the first triggering method compared to nearly no “jitter” in the second method.

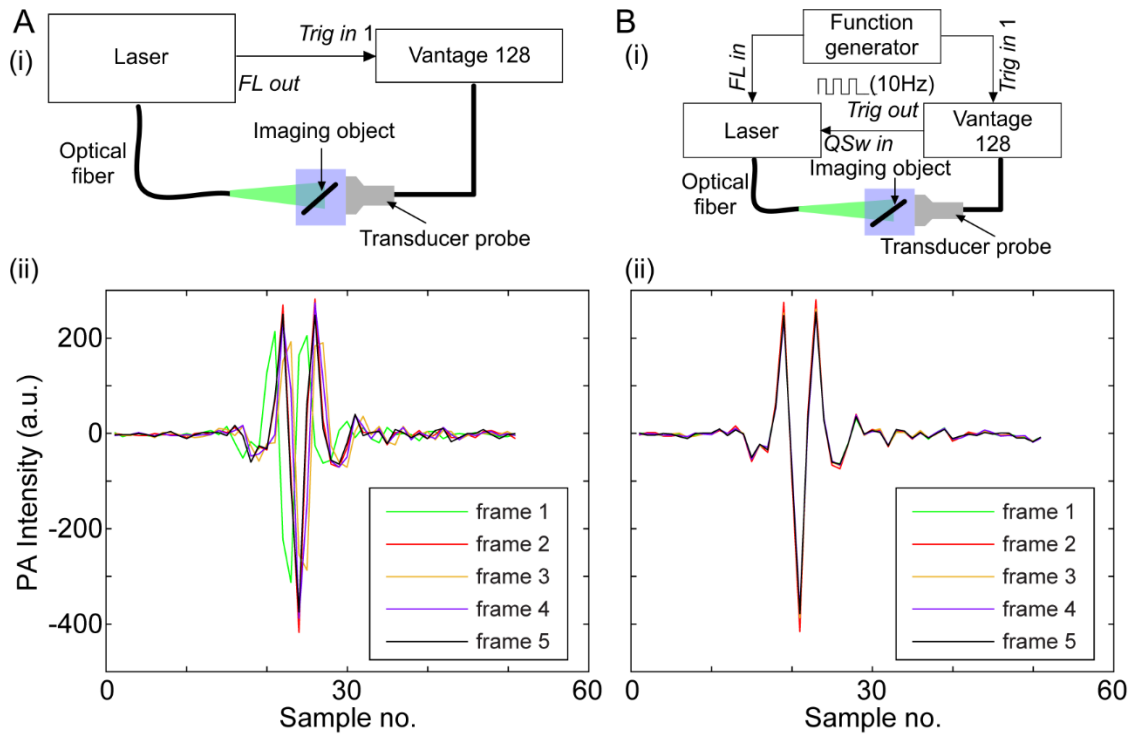


**Figure 5. Photoacoustic signal “jitter” comparison**, between two triggering methods when a 2mm carbon lead was imaged. 64th element signals are plotted. (A) (i) Schematic of straightforward triggering method where laser triggers Vantage system (method 1), (ii) five sequential PA frames showing significant “jitter” between frames, (B) (i) schematic of the function generator driven triggering method where function generator triggers laser flash lamp and Vantage system, which then triggers laser Q-switch (method 2), (ii) five sequential PA frames showing nearly no “jitter” between frames.

### 2.3.2 Frame averaging

Averaging improves the signal-to-noise ratio (SNR) of the PA signal only if the signal components being averaged are correlated and the noise components are not correlated. We imaged a 2mm diameter carbon lead suspended in 100% intralipid at 690nm. 64th element of the L7-4 probe data was averaged using various numbers of stored frames: 1, 10, and 50, and plotted (see Figure 6). As seen, increasing the number of frames, does not linearly increase the SNR of the PA signal, most probably because the correlation between PA signals is reduced as the number of frames increases.

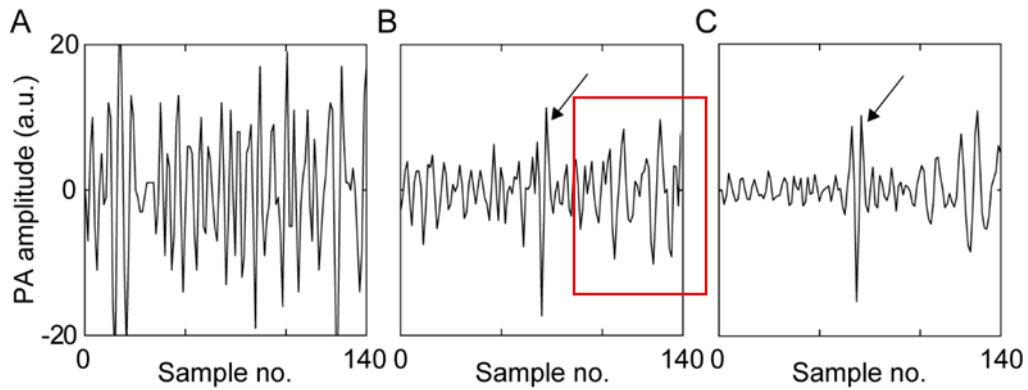


**Figure 6. PA signal SNR improvement with averaging.** 64th element (of L7-4 probe) PA signal obtained from a 2mm carbon lead phantom in 100% concentration of intralipid, when (A) 1, (B) 10, and (C) 50, frames were averaged. Arrow demonstrates location of the PA signal. Red box shows area of reverberation.

### 2.3.3 Illumination angle

Light illumination is the main component in generating photoacoustic signal. The direction of illumination of light can influence the amplitude of signal received by the transducer based on how the light energy is deposited on the object [5]. To investigate this matter, we imaged a 2mm diameter carbon lead in water at 690 nm. We acquired PA data at two illumination angles: 40° and 58°. The angles were measured as the

angle between the transducer and the illumination plane. In these experiments, the transducer plane was held constant while the illumination plane was changed. Figure 7A shows the data collected by the 64th element of the L7-4 probe at an angle of  $40^\circ$ . Figure 7B shows the data collected by the 64th element of the L7-4 probe at an angle of  $58^\circ$ . It can be seen that the shape of the two induced PA signals are consistent while the PA signal amplitude is higher at one angle over another. This demonstrates the importance of optimizing illumination in PA imaging.

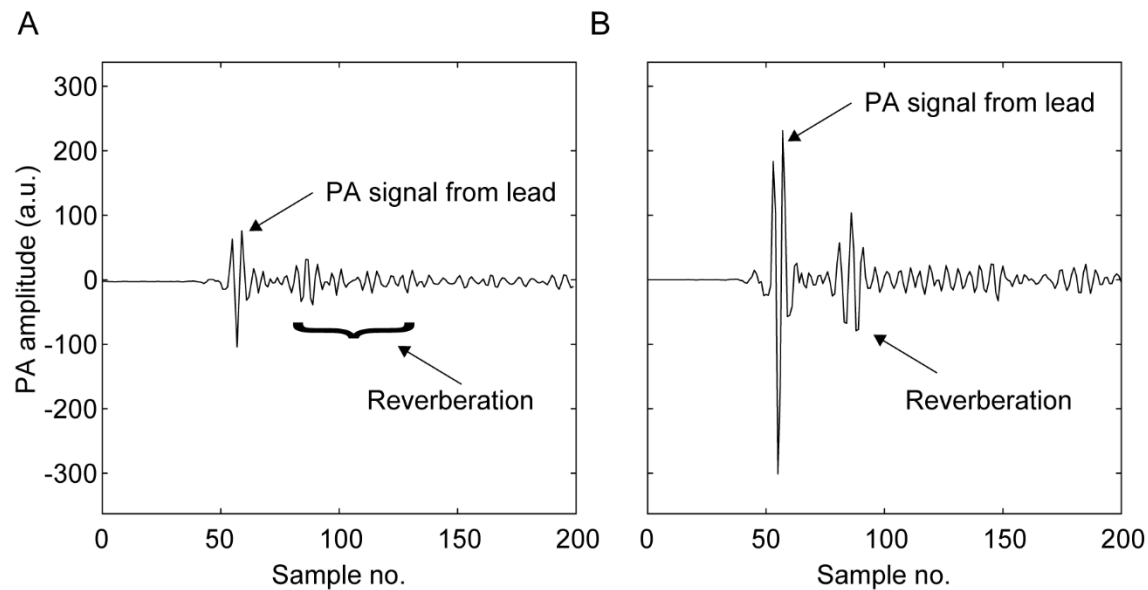


**Figure 7. Importance of illumination angle.** PA signal profile from 64th element of L7-4 probe taken from a 2mm carbon lead phantom with different illumination angles. (A) 40 degrees, (B) 58 degrees.

### 2.3.4 Modifying sampling rate

The Vantage system automatically samples ultrasound signals at a rate that is 4 times the central frequency of the transducer being used. This is sufficient to meet the Nyquist limit, however it may be necessary to analyze PA signals at a higher sampling rate. This requires modifications to the script as well as the use of an in-built filter tool to change the spectrum of the bandpass filter on the receive end of the transducer so that

the system does not mistake the higher sampled signals as high frequency noise. First, the *Resource.RcvBuffer(1).rowsPerFrame* parameter must be multiplied by the factor that the sampling rate will be multiplied. This is to allow the data buffer to hold the increased number of samples. Similarly, the *Receive.decimSampleRate* parameter must be multiplied by the same factor. Finally, the parameter *Receive.inputFilter* must be modified by entering *filterTool* into the MATLAB command line. This brings up a GUI which outputs the *Receive.inputFilter* value based on the user input parameters. Inside the GUI, *sampleMode* should be set to custom with the *decimSampleRate* set to the rate of choice. The bandpass filter central frequency and relative bandwidth should then be set to the standard values of the probe being used. This tool then outputs the appropriate modifications to the *inputFilter* parameter modification seen below. The modifications to the script can be seen in Table 5 for using the L7-4 probe and changing the sampling rate from 20.8MHz to 62.4MHz.

**Table 5. Sampling rate script modifications.** Script modifications to change the sampling rate of L7-4 from 20.8MHz to 62.4 MHz. The modifications are indicated in red.

Change #	Original	After Modification
1	<code>Resource.RcvBuffer(1).rowsPerFrame = 2048*(na + ne);</code>	<code>Resource.RcvBuffer(1).rowsPerFrame = 3*2048*(na + ne);</code>
2	<code>Receive = repmat(struct('Apod', ones(1,Trans.numelements), ... 'startDepth', P(1).startDepth, ... 'endDepth', P(1).startDepth + wl4sPer128*ceil(maxAcqLngth2D/wl4sPer128), ... 'TGC', 1, ... 'bufnum', 1, ... 'framenum', 1, ... 'acqNum', 1, ... 'sampleMode', 'NS200BW', ... 'mode', 0, ... 'callMediaFunc', 0), 1,</code>	<code>Receive = repmat(struct('Apod', ones(1,Trans.numelements), ... 'startDepth', P(1).startDepth, ... 'endDepth', P(1).startDepth + wl4sPer128*ceil(maxAcqLngth2D/wl4sPer128), ... 'TGC', 1, ... 'bufnum', 1, ... 'framenum', 1, ... 'acqNum', 1, ... 'sampleMode', 'NS200BW', ... 'mode', 0, ... 'callMediaFunc', 0,...</code>



	(na+ne)*Resource.RcvBuffer(1).numFrames);	'inputFilter', [+0.00000 +0.00122 +0.00400 +0.00687 +0.00677 +0.00378 +0.00323 ... +0.00931 +0.01569 +0.00861 - 0.01431 -0.03320 -0.02631 -0.00491 ... -0.01303 -0.07413 - 0.14075 -0.12170 +0.02014 +0.20425 +0.28894],... 'decimSampleRate', 20.8333*1), 1, (na+ne)*Resource.RcvBuffer(1).numFrames);
--	---	--

We imaged a black tape phantom of 18mm width at 3 sampling rates, 20.8, 41.6, and 62.4MHz. The tape was imaged in a water bath with the L7-4 probe at the illumination wavelength of 690 nm. The results for these sampling rates are given in Figure 8A, B, and C.

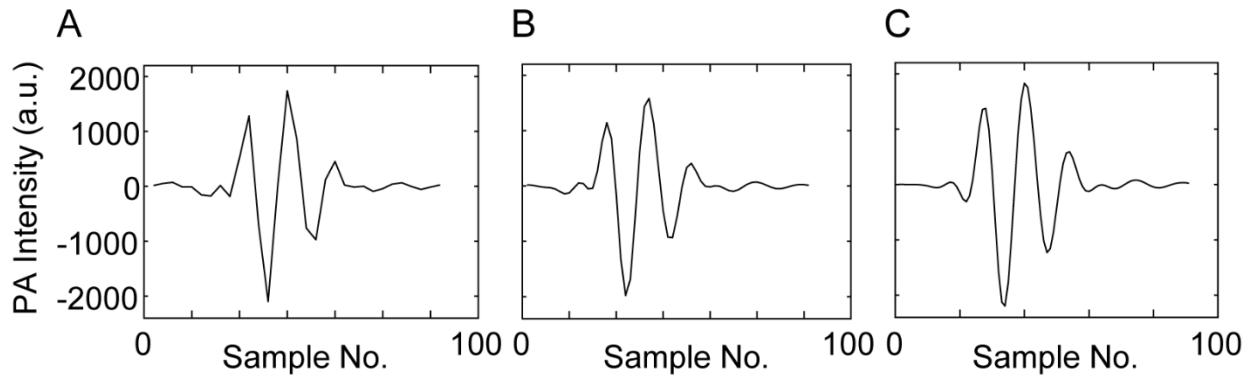


**Figure 8. Signal quality of different sampling rates.** PA signal profile from 64th element of L7-4 probe taken from a black tape phantom of 18mm width with varying sampling rates: (A) 20.8MHz, (B) 41.6MHz, (C) 62.4MHz.

### 2.3.5 US/PA simultaneous display

The default MATLAB script utilizes a single imaging window for both US and PA image display, with the user being able to modify parameters to view one or the other. With real-time imaging, it is more important to simultaneously view US and PA images side by side. The following describes how to modify the original example script to simultaneously display US and PA images in real-time. With a single imaging window,

all parameters for the Resource struct have arguments of 1. Adding a second window requires duplication of all of the Resource parameters, but with an argument of 2. Specifically, the variables *Title*, *pdelta*, *Position*, *ReferencePt*, *numFrames*, *AxesUnits*, *Colormap*, and *splitPalette* are copied from the already existing *Resource.DisplayWindow(1)* struct, but with the argument changed to 2. To differentiate between US in window 1 and PA in window 2, we set *Resource.DisplayWindow(1).Colormap* to *gray(256)* and *Resource.DisplayWindow(2).Colormap* to *hot*. The other change necessary to keep both windows real-time is modification of the *Process(n).Parameters* struct where *n* is 1 for US and 2 for PA. In the original struct, *mappingMethod* is set to *lowerHalf* for US and *upperHalf* for PA, but both should now be set to *full*. Also, *displayWindow* was originally set to 1 in both processes, but now it should be 1 for US and 2 for PA. The modifications to the original script can be seen in Table 6.

**Table 6. 2 window display script modifications.** Modifications to the original script to simultaneously display US and PA images, in real-time. The modifications are indicated in red.

Change #	Original script	After Modification
1	Resource.DisplayWindow(1).Title = mfilename; Resource.DisplayWindow(1).pdelta = 0.4; ScrnSize = get(0,'ScreenSize'); DwWidth = ceil(PData(1).Size(2)*PData(1).PD elta(1)/Resource.DisplayWindow(1 ).pdelta); DwHeight = ceil(PData(1).Size(1)*PData(1).PD elta(3)/Resource.DisplayWindow(1 ).pdelta); Resource.DisplayWindow(1).Positi on = [250,(ScrnSize(4)-	Resource.DisplayWindow(1).Title = mfilename; Resource.DisplayWindow(1).pdelta = 0.4; ScrnSize = get(0,'ScreenSize'); DwWidth = ceil(PData(1).Size(2)*PData(1).PDelta(1 )/Resource.DisplayWindow(1).pdelta); DwHeight = ceil(PData(1).Size(1)*PData(1).PDelta(3 )/Resource.DisplayWindow(1).pdelta); Resource.DisplayWindow(1).Position = [250,(ScrnSize(4)-(DwHeight+150))/2, ... DwWidth, DwHeight]; Resource.DisplayWindow(1).Reference

	<pre> (DwHeight+150))/2, ... DwWidth, DwHeight]; Resource.DisplayWindow(1).ReferencePt = [PData(1).Origin(1),0,PData(1).Origin(3)]; Resource.DisplayWindow(1).numFrames = 2; Resource.DisplayWindow(1).AxesUnits = 'mm'; Resource.DisplayWindow(1).Colormap = gray(256); Resource.DisplayWindow(1).splitPalette = 1; </pre>	<pre> Pt = [PData(1).Origin(1),0,PData(1).Origin(3)]; Resource.DisplayWindow(1).numFrames = 2; Resource.DisplayWindow(1).AxesUnits = 'mm'; Resource.DisplayWindow(1).Colormap = gray(256); Resource.DisplayWindow(1).splitPalette = 1;  Resource.DisplayWindow(2).Title = mfilename; Resource.DisplayWindow(2).pdelta = 0.4; Resource.DisplayWindow(2).Position = [250,(ScrnSize(4)-(DwHeight+150))/2, ... DwWidth, DwHeight]; Resource.DisplayWindow(2).ReferencePt = [PData(1).Origin(1),0,PData(1).Origin(3)]; Resource.DisplayWindow(2).numFrames = 2; Resource.DisplayWindow(2).AxesUnits = 'mm'; Resource.DisplayWindow(2).Colormap = hot; Resource.DisplayWindow(2).splitPalette = 1; </pre>
2	<pre> Process(1).classname = 'Image'; Process(1).method = 'imageDisplay'; Process(1).Parameters = {'imgbufnum',1,... 'framenum',-1,... 'pdatanum',1,... 'pgain',1.0,... 'reject',10,... 'persistMethod','simple',... 'persistLevel',50,... 'interpMethod','4pt',... 'grainRemoval','none',... </pre>	<pre> Process(1).classname = 'Image'; Process(1).method = 'imageDisplay'; Process(1).Parameters = {'imgbufnum',1,... 'framenum',-1,... 'pdatanum',1,... 'pgain',1.0,... 'reject',10,... 'persistMethod','simple',... 'persistLevel',50,... 'interpMethod','4pt',... 'grainRemoval','none',... 'processMethod','none',... 'averageMethod','none',... </pre>

<pre> 'processMethod','none',... 'averageMethod','none',... 'compressMethod','power',... 'compressFactor',40,... 'mappingMethod','lowerHalf',... 'display',1,... 'displayWindow',1};  Process(2).classname = 'Image'; Process(2).method = 'imageDisplay'; Process(2).Parameters = {'imgbufnum',2,... 'framenum',-1,... 'pdatanum',2,... 'pgain',1.0,... 'reject',10,... 'persistMethod','dynamic',... 'persistLevel',cpers,... 'interpMethod','4pt',... 'grainRemoval','none',... 'processMethod','none',... 'averageMethod','none',... 'compressMethod','power',... 'compressFactor',40,... 'mappingMethod','upperHalf',... 'threshold',cpt,... 'display',1,... 'displayWindow',1}; </pre>	<pre> 'compressMethod','power',... 'compressFactor',40,... 'mappingMethod','full',... 'display',1,... 'displayWindow',1};  Process(2).classname = 'Image'; Process(2).method = 'imageDisplay'; Process(2).Parameters = {'imgbufnum',2,... 'framenum',-1,... 'pdatanum',2,... 'pgain',1.0,... 'reject',10,... 'persistMethod','dynamic',... 'persistLevel',cpers,... 'interpMethod','4pt',... 'grainRemoval','none',... 'processMethod','none',... 'averageMethod','none',... 'compressMethod','power',... 'compressFactor',40,... 'mappingMethod','full',... 'threshold',cpt,... 'display',1,... 'displayWindow',2}; </pre>
---	---

### 2.3.6 Comparing US and PA signals received by the transducer

In US imaging, the acoustic pressure wave is generated by applying a pulsed electrical signal across piezoelectric elements at a specific frequency. This pressure (acoustic) wave propagates through the medium and is reflected back from the acoustic boundary of the object due to the impedance mismatch between the propagating medium and object interface [45]. In contrast, in PA imaging, the acoustic pressure wave is induced from the absorption of the pulsed laser. Due to an incident pulsed laser, dielectric properties of the biological tissue will take a finite amount of time to

polarize [46] and the time-varying nature of the field will cause the polarization of the dielectric to be out of phase with the field. Immediately after the absorption, the dissipative energy is converted into heat in an adiabatic condition and causes the temperature to rise. The heating process is governed by the heat diffusion and consequent temperature rise followed by thermoelastic expansion which then induce the pressure wave (ultrasound) [47]. To compare the US echo and PA signals, a 2mm diameter carbon lead phantom was imaged in water at 690nm. Laser energy was maintained to about  $15\text{mJ}/\text{cm}^2$  at the sample. The PA signal amplitude was then compared to US signal amplitude when the transmit voltage for US imaging was set to 2.5V; we kept all other gains constant. The results are shown in Figure 9.

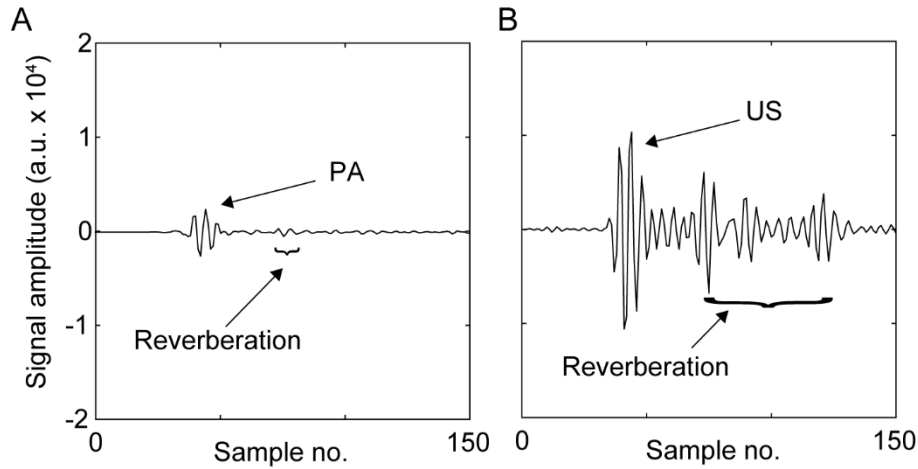


**Figure 9. Comparing absolute magnitude of PA and US signal.** US and PA signal profiles from 64th element of L7-4 probe when a 2mm diameter carbon lead phantom was imaged. The transmit voltage in US imaging was set to 2.5 V. The laser energy at the sample in PA imaging was  $15\text{mJ}/\text{cm}^2$ . (A) Photoacoustic signal, (B) ultrasound signal.

### 2.3.7 US/PA image resolution analysis

L7-4 and L22-14v, are two commonly used US transducers with the Vantage system for US/PA imaging. We created a resolution phantom of hair of diameter  $54\mu\text{m}$  in an open top plastic cubic box filled with deionized water (see Figure 10A). The lateral

and axial resolutions were measured by measuring the full width half maximum (FWHM) of the normalized 1D intensity profile along x and y axes of a hair image, respectively [48]. The axial and lateral resolutions of the L7-4 were measured at depths 0.5, 1.0, 1.5, 2.0, 2.5, 3.0, 3.5, 4.0, 4.5, and 5.0 cm (see Figure 10B). The axial and lateral resolutions of the L22-14v were measured at depths 0.2, 0.4, 0.6, 0.8, 1.0, 1.2, 1.4, 1.6, 1.8, 2.0 cm (see Figure 10C). L7-4 axial resolution remained constant in both US and PA imaging while the lateral resolution worsened with depth, which may be attributed to the focal depth specified by the Vantage system. The L22-14v axial and lateral resolutions stayed almost constant in both US and PA images, potentially due to the focal depth specified by the Vantage system. Further, high frequency transducers have less beam divergence than low frequency which is contributing to the worsening lateral resolution of the L7-4 and constant lateral resolution of the L22-14v [49].

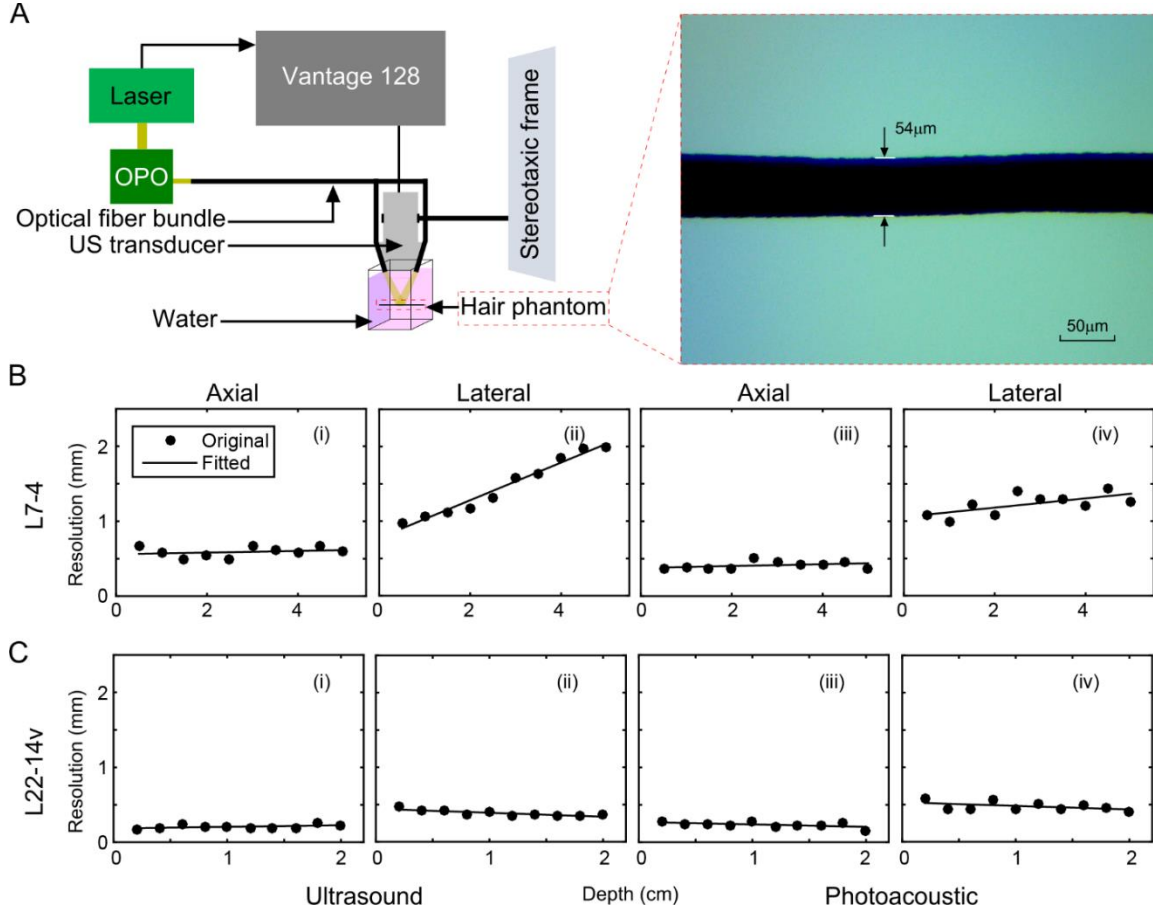


**Figure 10. US/PA resolution study.** (A) Schematic of the experimental setup, including a hair phantom photograph captured by a 4 $\times$  objective on a light microscope (SME-F8BH, Amscope, CA, USA). resolution study when (B) L7-4 was used, (C) L22-14v was used. (i) US axial resolution versus depth, (ii) US lateral resolution versus depth, (iii) PA axial resolution versus depth, (iv) PA lateral resolution versus depth.

### 2.3.8 US image quality improvement through beam steering

The Vantage example script offers beam steering as a method of improving US image quality. This technique modifies transmit delay times in the beam apodization to steer the beam at different directions into the imaging field. This provides received echoes from different angles of reflection off the imaging targets. The received echoes from multiple steered angles are then averaged to form an improved image. The variable  $na$  can be set to any positive integer to determine the number of steered

angles. The transmit waveforms will be emitted at angles of  $\frac{n\pi}{N+1}$ , where N is equal to the variable  $na$ , and n iterates with each transmit angle from 1 to N, where  $\frac{\pi}{2}$  is normal to the transducer elements. Upon definition of  $na$  the example script calculates these angles and corresponding time delays in the apodization for each element. The script specifies how much time occurs between each US steered angle. Taking this time into account with the pulse repetition rate of the laser, the user must determine how many angles can occur between each laser pulse. Further, increasing the number of steered angles and number of stored frames in each buffer must be balanced to avoid slowdown of the system due to memory build up, which can potentially freeze MATLAB if the system RAM is overflowed.

To investigate the effect of the number of steered US transmit angles on the image quality, we imaged a phantom, with 2 mm, 0.9 mm, and 0.2 mm diameter carbon leads, in water with varying numbers of steered angles (i.e., 8, 16, 32, 64, 128), and quantified the contrast to noise ratio (CNR) of resultant images [5]. Figure 11A demonstrates the experimental setup. Figure 11(B-F) show the US image for 8, 16, 32, 64, and 128 steered angles, respectively. Figure 11G shows the improvement of CNR with greater number of steered angles.



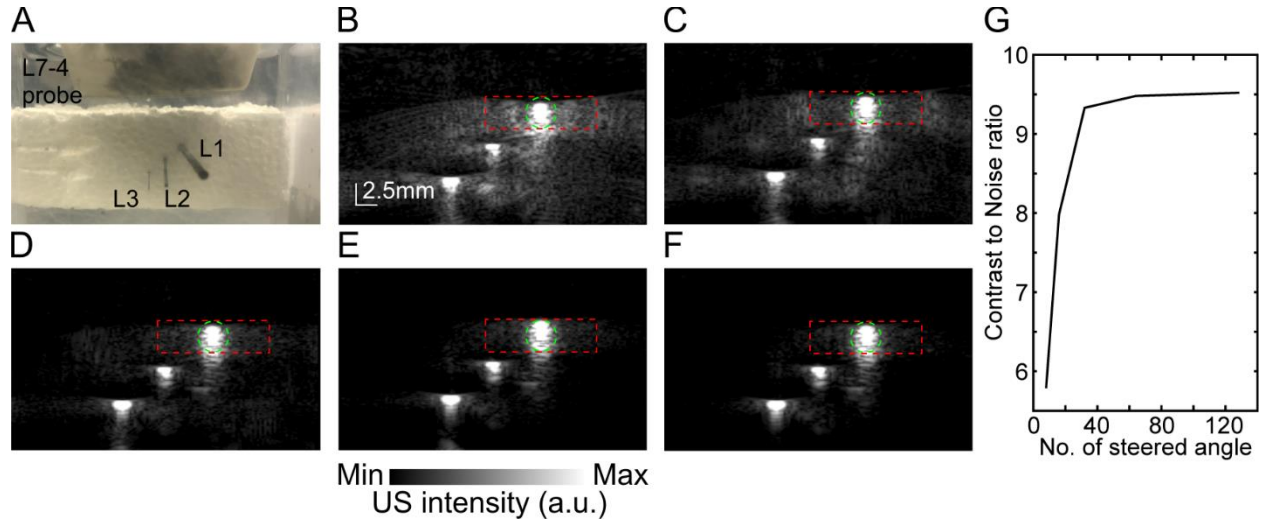


**Figure 11. US image quality with increasing number of steered angles.** US image quality improvement with a greater number of ultrasound steered angles. (A) Experimental setup showing ultrasound probe and a 3-carbon lead phantom. (L1) 2 mm diameter carbon lead, (L2) 0.9 mm diameter carbon lead, (L3) 0.2 mm diameter carbon lead, (B-F) US images of the 3 carbon lead phantom for 8, 16, 32, 64, and 128 steered angles, respectively. Green dashed circle encloses object pixels and red dashed box encloses background pixels, (G) US image CNR versus number of steered angles.

### 2.3.9 Photoacoustic signal amplification

The PA pressure waves received by the linear array transducer are too weak compared to the regular echo signal in US imaging (see the results in Figure 9). Such low voltage signals cannot accurately be digitized using Vantage data acquisition (DAQ) system. To increase the amplitude of the received signal, we have used a 128-channel amplifier (AMP128-18, Photosound, Houston, TX, USA). The amplifier has 40dB gain with -6dB cut off frequencies of 25kHz and 35MHz. The amplifier is attached to the 260pin Cannon connector on Vantage system (see Figure 12). The US probe is then plugged into the front end of the amplifier. In the MATLAB script *computeTrans.m*, a custom transducer ID is added. Details of the ultrasound transducer being amplified must be copied to the custom ID so that the amplifier can be recognized. This is similar to the addition of any unrecognized transducer to the system, only the transducer

attributes must be determined independently and input into the *computTrans.m* script under a new custom transducer case. Key attributes include the central frequency, bandwidth, number of elements, element width, element spacing, and element position. To allow for identical wiring path lengths through the amplifier from the transducer end to Vantage system end, the pins are not connected one to one and their organization must be corrected in the MATLAB script in the *Trans.Connector* variable. Since the amplifier is programmed to multiply any signal going in or out, to avoid causing damage to the transducer elements during US transmit, the transmit beam is disabled by setting *TX.Apodization* to zeros. This allows the Vantage system to only work in receiving mode with amplification.

To demonstrate the utility of the amplifier, a two-wire phantom (each with 600 $\mu$ m diameter) was imaged with and without the amplifier at varying concentrations of intralipid (0%, 25%, 50%), made by mixing a whole milk (Kroger, Waterford, MI) with distilled water. The experimental setup is shown in Figure 12A. It consists of a 50Hz, 532nm Nd:YAG laser (NL231-50-SH, EKSPLA, Vilnius, Lithuania) with 7ns pulses, and an L7-4 US transducer. The laser illuminated the 2-wire phantom through a large fiber optic bundle (1cm diameter, FO Lightguide, Edmund Optics, NJ, USA). We observed an SNR improvement in addition to the signal peak increase in all concentrations of intralipid (see Figure 12B, C, and D). SNR improvement was due to the high pre-amplifier input impedance which shifted the transducer noise spectrum to low frequencies, which is then filtered out using a high-pass filter [50].

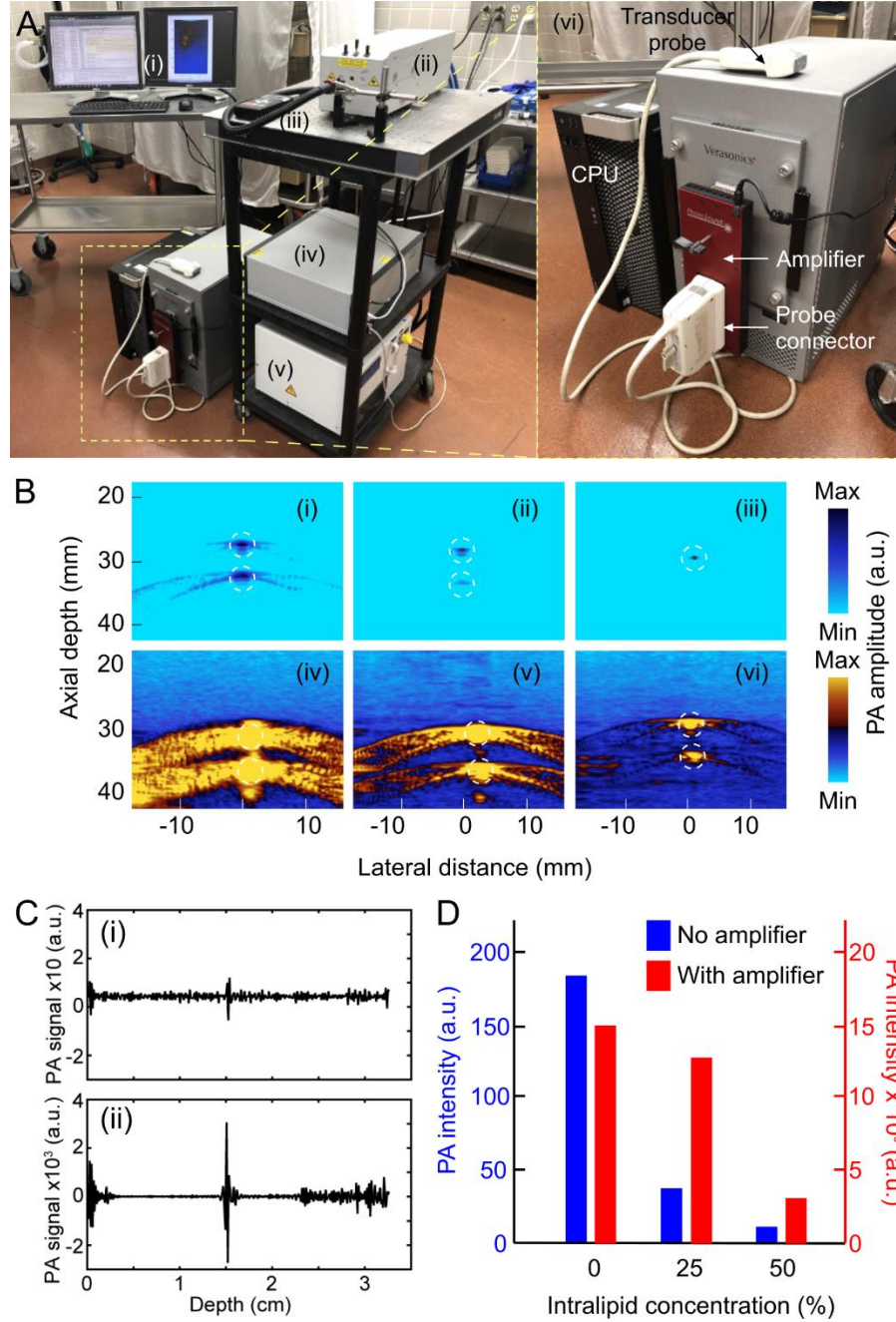


**Figure 12. PA signal amplification.** (A) System setup to test the Photosound AMP128-18 amplifier: (i) display monitor, (ii) Nd:YAG laser head, (iii) fiber optic bundle, (iv) laser power supply, (v) laser chiller. (B) Wire imaging results: wire phantom suspended in 0% intralipid imaged (i) without and (iv) with amplifier, wire phantom suspended in 25% intralipid imaged (ii) without and (v) with amplifier, and wire phantom suspended in 50% intralipid image (iii) without and (vi) with amplifier. (C) Raw data from the 64th channel of the linear array when imaging a single wire in 50% intralipid concentration demonstrating improvement in SNR between (i) without amplifier and (ii) with amplifier.

(D) Bar chart demonstrating signal amplitude increase corresponding to phantom imaging in B with and without amplifier.

### 2.3.10 Fluence compensation

The initial PA pressure is proportional to the product of local optical absorption coefficient and the optical fluence deposited at the same location. However, the optical fluence could vary significantly in living tissue which necessitates the use of optical fluence compensation for quantitative PA imaging [51]. If the optical parameters of the tissue, e.g., absorption coefficient, scattering coefficient, and anisotropy factor, are known, the optical fluence can be calculated by solving the photon diffusion equation using Monte Carlo (MC) or finite element method [52, 53]. With the known optical fluence distribution, a fluence-compensated absorption map can be calculated via dividing the PA reconstructed image by its corresponding fluence map.

We evaluated the fluence compensation algorithm on a phantom made of a gelatin, intralipid, and ink mixture (see Figure 13A and B). We used 0.5 mm diameter carbon lead in three layers of gelatin phantom with thicknesses of 5, 8, and 7mm, respectively. We added intralipid (Sigma Aldrich, USA) as scatterers and used ink to represent absorption. The concentration of the intralipids were 4%, 1%, and 6%, and those of ink were 0.1%, 0.4%, and 0.2%, respectively. These values were chosen to represent various biological tissues. Using Mie calculator [54], the scattering coefficient, absorption coefficient, and anisotropy factor of the layers were calculated at 532nm. The scattering coefficients were  $15.4\text{cm}^{-1}$ ,  $3.1\text{cm}^{-1}$  and  $22.3\text{cm}^{-1}$ , respectively. The absorption coefficients were  $0.3\text{cm}^{-1}$ ,  $0.9\text{cm}^{-1}$ , and  $0.4\text{cm}^{-1}$ , respectively. The absorption coefficient of water, i.e.,  $0.11\text{cm}^{-1}$ , was added to these numbers. We used another layer of pure gelatin with the thickness of 5mm. The scattering coefficient of both pure gelatin

and US gel was considered  $0.05\text{cm}^{-1}$ . The absorption coefficient of US gel (3mm layer) was considered  $0.11\text{cm}^{-1}$ . The experimental protocol was as follows: (1) we imaged the phantom using the L7-4 probe and generated an US image (see Figure 13C) and a PA image (see Figure 13D); (2) we then segmented the US image using the segmentation method given in [55]; (3) optical properties were assigned to each segment (that we designed the phantoms with), creating the phantom optical model; (4) fluence map (see Figure 13E) of the phantom optical model was generated by an MC simulation (using MCX software [56]); (5) finally, the PA image was divided by the MC simulated image. The resultant image was a fluence-compensated PA image (see Figure 13F). The PA intensity variation between the peaks (at the location of imaging targets) in the fluence-compensated PA image was less than 5%.

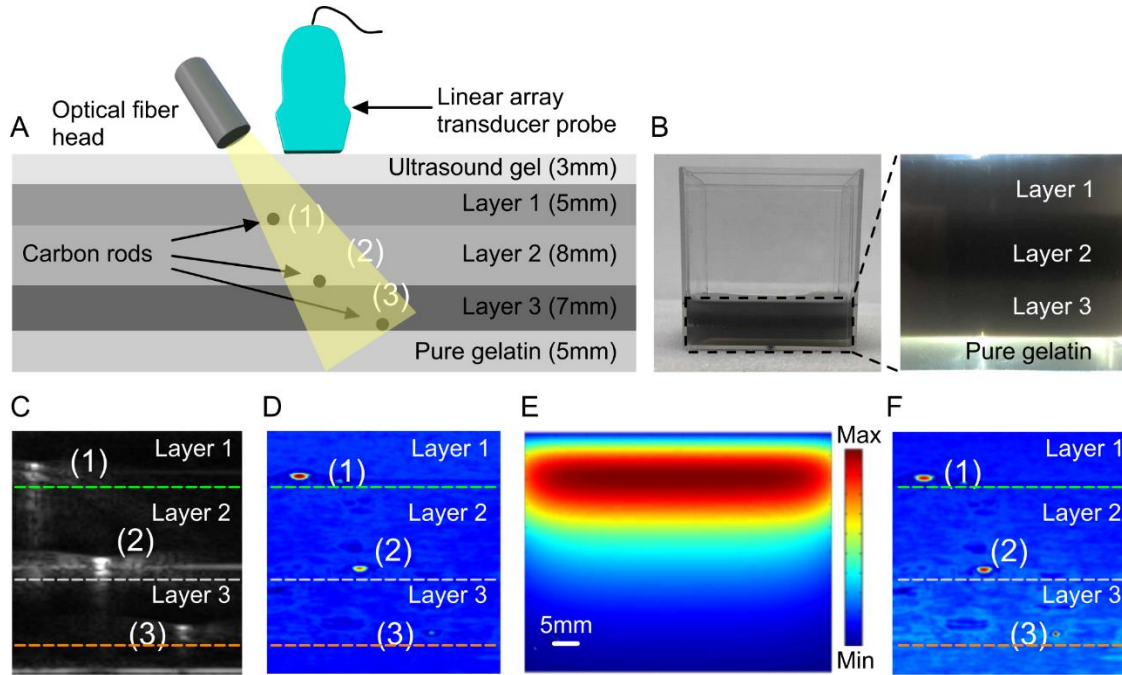


**Figure 13. Fluence Compensation algorithm validation.** (A) Schematic of a phantom with 3 layers of gelatin phantom mixed with intralipid/ink solution and 3 carbon lead imaging targets, (B) photograph of the phantom made in a cube box and magnified to show the layers, (C) US image of the phantom, (D) PA image before fluence

compensation, (E) Monte Carlo simulation of light propagation in the phantom, (F) PA image after fluence compensation.

### **2.3.11 Water as photoacoustic imaging couplant**

The PA imaging methodology contains ultrasonic transducers and an acoustic coupling layer between the imaging target and transducers. Propagation of generated ultrasound from the imaging target is least attenuated when received by the ultrasound sensor through a coupling agent that exhibits minimal acoustic impedance mismatch with the imaging target. Hence, it helps minimizing the degradation and signal loss [57]. Acoustic couplants can be characterized in the following groups: liquids, gels, and dry. Water has a low acoustic attenuation and impedance (1.5MPa.s/m) which makes it suitable as a PA coupling material, and is widely used for PA applications. In terms of water optical properties, it absorbs over a wide range of electromagnetic radiation with rotational transitions and intermolecular vibrations responsible for absorption in the microwave ( $\approx 1\text{mm} - 10\text{cm}$  wavelength) and far-infrared ( $\approx 10\mu\text{m} - 1\text{mm}$ ), intramolecular vibrational transitions responsible for absorption in the infrared ( $\approx 1\mu\text{m} - 10\mu\text{m}$ ), and electronic transitions responsible for absorption in the ultraviolet region ( $< 200\text{nm}$ ) [58-60]. In regular water ( $\text{H}_2\text{O}$ ), a first large absorption band occurs at a wavelength of 980nm [58, 61, 62] followed by another band at  $\sim 1450\text{nm}$ . The absorption spectrum of heavy water ( $\text{D}_2\text{O}$ ) is different from that of  $\text{H}_2\text{O}$ , mainly due to the heavier deuterium nucleus. Resonance positions occur at a wavelength of around 1000nm, 1330nm, and 1600nm [63, 64]. The spectral features of water absorption also depend upon the temperature [58, 63]. As temperature decreases, the fraction of hydrogen-bound water molecules is increased, causing the absorption peak to reduce in intensity, broaden in

bandwidth, and shift to lower energy. Data for Figure 14 has been extracted from [58, 63] and reproduced.

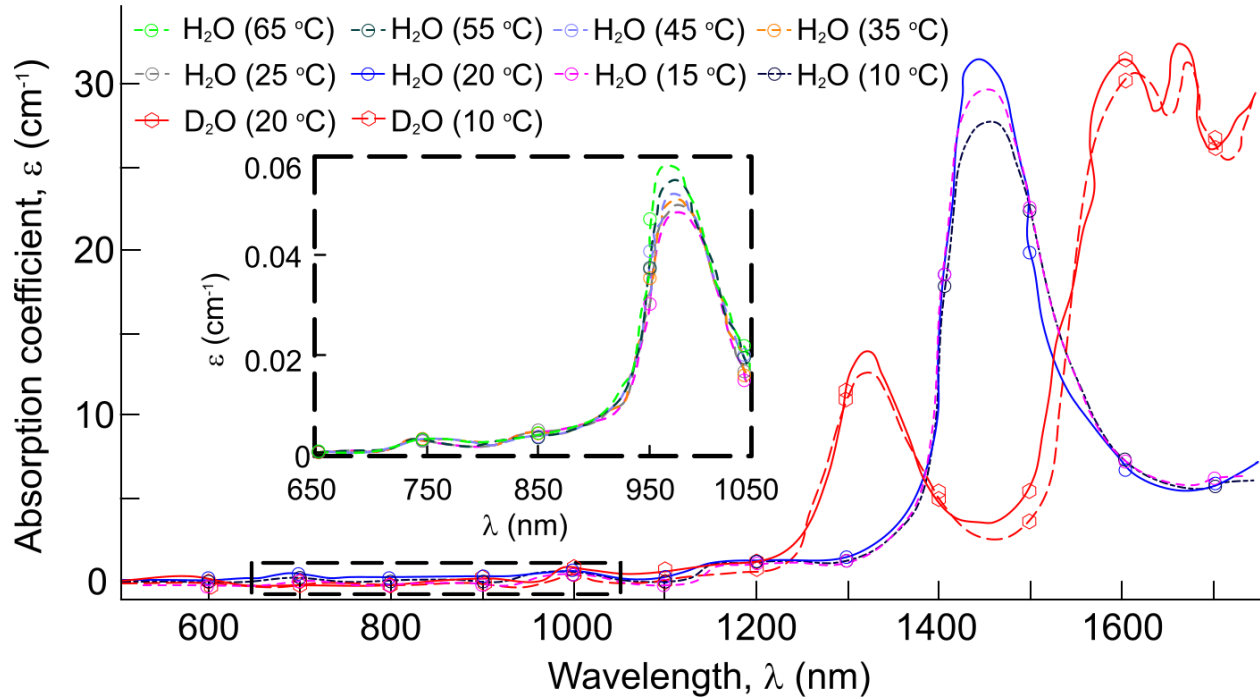


**Figure 14. Analysis of water optical absorption spectrum.** Optical absorption spectrum of regular water (H<sub>2</sub>O) and heavy water (D<sub>2</sub>O) at various temperature in NIR region.

## 2.4 PA Image reconstruction

### 2.4.1 Evolution of PA image reconstruction algorithms

After detecting PA signals by the linear array, the channel data are given to an image reconstruction algorithm and an optical absorption distribution map is reconstructed. Several different image reconstruction algorithms have been studied for linear-array PA imaging [65-72]. The most basic algorithm is delay-and-sum (DAS) [73]. DAS follows the dynamic focusing protocol, in which the focus is adjusted for each pixel of the imaging target; the detected signals are delayed proportional to the distance between the focused point and the position of the element in the imaging array). Finally, the delayed signals are summed up, and an image is formed. As a result of this

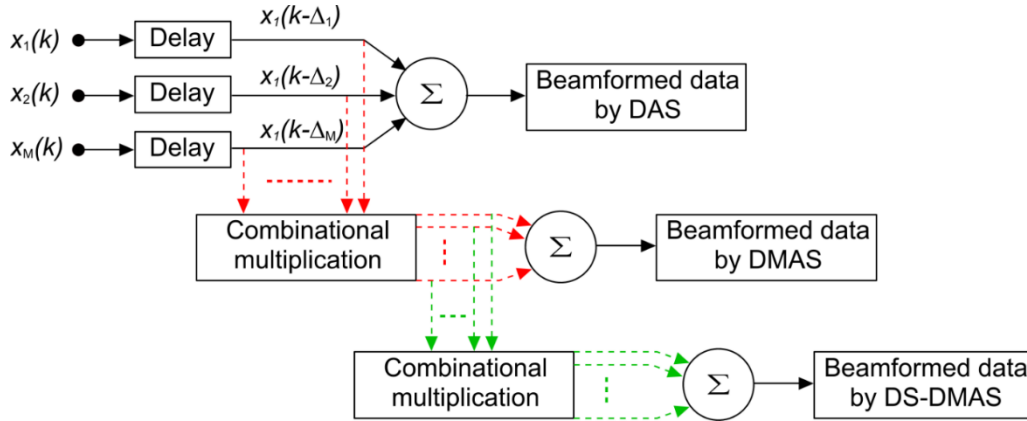
summation, the on-axis signals will overlap on each other while off-axis signals will be suppressed.

In this section, we used two signal quality metrics to compare the performance of different image reconstruction algorithms: (i) resolution, which is defined as the full width half maximum (FWHM) of the lateral profile of the image of a point source, and (ii) sidelobe, defined as the power of the first lobe next to the main lobe. Although DAS algorithm is simple to implement and fast, it treats all the detected signals the same way which results in low resolution images with high sidelobes; this is mainly due to the constructive overlap of the off-axis signals [74-78]. Delay-Multiply-and-Sum (DMAS) can generate images with a finer resolution and lower sidelobes compared to DAS [79]. Double Stage DMAS (DS-DMAS) algorithm offers finer resolution, and lower sidelobes [80] than DMAS; DS-DMAS uses two stages of correlation process to suppress off-axis signals. Minimum variance (MV) significantly improves the image resolution compared to DAS, DMAS and DS-DMAS, however the produced images have high sidelobes; this problem has been addressed in MV-DMAS [77, 81-88]. The eigen-space version of MV-DMAS, i.e., EIMV-DMAS, evaluated in [89], provides similar resolution to MV-DMAS with lower sidelobes. Methods that use minimum variance algorithm, are sensitive to the quality of the received data. This issue limits the application of these methods for PA image reconstruction that uses weak PA signals. Among the image reconstruction algorithms described above (see Table 7), DS-DMAS is the most suitable one for linear-array based PA image reconstruction, because it reconstructs images with fine resolution and low sidelobes, and has a low computational complexity. A block diagram of DS-DMAS algorithm is shown in Figure 15.



**Table 7. Reconstruction algorithm performance comparison.**

Algorithm	Resolution	Sidelobes	Complexity	Reference
<b>DAS</b>	Low	High	$O(M)$	[90, 91]
<b>MV</b>	High	High	$O(M^3)$	[76, 84]
<b>DMAS</b>	Low	Medium	$O(M^2)$	[79, 92]
<b>DS-DMAS</b>	Medium	Low	$O(M^2)$	[69, 85]
<b>MV-DMAS</b>	High	High	$O(M^3)$	[84, 86]
<b>EIMV-DMAS</b>	High	Low	$O(M^3)$	[89]

**Figure 15. Block diagram of DS-DMAS algorithm.**

#### 2.4.2 Evaluation of performance of DS-DMAS algorithm

Four wire phantoms were prepared for this study (Figure 16A). Transducers were securely held by a clamp which was attached to an x-y translation stage. The phantom container was fixed to the optical table and filled with distilled water. Each phantom was imaged 50 times. Figure 16(B-E) demonstrate images of the four wire phantoms taken with the L7-4 probe where (i) is US, (ii) is PA reconstructed in the Vantage system, and (iii) is PA reconstructed with DS-DMAS. Figure 16(F-I) demonstrate images of the four wire phantoms taken with the L22-14v probe where (i) is US, (ii) is PA reconstructed in the Vantage system, and (iii) is PA reconstructed with DS-DMAS.

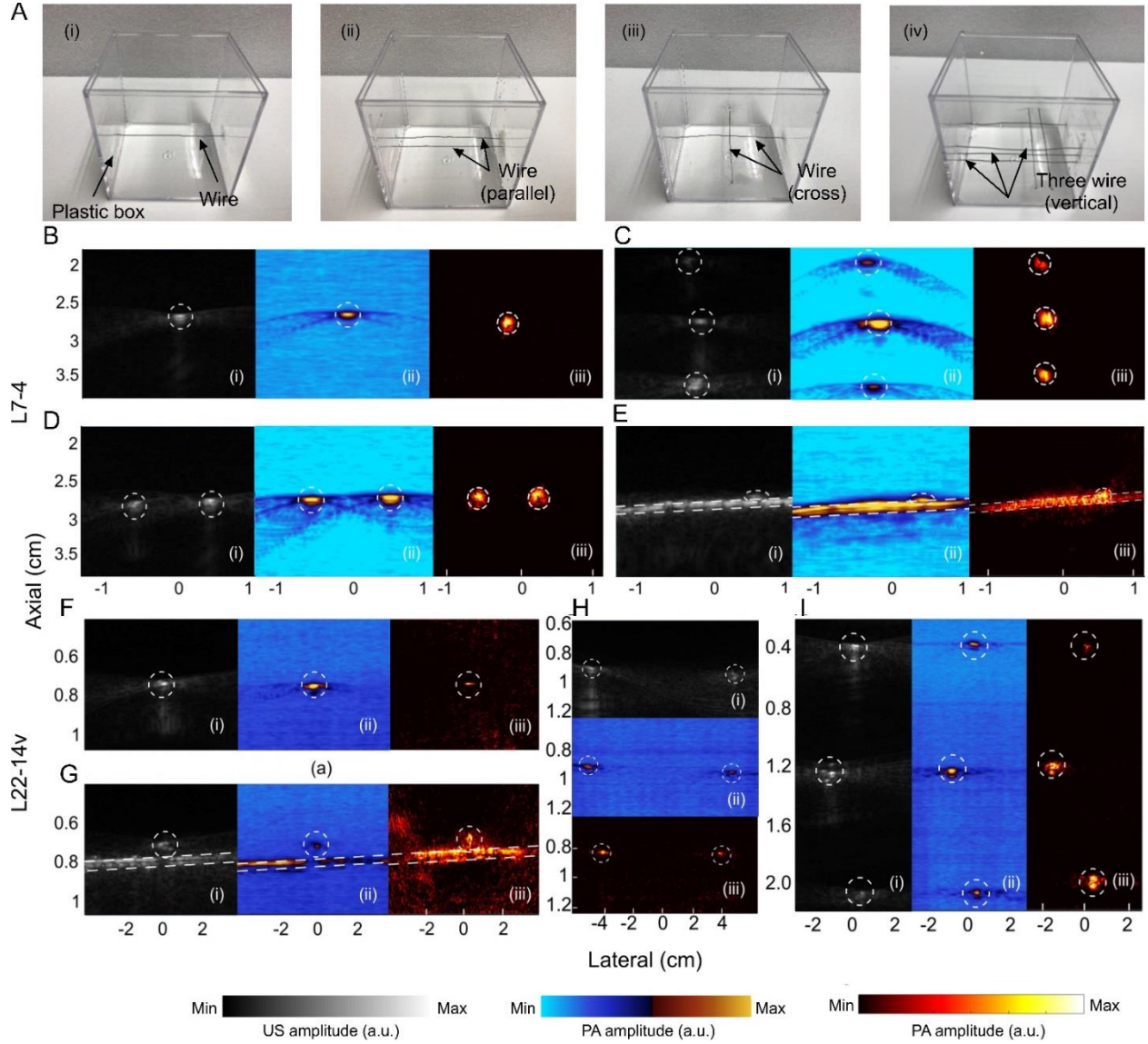


**Figure 16. DS-DMAS reconstruction against Verasonics standard US and PA.** Comparison of the performance of DS-DMAS to Vantage PA reconstruction and Vantage US reconstruction. (A) Wire phantoms for resolution study, (i) one-wire, (ii) two-wire, (iii) two-wire cross, and (iv) three-wire. (B-I) US and PA images from L7-4 and L22-14v probes where reconstructions are (i) Verasonics default ultrasound, (ii) Verasonics default photoacoustic, and (iii) Photoacoustic (DS-DMAS). L7-4 probe (B) single wire cross section, (C) 3-wire cross section, (D) 2-wire cross section, and (E) 2-wire cross. L22-14v probe: (F) single wire cross section, (G) 2-wire cross, (H) 2-wire cross section, and (I) 3-wire cross section. Images of the targets are shown in white circles or straight lines.

## 2.5 Discussion and conclusions

Photoacoustic imaging is a complement to the established US imaging and may significantly increase its scope of application in diagnostic imaging and therapeutic monitoring. Combining with commercial medical US systems, the development of PAI can be accelerated by taking advantage of US image reconstruction and processing. Moreover, PAI results can be more easily reproduced between laboratories when realized with commercially available US machines.

Among different configurations, linear-array PAI is becoming popular, mainly because linear-array US transducers can easily be manufactured, hence the production cost is lower as compared to custom-made curved or ring arrays [93, 94]. Moreover, these transducers are commonly used in clinical applications hence the PAI system built on top of it, will have a high clinical translatability.

We discussed details of US/PA imaging system setup implemented on Vantage research system, sequencing of the US/PA signal generation, and the related data processing protocols. Although the Verasonics Vantage System has many capabilities and advantages, it has some limitations. The transducer connector limits which transducers can directly connect to the system. Verasonics offers some connector adapters to alleviate this problem, but it can make switching between transducers cumbersome. Another limitation is that the signal pre-amplification occurs far (~1-2 meters) from the probe which increases the noise level for weak PA signals. Further, the maximum sampling rate of the system is 62.5MHz which limits the frequency of transducer that can be used. The L22-14v operating frequency is lowered to 15.625MHz so that the Nyquist limit can be met. Higher frequency probes cannot be used. This is

significantly lower than the 500MHz sampling rate of the NI PXIe -1078 DAQ (National Instruments, Austin, TX, USA).

## CHAPTER 3: A NOVEL METHOD TO AVOID THERMAL DAMAGE IN PHOTOACOUSTIC IMAGING

In this Chapter, we study the laser-induced thermal damage on mouse skin *in vivo*, using two available 532nm lasers with repetition rates of 10Hz and 30Hz. Damages to skin are confirmed using histology report of the biopsied tissue samples. Further, we simulate the thermal damage at other laser energies, wavelengths, and repetition rates that are not permitted (above the American National Standards Institute (ANSI) limit) or were not available in the lab. Further, we propose a cooling method to significantly reduce the initial temperature of the tissue in order to avoid tissue damage when high energy lasers are used with a high repetition rate.

### 3.1 Introduction

Photoacoustic imaging (PAI) is an emerging hybrid modality with great potential for clinical translation. PAI works in the photothermal regime, where a high energy short laser pulse is absorbed by tissue chromophores, generating pressure waves through the thermoelastic effect [1]. These waves are detected using ultrasound transducers, given to an image reconstruction algorithm, to form an image.

A laser with a high energy or a long exposure time (thresholds defined as ANSI limit [95]) damages the tissue through either thermal and/or mechanical damage mechanism. Here, we study only the laser-induced thermal tissue damage and propose a way to avoid that.

The photothermal reaction proceeds in two steps: first, the absorption of a photon of energy,  $h\nu$ , (e.g., Nd:YAG laser: 1.2 eV that exceeds by far the kinetic energy of a molecule at room temperature which is about 0.025 eV), promoting X to a vibrational excited state  $X^*$  (increased molecular vibrations); and second, an inelastic scattering

occurring at 1-100ps time-scale with a collisional partner XX, belonging to the surrounding medium, lead to a deactivation of  $X^*$  and a simultaneous increase in the kinetic energy of XX [96].

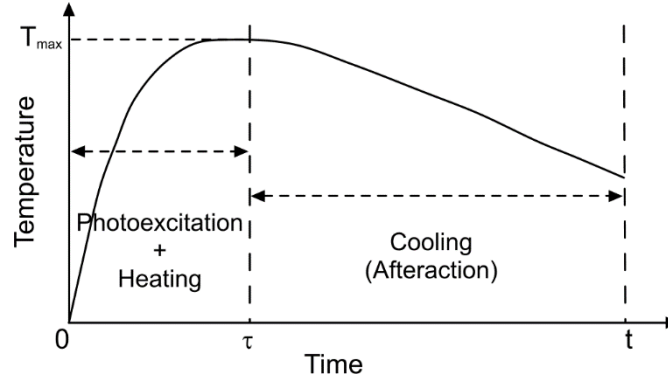


**Figure 17. Temperature rise profile in biological tissue due to laser exposure.**

The heat transfer process in living tissue is complicated because of the involvement of the heat conduction between blood and tissues, blood perfusion in vascular beds and metabolic heat generation. An effective bio-heat transfer model that includes effects of the capillary vessel systems, the metabolism and the relaxation time of temperature gradient and heat flux is expressed in [97]:

$$\rho C \frac{\partial T}{\partial t} + \rho C \hat{u} \cdot \nabla T + \nabla \cdot (-k \nabla T) = \rho_b C_b \omega_b (T_b - T) + Q_m + Q_L \quad (1)$$

where,  $\rho$  and  $\rho_b$  represent the density of the human tissue and the blood.  $c$  and  $c_b$  are specific heat of the tissue and blood.  $\omega_b$  is the blood perfusion in the human tissue.  $k$  is the thermal conductivity,  $T_b$  represents the arterial blood temperature.  $Q_m$ , represents heat production rate caused by metabolism and  $Q_L$  is external heat source (i.e., laser).

For a single laser pulse,  $Q_L$  can be written as:

$$Q_L = \mu_a \phi \quad (2)$$

where,  $\mu_a$  and  $\varphi$  are the absorption coefficient of material and the optical fluence, respectively. In biological tissues,  $\varphi$  can be approximated in the following form:

$$\varphi(r, z) = (1 - R)E(r)e^{-\mu_t z} \quad (3)$$

where,  $R$  represents the optical reflection ratio of the human tissue,  $\mu_t$  represents the optical attenuation coefficient,  $z$  is axial depth into the tissue. The energy profile of a laser source at  $r$  is defined in [98] as,

$$E(r) = \frac{E}{\pi t_p^2} e^{-2r^2/t_p^2} \quad (4)$$

where  $t_p$  is the half width half maximum (HWHM) of a Gaussian laser pulse profile and  $E$  represents total emitted energy. The temperature rise due to a laser pulse is [99, 100]:

$$\Delta T(r, z) = T - T_0 = \frac{Q_L}{\rho C} = (1 - R) \frac{\mu_a}{\rho C} \frac{E}{\pi t_p^2} e^{-2r^2/t_p^2 - \mu_t z}. \quad (5)$$

Normal temperature in biological tissues is  $\sim 37^\circ\text{C}$ . Hyperthermia ( $\sim 45^\circ\text{C}$ ) results from weakening or destruction of molecular bonds and alterations in membrane structures. However reversible, some of the impacts of hyperthermia are edema of the basal layer, subepidermal cleft formation, and slough. If such a hyperthermia condition persists for several minutes, the tissue will undergo necrosis (death of living cells or tissue). Starting around  $50^\circ\text{C}$  there is a noticeable reduction in enzyme activity. This effect results in cell immobility, reduced energy transfer in the cell, and a diminishing of certain cell repair mechanisms. Depending on the duration and the peak value of the temperature increase, the resulting effects include coagulation ( $> 55^\circ\text{C}$ ) due to the denaturation of proteins and collagen, vaporization of the water molecules ( $\sim 100^\circ\text{C}$ ),

carbonization ( $> 100^{\circ}\text{C}$ ), and melting ( $> 300^{\circ}\text{C}$ ). Laser-induced photoacoustic temperature rise that is studied here is before and within  $45^{\circ}\text{C}$ , therefore we only experience hyperthermia if tissue temperature rises.

### 3.2 Materials and methods

We used two high energy lasers: (i) an Nd:YAG pump laser with a repetition rate of 10Hz, a pulse width of 8.5ns (LPS-532-L, CNI Optoelectronics Tech. Co., Changchun, China); (ii) Another Nd:YAG pump laser with a repetition rate of 30Hz, a pulse width of 8ns (PRO-270-30H, Spectra-Physics, CA, USA). Due to the beam divergence in laser (i), we had to use a converging lens (AC508-100-A-ML, Thorlabs, NJ, USA). The beam diameter on the animal for both lasers was 6mm diameter, and the energy level was  $20\text{mJ}/\text{cm}^2$ . The experimental setup made with both lasers are shown in Figure 18A. For temperature measurements, we used an infrared (IR) camera (Sc6700, FLIR, MO, USA) with a 25mm focal length lens placed directly in-line with the surface of the target. Image acquisition by the IR camera was synchronized with the laser trigger. Figure 18B demonstrates an example thermal image taken of one mouse during illumination.

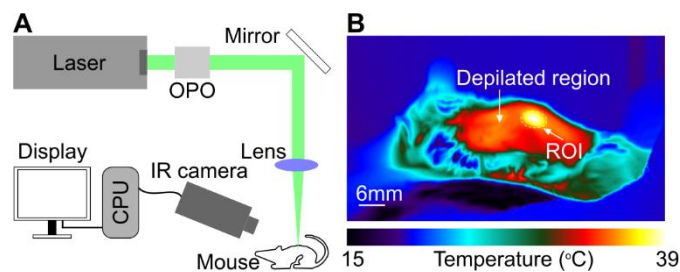


**Figure 18. Thermal imaging setup.** (A) Schematic of *in-vivo* experimental setup, (B) Thermal image of a live mouse when exposed to laser.

Five 4-month old, ~25g, healthy male mice (CD-1, Charles River, MA, USA) were used in this study. Animal protocols were approved by the Institutional Animal Care and



Use Committee (IACUC) and animal handling was performed according to the guide provided by Division of Laboratory Animal Resources (DLAR) at Wayne State University. Full anesthesia was maintained throughout the experiment by using isoflurane gas, administered with 500mL/min of oxygen and 2.50% of isoflurane (VetOne, Boise, ID, USA) and laid on a temperature regulating water blanket to maintain their equilibrium body temperature. The hair near the abdominal region were depilated. One mouse was exposed to laser (i) for 300s. 3 mice were exposed to laser (ii), each for 20, 60, and 300s respectively. The fifth mouse was exposed to laser (ii) for 300s through a cooling bag. For cooling, a thermally conductive plastic bag filled with cold water (15°C) was placed on the region of interest. A thermal sensor (TSP01, Thorlabs, NJ, USA) was used to check the water temperature.

The laser exposed areas were biopsied after 48 hours. Punch biopsies were performed using a 3mm punch (33-32, Integra Miltex, Plainsboro, NJ) and placed in a formalin cup. Two biopsies from separate locations (exposed and control) were taken from each mouse.

For simulation studies, initially, we used MCX software [56] to calculate the fluence inside a single-layer skin tissue, with the dimension 20mm×20mm×8mm (length×width×depth). Figure 19 shows the absorption and scattering coefficients of skin [101] at different wavelengths used for the simulations. Refractive index,  $n=1.37$  and anisotropy factor  $g=0.9$  at all wavelengths. We used a collimated uniform beam with a diameter of 6mm illuminated top center of the sample with  $10^8$  photons for simulation purposes.

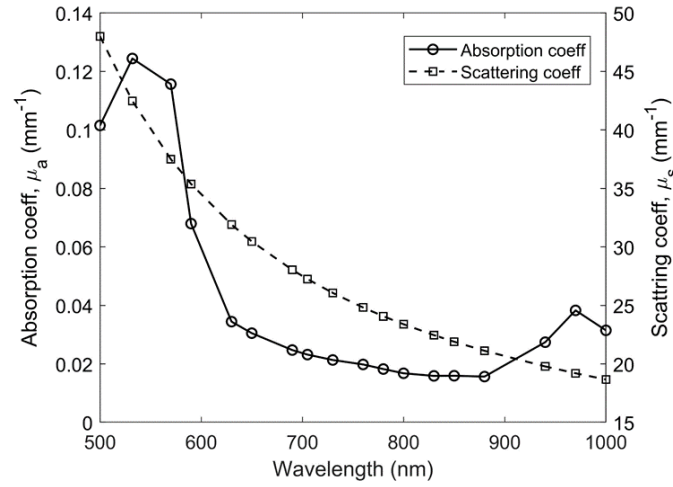


**Figure 19. Absorption and scattering coefficients of skin**, used for simulations at different wavelengths.

The normalized absorbed light energy,  $E_n$ , was calculated in the tissue. The absorbed energy corresponding to a specific pulse energy will be  $E = E_n \times E_p$  where  $E_p$  is the energy of a single pulse. The temperature change due to a single pulse can be calculated by equation (6),

$$\Delta T_p = E_p / \rho c V_{vox} \quad (6)$$

where  $\rho$  and  $c$  are density and specific heat capacity, respectively and  $V_{vox}$  is the volume of a voxel. The next step is the heat transfer simulations. We used *kWaveDiffusion* from k-wave software library [102] which solves the bio-heat equation (Equation (1)). We defined a similar domain to that we used for light simulations with the same voxel size. The initial temperature for all the voxels was set to 32.5°C. The same as the initial temperature of the mouse skin in the experiment. The time step used in the heat simulation was 0.02s. To take into account the effect of pulsed laser illumination,  $\Delta T_p$  was added to the current temperature at right intervals according to the laser repetition rate. Currently, k-wave does not support the surface heat transfer, thus we

had to implement heat transfer at the boundary manually to take into account the cooling effect due to the air convection. At each time step, we updated the temperature of the surface voxels by:

$$\Delta T_{conv} = Q_{conv} / \rho c V_{vox} = h A_{amb} (T_{amb} - T) dt / \rho c V_{vox} \quad (7)$$

where  $h$  is the heat transfer coefficient,  $A_{vox}$  is the face area of a voxel,  $T_{amb}$  is the ambient temperature and  $T$  is the current temperature of the surface voxel.

**Table 8. Thermal simulation parameters used.**

Parameter	Value
$E_p$ (mJ/cm <sup>2</sup> )	26
$\rho$ (kg/m <sup>3</sup> )	1000
$c$ (J/kg.K)	3400
$k$ (J/m.K)	0.3
$\rho_b$ (kg/m <sup>3</sup> )	1000
$c_b$ (J/kg.K)	3600
$\omega_b$ (1/s)	0.001
$T_b$ (°C)	37
$h$ (W/m <sup>2</sup> .K)	10
$T_{amb}$ (°C)	16

### 3.3 Results

#### 3.3.1 In vivo experiments

We used laser (i) with the setup shown in Figure 18A, created a homogenized spot with a diameter of 6mm on the abdominal region of the mouse. By adjusting the IR camera lens, we put the imaging target at the focus of the IR camera, about 4cm away. A small region of interest (ROI) was selected and the averaged pixel intensity of the ROI was reported as the temperature of the target (see Figure 18B). Before the laser exposure, the target temperature was at ~32.4 °C. The temperature fluctuation occurred due to the respiratory movement of the mouse (i.e., the outliers) was removed by fitting an 8<sup>th</sup> order polynomial function to the temperature profile. The temperature

rise profiles and fitted functions for laser (i) and laser (ii) in the course of 300 seconds are plotted in Figure 20A. The temperature change rates in the first 10s for laser (i) and (ii) were  $\sim 0.09^{\circ}\text{C/s}$  and  $\sim 0.23^{\circ}\text{C/s}$  respectively as shown in Figure 20A with dotted lines. The damage threshold is also drawn with a dashed line.

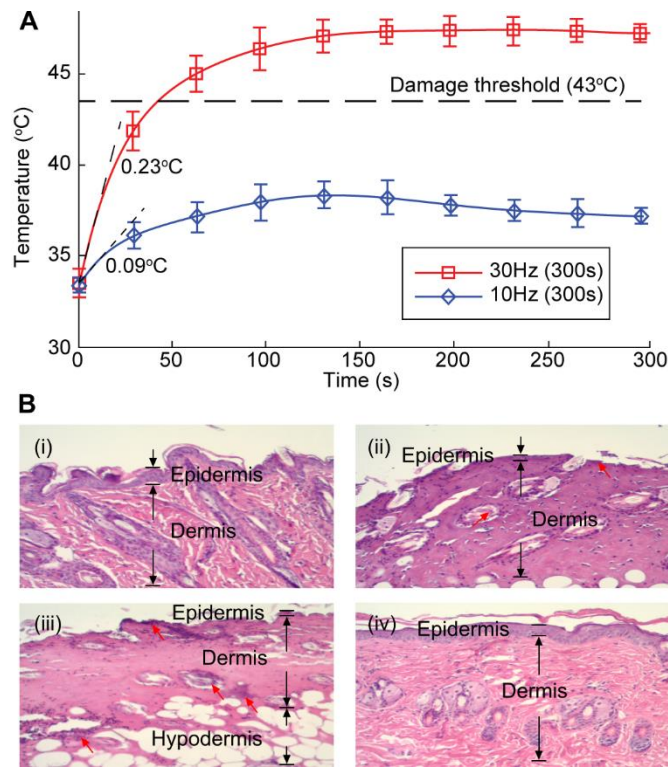


**Figure 20. No cooling irradiation results.** (A) Temperature rise profile for different repetition rate (10 & 30 Hz) for 5 minutes, (B) Histology of biopsied mouse skin 48 hours post irradiation using (i) 10Hz laser for 5mins, (ii) 30Hz laser for 5mins, (iii) 30Hz laser for 60s, (iv) 30Hz laser for 20s. Red arrows showing necrosis region.

The irradiated tissues by both lasers were biopsied 48 hours post irradiation. The histology results showed no damage in the sample illuminated by laser (i) but indicates necrosis in the tissue illuminated by laser (ii). Necrosis is an irreversible phenomenon. We reduced the duration of the illumination of laser (ii) from 300s to 60s and 20s. In all cases but 20s, the tissue experienced necrosis (see Figure 20B). Usually to improve the quality of PA image of a certain cross-section or deeper imaging, we repeat the PA

imaging multiple times, and perform averaging. Therefore, increasing the duration of the PA imaging experiment without damaging the tissue is essential. We proposed a cooling protocol to significantly reduce the initial temperature of the tissue. This prevents tissue from damage in longer durations of a high repetition rate laser such as laser (ii). We tested this method for the longest period that we used laser (ii), i.e., 300s. We measured the initial temperature of the tissue to be  $\sim 33.8^{\circ}\text{C}$ . The cooling bag was placed on the imaging area for 60s, which brought down the tissue temperature to  $\sim 26.6^{\circ}\text{C}$ . The temperature of the area was measured again after 300s, the temperature raised to  $\sim 31.2^{\circ}\text{C}$ . We observed no irritation, and in the histology results there was no sign of tissue damage (see Figure 21B). A summary of the laser irradiation experiments and their corresponding histology results have been listed in Table 9.

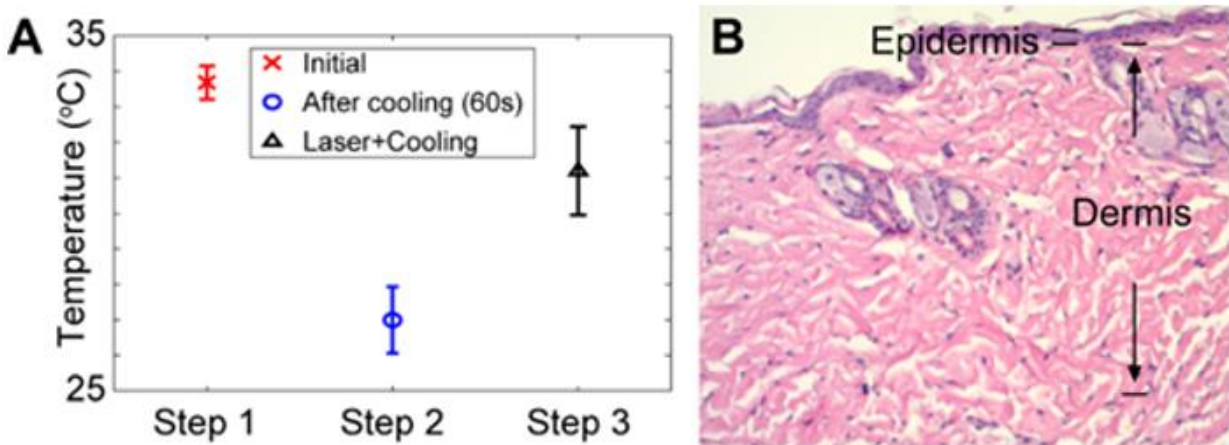


**Figure 21. Irradiation with cooling results.** (A) Effect of cooling the region of interest and corresponding temperature rise, Step 1: Initial temperature, Step 2: Temperature decrement after 60s cooling, and Step 3: Temperature increment after laser exposure through cooling bag at 30Hz for 300s, and (B) Histology of 48 hours post irradiation biopsy to 30Hz laser with exposure time 5mins through cooling bag.

**Table 9. Laser irradiation process and biopsy results.**

Sample no.	Frequency (Hz)	Irradiation Duration (s)	Biopsy result
1	10	300	No

			change
2	30	300	Necrosis
3	30	60	Necrosis
4	30	20	No change
5	30 (wc)	300	No change

\*Fluence: 20mJ/cm<sup>2</sup>, wc: with cooling

### 3.3.2 Simulation results

To find the proper values for simulation parameters we adjusted values  $E_p$ ,  $h$  and  $\omega_b$  and compared the simulation results at 532nm with experiments until we observed similar behavior for the time interval of 60s which is the desired time for real applications. In this way we know that our model is describing the heat problem correctly in the defined time interval. Figure 22 compares the best simulation results with experimental data. The corresponding values are  $E_p = 7.5\text{mJ}$  (26mJ/cm<sup>2</sup>),  $h = 10\text{J/m}^2\text{K}$  and  $\omega_b = 0.001\text{s}^{-1}$ , and the same values reported in Table 8 were used.

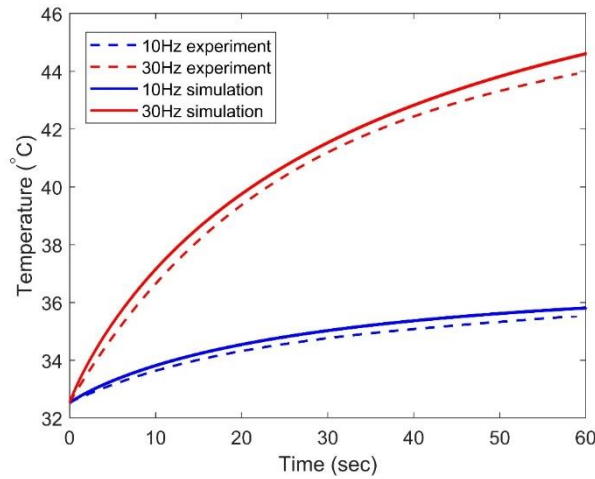


**Figure 22. 532nm experimental/simulation comparison.** Comparison of simulation results (solid lines) with experimental data (dashed lines) for 10Hz (blue) and 30Hz (red) at 532nm with  $E_p=26(\text{mJ/cm}^2)$ ,  $h=10 (\text{J/Km}^2)$  and  $\omega_b=0.001(\text{s}^{-1})$ .

After validating the model at 532nm, we studied temperature rise at different wavelengths from 500nm to 1000nm by repeating the light simulation with

corresponding optical properties followed by heat simulation in the 60s interval. We also studied the effect of changing repetition rate on the temperature rise. Figure 23A shows the final temperature at  $t=60s$  for different wavelengths and for different repetition rates. At higher repetition rates the temperature increases very fast and thus the energy should be lowered. Next, we changed the individual pulse energy,  $E_p$ , and studied the temperature rise for two repetition rates 10Hz and 30Hz. Figure 23B shows the final temperature after 60s for 10, 20, 26, 40 and 50 mJ/cm<sup>2</sup>.

It is evident that as wavelength increases, the temperature rise is decreased which is due to the lower light absorption coefficient. The results also suggest that the change in temperature is a function of total energy received by the sample in a time interval which is the product of the pulse energy and repetition rate. If the repetition rate doubles while the energy is halved, the results will be the same.

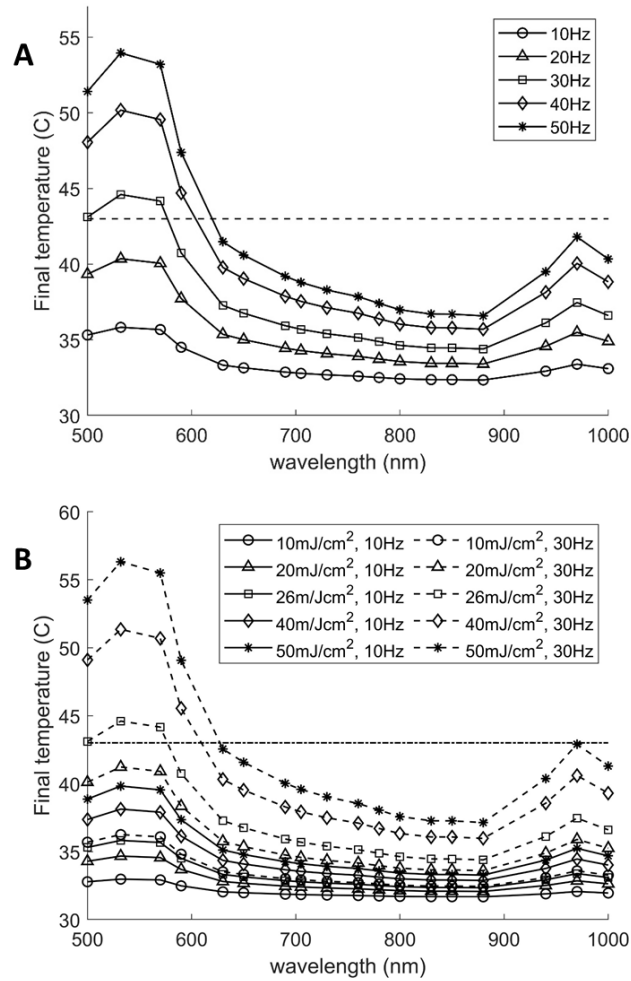


**Figure 23. Simulation results for varied pulse repetition rate and pulse energy.** Final temperature rise after 60s of laser irradiation at different wavelengths. (A) Different repetition rates with pulse energy=10(mJ/cm²), (B) Different pulse energies for repetition rates 10Hz and 30Hz. The dashed horizontal line shows the damage threshold, 43°C.

According to Table 9 and Figure 23 to avoid necrosis either temperature rise must be reduced or the energy received by the tissue. Alternately, we showed that a pre- or parallel-cooling method can be utilized to reduce the temperature at the epidermis while maintaining sufficient deposited energy at the target. Until now we only considered heat transfer by air free convection ( $h=10\text{W/cm}^2\text{K}$ ). By applying the cool water bag, we in fact, increased the heat transfer coefficient,  $h$ , and cooling the tissue more due to greater heat exchange between the skin surface and to surrounding



medium according to equation (4). In the next set of simulations we used heat transfer coefficient  $h=10, 20, 50, 100$ . Different values of  $h$  can be achieved in real application by changing cooling medium i.e. air or water and by externally circulating the cooling medium resulting in forced convection. The pulse energy was kept constant at  $26\text{mJ/cm}^2$  and the repetition rate set to  $30\text{Hz}$ . Figure 24 shows the final temperature at  $t=60\text{s}$  for different values of  $h$  at different wavelengths. It can be seen that by increasing the surface cooling, final temperature reduces significantly below damage threshold. It allows for an increase in light energy.

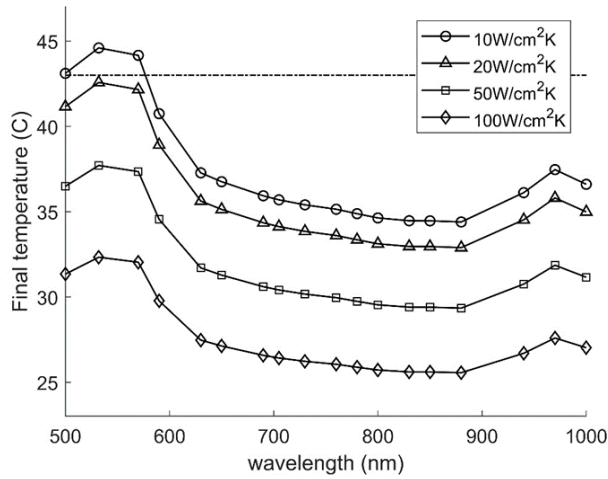


**Figure 24. Simulation results for various heat transfer coefficients.** Final temperature rise after 60s of laser irradiation for different heat transfer coefficients at different wavelengths. The dashed horizontal line indicates the damage threshold at  $43^\circ\text{C}$ .

### 3.4 Discussion and conclusions

One of the main issues in the clinical translation of PAI is to determine the maximum permissible level of exposure (MPLE). Since, the tissue thermal response is a complex phenomenon and requires several critical parameters to be considered simultaneously, it is not feasible to determine MPLE accurately using optical-thermal models which are available in the literature. Hence, we tested the temperature change

over time experimentally to help understanding thermal-tissue response. We demonstrated that there is microstructural deformations in dermis or epidermis of mouse skin *in-vivo* when illuminated by the laser light with 30Hz repetition rate whereas 10Hz frequency does not appear to have any damaging effect. These results are verified from the histology of the biopsied samples 48 hours post laser irradiation. Further, using the thermal-tissue simulation model, we investigated repetition-rates and energy levels of the laser that were not possible to explore *in vivo*. We also presented a parallel-cooling technique that enables the usage of near MPLE for SNR enhancement and used simulations to investigate the effect of cooling by changing heat transfer coefficient.

## **CHAPTER 4: DEVELOPMENT OF TRANSFONTANELLE PHOTOACOUSTIC IMAGING**

In this chapter, we describe the development, optimization and evaluation of a novel TransFontanelle Multispectral Photoacoustic Imaging (TFMPI) method, a sensitive, compact, portable, and safe imaging modality, to study pathophysiology, and to improve the detection of brain hemorrhage. TFMPI detects intracranial hemorrhage (ICH) earlier, with higher sensitivity and specificity than US; has no need for sedation, radiation or radionuclides; and, provides images with excellent spatial resolution and penetration depth.

### **4.1 Introduction**

Intracranial hemorrhage (ICH) occurs at a rate of approximately 3.5 times per 1,000 live births, and is the most common neurological disorder of newborns [103, 104]. ICH has many causes, e.g., prolonged or precipitous delivery, vaginal breech delivery, instrumental delivery, use of forceps or vacuum extraction, and primiparity or extreme multiparity [105-114]. Neonates with low gestational age and/or with low birth weight (<1500g) are also at high risk for ICH [114]. Improving medical interventions have increased the survival of low gestational age and low birth weight infants, meaning the potential number of infants with ICH from these causes is increasing [115-118]. There are several types of ICH: sub-ependymal (SEH), intraventricular (IVH), and subarachnoid (SAH) hemorrhages being the most common in neonates [119, 120]. SEH and IVH are also identified as Germinal Matrix Hemorrhage (GMH). SEH, IVH and SAH all lead to blood mixing with cerebrospinal fluid (CSF) [121, 122]; this may cause hydrocephalus [123, 124]. Intraparenchymal hemorrhage (IPH), is bleeding into brain tissue, and is a precursor for vasogenic edema. Based on the current diagnostic

approaches, at least one type of neonatal ICH occurs in ~25% of newborns [125-128]. In addition, many sub-clinical cases remain undiagnosed due to limitations of current diagnostic imaging technologies may or may not manifest by obvious neurological deficit symptoms. Significance of brain injury is dependent on severity, duration and location of hemorrhage [129, 130]. Ultimately, up to 85% of survivors of neonatal brain hemorrhage will exhibit major cognitive dysfunction; the majority of which eventually having special educational needs [131, 132]. Therefore, accurate, early detection, classification and diagnosis of ICH is essential for brain injury reduction, prognostication, and optimal treatment [120, 133, 134].

TransFontanelle ultrasound imaging (TFUSI) is the current standard of care diagnostic modality that can detect grade III-IV intraventricular [128] hemorrhage (IVH) (or brain hemorrhages larger than 5 mm [135]) with sensitivity of nearly 100% and specificity of 93.3% [135]. However, TFUSI has very low sensitivity and even lower specificity (i.e., 0-5%) for detection of hemorrhages <5mm, IVHs of grades I-II, diffuse subarachnoid hemorrhage (SAH) (without obvious blood clots in the normal-size brain ventricles and cisterns), and small cerebral or extra-axial hemorrhages, with unknown long-term consequences. TFUSI is also limited in detection of low concentration blood in CSF, i.e., <10% [115, 135], and unable to detect vasogenic edema following hemorrhage or ischemia/reperfusion injury [136]. Although definitive diagnosis of SAH can only be made by detection of blood in CSF obtained by a lumbar puncture, it is not used as a standard of care for infants due to significant trauma and potential complications. In contrast, these second stage diagnostic tools, magnetic resonance imaging (MRI), computed tomography (CT) and positron emission tomography (PET)

[137] have high sensitivity and specificity for detection brain hemorrhages. However, they are not used as frontline modalities for routine screening of preterm infants, because MRI takes a long time (~1 hour), CT utilizes ionizing radiation, and PET requires a positron-emitting radionuclide. These modalities require transporting clinically unstable newborns out of the Neonatal Intensive Care Unit (NICU), often require sedation that is associated with risks (i.e. hypotension, hemodynamic changes, or allergic reaction [138]), and have relatively high cost. Small MRI units that have been installed and tested in a few NICUs are expensive and still require sedation during imaging [139]; therefore, have not been widely adopted in neonatal clinics. Near infrared spectroscopy (NIRS) can potentially assist clinicians in assessing functional changes in cerebral perfusion and oxygenation [140-142], but it has a poor spatial resolution, especially for the small neonate head, and poor penetration depth, which both limit its use to cortical mapping [143]. Moreover, NIRS requires the attachment of cumbersome head caps to accommodate multi-channel fiber optic cables. Photoacoustic Imaging is a promising technique that provides noninvasive detection of structural, functional and molecular anomalies in biological tissue [144]. A nanosecond laser pulses can illuminate the tissue at the wavelengths that the endogenous chromophores, e.g., oxy-hemoglobin (HbO) and deoxy-hemoglobin (HbR), or exogenous contrast agents have the highest absorption [6, 145]. Photoacoustic imaging of the brain can simultaneously provide high-resolution images of the brain vasculature and hemodynamics [13, 146].

## 4.2 Materials and methods

### 4.2.1 Equipment specifications and Wavelength Selection

The following equipment was used for the fluence decay, resolution, and sensitivity sections. Quanta Pro laser (Nd: YAG) from Spectra Physics has been used as the laser source. A repetition rate of 30Hz and a pulse width of 8ns is used in this study. The optical parametric oscillator GWU Versa Scan has been used to tune the wavelength. This tunable laser has a range from 410 – 1100nm with a maximum energy of 100mJ. We used Graded Index Plastic Optical Fiber (PMMA) for delivering light. The fibers are flexible and have a diameter of 2mm. The length of each fiber is about 2 meters. 40 fibers are placed in the bundle. The design of the light illumination is based on reaching the most optimum light delivery. A customized 3D printed probe tip has been used which can accommodate a single row of 20 optical fibers on each side. They are inserted through the probe tip rails. At the distal end, the optical fibers were bundled using an in-house cylindrical holder. For the oxygenation, *ex-vivo* sheep brain imaging, brain reconstruction improvement, and edema imaging sections we used a different bifurcated optical fiber bundle of rectangular, tightly packed 100µm fibers (Fiberoptics Inc. Technology) with the Opotek PhocusMobil Nd:YAG laser. We have illuminated the fontanelle area with an average of 15mJ/cm<sup>2</sup> at 570nm for fluence decay and sensitivity sections. Illumination wavelengths for oxygenation study were 750 and 800nm. For Evan's Blue study, we have used 690nm for Evan's Blue and 570nm for hemoglobin. These wavelengths were chosen due to high absorption coefficient of hemoglobin and Evan's Blue, respectively, as well as optimal quantification of blood oxygenation. We measured the laser energy using an energy meter (Gentec Integra, USA) that was

connected to a laptop to acquire and store energy log for further normalization. The software used for reading and storing the energy data was PC Gentec-EO. The photoacoustic probe was placed on a custom made x-y manual translation stage. The ultrasound probe used in this study is a 128-element linear array (ATL/Philips L7-4 with 5MHz central frequency). The photoacoustic signals are acquired using 128-channel high frequency ultrasound system (Vantage, Verasonics Inc). The acquisition system was triggered directly from the laser power supply. Authors have developed a MATLAB code to acquire the ultrasound and photoacoustic signal in A-scan and produce B-mode images that is compatible with the Vantage 128 and the L7-4 probe. An eventual design for the TFMPI probe is seen in Figure 25.

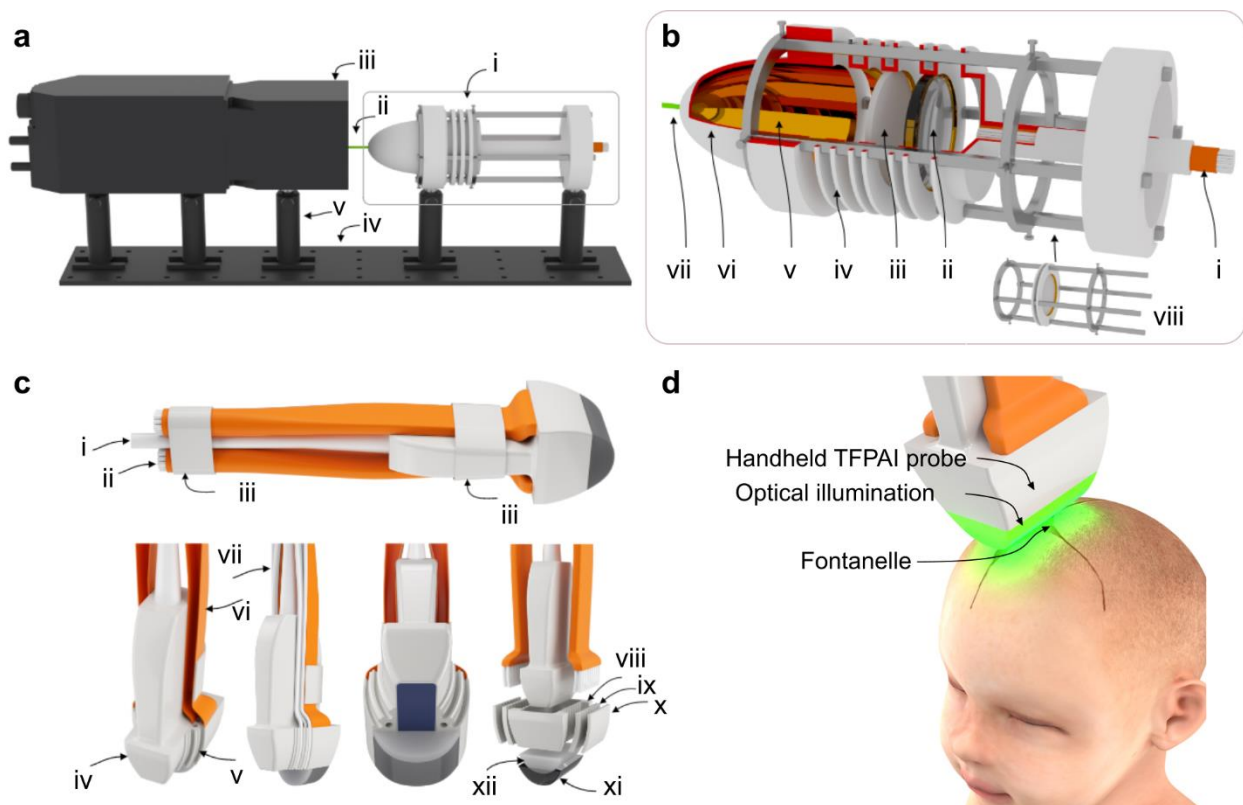


**Figure 25. TFMPI probe and associated optics.** (A) Optical setup of laser light coupling to fiber bundle with (i) laser light coupling optics, (ii) laser light, (iii) laser system head, (iv) optical breadboard, and (v) optical post and post holder. (B) Laser light coupling optics cut section view with (i) fiber optic cable bundle, (ii) convex lens, (iii)

diffuser, (iv) spacer, (v) parabolic reflector, (vi) thin silver coating, (vii) laser light, and (viii) horizontal cage system. (C) TFMPI probe including (i) ultrasound data cable, (ii) fiber optic cable bundle, (iii) flexible strap, (iv) linear array transducer, (v) fiber optic cable housing, (vi) fiber optic bundle housing, (vii) fiber optic cable bundle, (viii) main body, (ix) inner fiber optic cable holder, (x) outer fiber optic cable holder, (xi) soft tip, and (xii) Aqualene® coupler. (D) Rendering of TFMPI probe in use.

#### 4.2.2 Development of simulation model

Prior to acquiring a more uniform illumination bifurcated fiber bundle, we performed an intensive simulation study on optimal illumination design with larger diameter individual fibers. The first step was to find the light intensity profile on a surface coming out from a single fiber for different combinations of optical fiber parameters. A 2-D model was designed and a schematic has been shown in Figure 26. An ultrasound transducer is placed at the center of the fontanelle. The fontanelle area was considered as a 20×20mm square.

Fiber diameter,  $D$ , and numerical aperture,  $NA$ , are two more parameters of the optimization problem. Parameter values we used in the simulations are as follows; 1)  $D = 0.5, 1.0, 1.5, 2.0$  and  $2.5$  mm, 2)  $NA = 0.1, 0.2, 0.3, 0.4$  and  $0.5$  covering a wide range for both glass and plastic optical fibers, 3)  $\theta$  or angle of illumination with normal to tissue was set to 0 (perpendicular), 10, 20, 30, 40, 50, 60 degrees. 4)  $H$  or height of the fibers from the surface of the tissue was set to 5, 6, 7, 8, 9 and 10mm. For each combination of parameters we performed Monte Carlo simulations based on geometrical optics and assumed that diffused light was coming out from the core of the optical fiber with a maximum divergence limited by the numerical aperture. These assumptions were based on the fact that core diameters were much larger than the wavelength and the input light is diffused since the laser beam has passed through a diffuser. The illuminated surface is divided into pixels with area  $da=0.1 \times 0.1 \text{ mm}^2$  creating a grid. The number of photons



hitting the surface was integrated over each pixel to give us the deposited energy,  $E$ , and intensity,  $I=E/da$ . These simulations were done using a custom code written by the authors. Considering a 0.5mm separation between fibers, the number of fibers in a row for core diameters 0.5, 1.0, 1.5, 2.0 and 2.5 mm were set to be 19, 13, 10, 8 and 7, respectively, so all the rows have the same length. Then we calculated the resulting intensity profile of a row for different parameter sets, by translating and adding up the intensity profile of a single fiber corresponding to each parameter set. The third step was to construct the probe with different numbers of rows and different configurations. With addition to the number of rows we also introduced the parameter  $L$  which is the distance between the first row and transducer axis with values 5, 6, 7, 8, 9 and 10mm. This enables us to accommodate transducers with different widths ranging from 10 to 20mm. The separation between different rows was also considered to be 0.5mm and the maximum number of rows at each side of the transducer were decided based on the core diameter. For diameters 0.5, 1.0, 1.5, 2.0 and 2.5mm the maximum number of rows were set to 9, 6, 5, 4 and 3 respectively. The width of the probe was not allowed to exceed 4cm in any configuration. Additionally, square and honeycomb configurations were considered. Some example configurations that were simulated are shown in Figure 26.

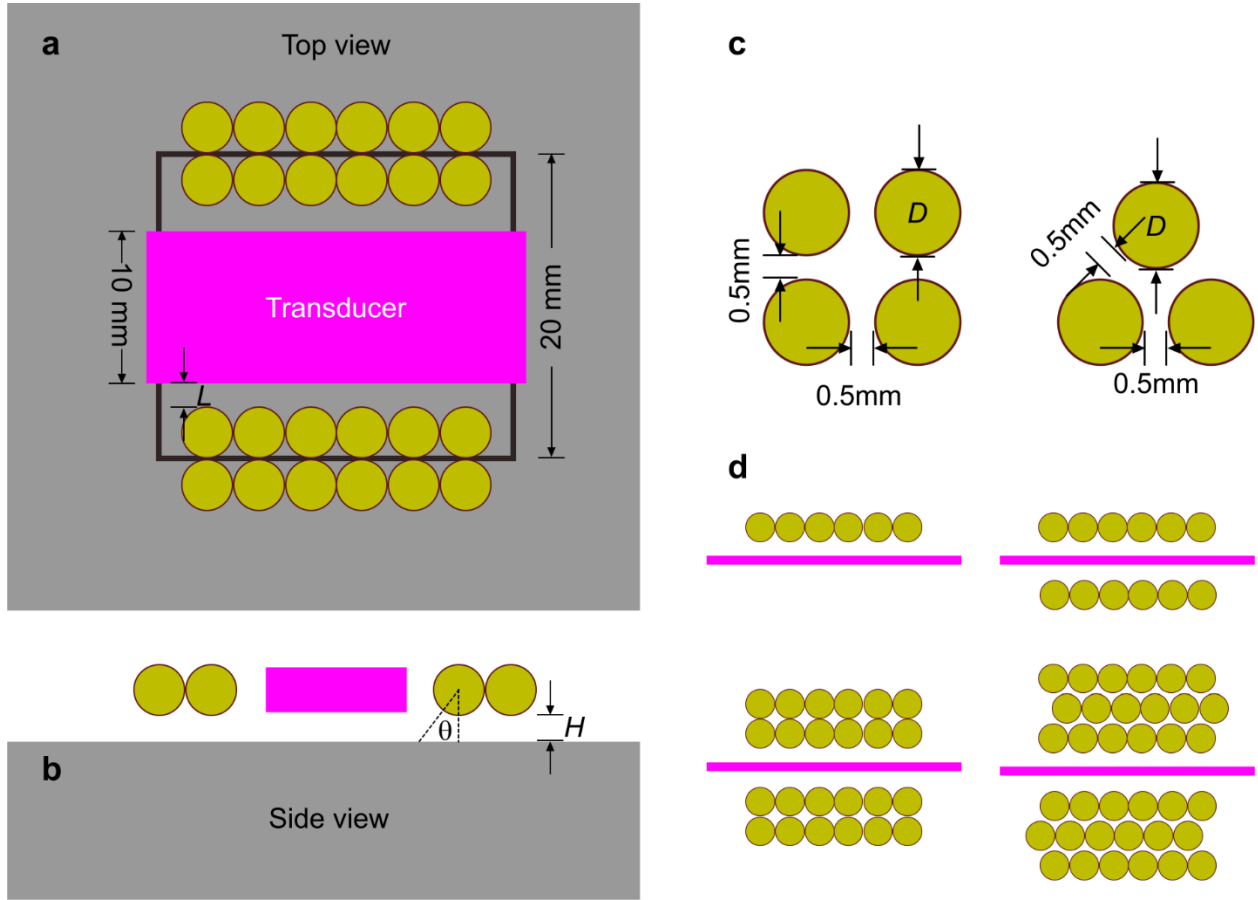


**Figure 26. Example TFMPI optical fiber configurations.** (A) Top view: an ultrasound transducer is placed at the center of fontanelle (grey rectangle within black square) and optical fibers (yellow circles) are located at sides act as light sources. Fontanelle area is considered as a 20×20mm square (dashed grey box). Distance from transducer wall and first row is  $L$ , (B) Side view: the distance between fibers and tissue surface is  $H$  and bending angle of fibers is  $\theta$ , (C) additionally fiber diameter,  $D$ , and fiber positioning in square (left) and honeycomb (right) configurations is evaluated. Separation between adjacent fibers is 0.5 mm in both cases. (D) Different probe configurations, one row at one side (top left), one row on each side (top right), two rows on each side in a square configuration (bottom left) and three rows on each side in a honeycomb configuration (bottom right).

The light intensity profile for all possible configurations amounting to a total number of ~124,000 were obtained. After finding intensity profiles for all configurations, we assessed the performance of each configuration to find the best results. To do this we used two criteria, first, the total light energy inside the fontanelle area, and second, how close this profile is to a uniform distribution. We defined an array,  $M$  as below,

$$M = \frac{E_{fontanelle}}{E_0} \times \frac{E_{mean}}{E_{max}} = \frac{1}{N_{pixel} E_0} \frac{E_{fontanelle}^2}{E_{max}} \quad (8)$$

where  $E_{fontanelle}$  is the total energy deposited inside the fontanelle area,  $E_0$  is the total output light energy from the probe in a single pulse,  $E_{mean}$  is the mean energy in the fontanelle area,  $E_{max}$  is the maximum value of deposited energy and  $N_{pixel}=201 \times 201=40,401$  is the number of pixels inside the fontanelle area. The deposited energy,  $E = I \times da$  where  $I$  is the intensity and  $da$  is the area of each pixel. The first term,  $E_{fontanelle}/E_0$ , shows the fraction of light that is inside the fontanelle area. The greater the amount of light that is outside this area – which is wasted - the smaller this quantity. The second term is the mean energy normalized by the maximum energy inside the fontanelle area. This gives a measure of how evenly the light is distributed on the fontanelle. Since the area is constant, the closer the light is to a uniform distribution, the smaller the difference is between maximum and mean energy and thus this quantity will be closer to 1. In the case where all the light is incident on a single pixel, this term becomes  $E_{fontanelle}/N_{pixel}$ .

After choosing the optimum configuration from the previous simulation study, we used Monte Carlo simulations to find the light fluence distribution inside the brain tissue using MCX software [56]. We designed two three-layer slab models. 1) scalp with thickness of 2mm, skull with 4mm thickness, and 2cm thick layer of brain. 2) We used the same geometry as before except replacing a  $2 \times 2 \text{ cm}^2$  region of skull with scalp to act as the fontanelle opening. We illuminated both tissues on the surface with the same probe configuration we found above. The wavelength of the laser pulse was  $\lambda=570\text{nm}$ . Optical properties of different layers has been as used as follows: scalp ( $\mu_a=0.56 \text{ cm}^{-1}$ ,  $\mu_s=250 \text{ cm}^{-1}$  and  $g=0.9$  [147] and skull ( $\mu_a=0.92 \text{ cm}^{-1}$ ,  $\mu_s=358 \text{ cm}^{-1}$  and  $g=0.92$ ) [148].

This was to show the difference in penetration of light through fontanelle compared to through skull.

We also simulated thermal effects on scalp with varying laser specifications to determine safety. We simulated illuminating the tissue for 200s and observed the temperature change. Different pulse energies with 10, 20, 30, 40, 50 and 60mJ with repetition rates of 5, 10, 20 and 40Hz are used in this study. A thin layer of water is considered in contact with tissue surface which held constant at room temperature (20°C). A 5×18 array of sensors are positioned inside the tissue. Each row consists of five sensors with 5mm separation. Rows are 1mm apart from the surface of the tissue up to 18mm inside the tissue. The configuration of sensor array is illustrated with black dots in Figure 29D(ii). k-wave software package [102] was used for simulations. The tissue damage depends on the temperature of the tissue and the duration it remains within that temperature. Different heating conditions result in different temperature-time histories. The cumulative equivalent minutes at 43°C (CEM43°C) model [149] calculates a single number representing a “thermal iso-effect dose” for each temperature-time history providing a mean to compare them. The thermal parameters for brain, skull, scalp are as follow respectively; 1) density = 1.081, 1.807 and 1.084 gr/cm<sup>3</sup> [150], 2) specific heat capacity = 3.68, 1.3 and 3.39 J/Kg.K [151], 3) thermal conductivity = 0.53, 0.5 and 0.3 W/mK, 4) volumetric blood perfusion = 0.009, 0.0025 and 0.0035 s<sup>-1</sup> [152].

#### **4.2.3 Blood fluence decay curve quantification**

To understand the effect on blood signal at different depths and concentrations in tissue-like media, we constructed our phantom from an open-top, cubic, plastic box in which we drilled two opposing holes to secure a thin capillary (3/32” inner diameter and

1/32" wall thickness). We utilized an automatic syringe pump (Razel Scientific Instruments) with a syringe volume of 150mL to pump heparinized sheep blood of varying concentrations (50%, 25%, 12.5%, 6.25%, 3.125%) diluted with saline at a flow speed of 100mL/hour (See Figure 27). Flowing allowed the blood and saline to maintain homogeneity throughout the experiment. 100%, 50%, and 25% intralipid (Sigma-Aldrich, USA) diluted with deionized water and mixed with 0.1% India Ink (Speedball, United Kingdom) to account for the optical properties of the brain tissue reported in the literature [153-155] (reduced scattering coefficients of 25, 12, and 9 ( $\text{cm}^{-1}$ ) and the absorption coefficient of 1 ( $\text{cm}^{-1}$ )). The optical properties of the intralipid solutions were measured using the method we detailed in [156].

The TFMPI probe was secured to a large translation stage that did not allow movement of the probe throughout the experiments except along the z-axis. Seen in Figure 27. Surrounding optical table components were fixed to allow the phantom box to be removed and re-secured with minimal movement below the probe while changing the milk concentration in the surrounding media. A translation stage (Holmarc, India) was utilized to adjust the distance (1cm to 5cm) of the probe from the blood capillary. In all experiments, the center of the capillary was used for measuring the distance to the probe. In order to keep the experimental parameters consistent, a fixed Verasonics Vantage 128 TGC (Time-gain compensation) profile was used for all phantom data acquisition. For each combination of different depths, intralipid, and blood concentrations, 1000 frames of photoacoustic signal were acquired. Simultaneously, the average energy over these 1000 frames was measured using an energy meter (Gentec, USA). For quantifying the PA signal, the data collected by the three middle elements

(63<sup>rd</sup>, 64<sup>th</sup> and 65<sup>th</sup> elements) of the TFMPI probe were averaged over the 1000 frames and normalized by the average energy. Due to the fixed absorption, the normalized photoacoustic signals at each depth is proportional to the fluence at that depth. Cubic spline interpolations were performed on each set of data to estimate a fluence decay function with depth for each scattering media. A fluence decay estimation based on absorption coefficient and, depth of the absorber and the scattering properties of the surrounding media is created using a cubic spline algorithm.

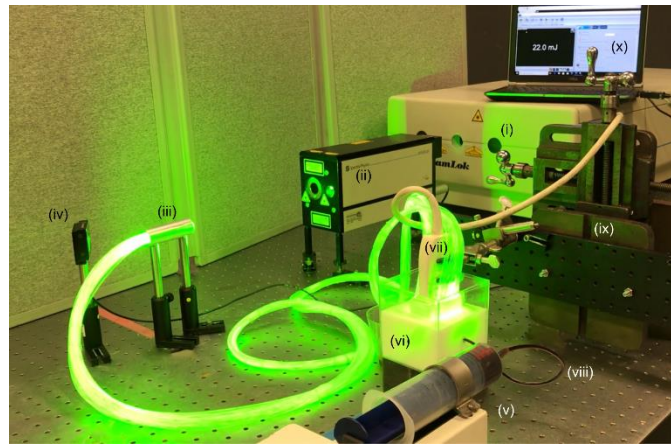


**Figure 27. Blood fluence decay experimental setup.** Experimental setup of in-vitro probe characterization. (i) Laser head, (ii) optical parametric oscillator, (iii) fiber bundle, (iv) energy meter (Gentec, USA), (v) automatic syringe pump, (vi) intralipid solution, (vii) TFMPI probe, (viii) capillary representing vessel, (ix) translation stage, (x) laptop for energy measurement and wavelength switching.

#### 4.2.4 Probe resolution analysis

To determine the photoacoustic resolution of the prototype TFMPI probe, we constructed a phantom in which a thin hair was secured to the inside of the same open-top, cubic, plastic box, and imaged in ultrasound and photoacoustic modality. The hair was measured with light microscopy (Olympus BX-41) to be 75 $\mu$ m in diameter seen in Figure 28.

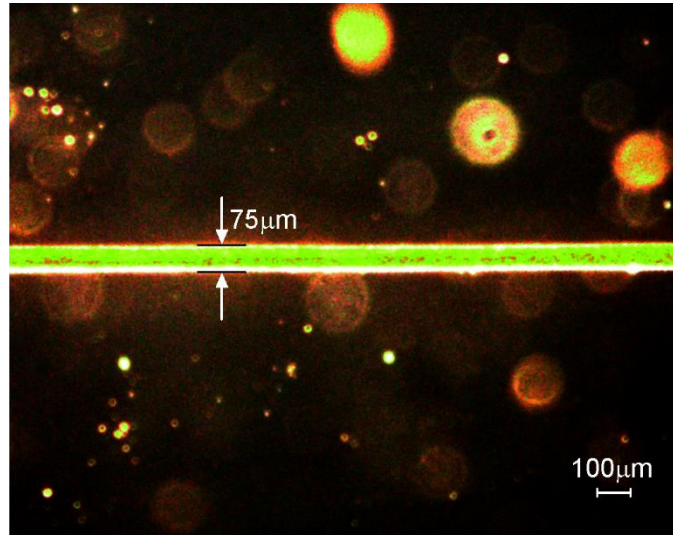


**Figure 28. Light microscopy image of human hair for resolution study.** Light microscopy image of 75μm human hair used for photoacoustic resolution study. Olympus BX41 microscope used with Infinity 3 camera for capture.

#### 4.2.5 Sensitivity analysis

After fluence decay and resolution characterization of our TFMPI probe, we quantified the sensitivity of the probe to blood signal compared to traditional ultrasound. Gelatin phantoms were mixed and left to stiffen in small cups with 0.5cm aluminum rods in their top to form a small opening. Heparinized sheep blood (Quad Five, USA), at different concentrations, i.e., 0.2%, 0.4%, 0.8%, 1.6%, 3.13%, 6.3%, 12.5%, and 25%, to represent hemorrhage into ventricular space, as well as different concentrations of the blood mixed with blended perfused sheep brain tissue (compact blender Bosch Inc., USA)), i.e., 0.2%, 0.25%, 0.3%, 0.4%, 0.5%, 0.6%, 0.8%, 1%, 1.2%, 1.6%, 3.13%, 6.3%, 12.5% and 25%, intraparenchymal hemorrhage, were injected into the openings of the gelatin phantoms and imaged with TFMPI.

#### 4.2.6 Oxygen saturation measurement

One of the applications of TFMPI in neonatology is tissue oxygen saturation ( $SO_2$ ) measurement.  $SO_2$  maps provide information about tissue hypoxia. To calculate

the  $SO_2$ , the photoacoustic signal from the blood sample is acquired at 800nm and 750nm to determine the ratio of oxy- and deoxy-hemoglobin from their differing absorption spectra. Using the spectroscopy formula, equation (9) [157], then a value for  $SO_2$  is obtained.

$$sO_2 = -\frac{\epsilon_{Hb}^{750}}{\Delta\epsilon_{Hb}^{750}} + \frac{\epsilon_{Hb}^{800}}{\Delta\epsilon_{Hb}^{750}} \frac{\mu_a^{750}}{\mu_a^{800}} \quad (9)$$

To confirm  $SO_2$  measurement ability of TFMPI, We imaged un-diluted heparinized sheep blood in a capillary system with varying  $SO_2$  and compared the extracted  $SO_2$  from the PA signal amplitude to measurements from a blood-gas analyzer (BGA) (Opti CCA-TS, Optimedical, USA). We varied the blood oxygen saturation from 64% to 95% to replicate the hypoxia, normal, and hyperoxia scenario. Fresh blood was measured by the BGA to be 95% and few days old blood was measured to be 60% saturated. We varied the blood oxygen saturation by mixing the two blood together without exposing the samples to the atmospheric air. Initially, the 95% saturated blood was imaged, followed by mixing of 15 mL of higher saturation with 5 mL of the 60% saturated. The resulting mixture was continually mixed with 5 mL of 60% saturated blood until we reached the lowest oxygen saturation (~64%). The  $SO_2$  of the blood mixture was stable during the imaging and it was confirmed by measuring the oxygenation level using the BGA before and after the imaging took place. The TFMPI probe was held using the two-way translation stage. Each oxygen saturation blood sample was imaged at depths of 0.5 cm to 2.5 cm in 0.5 cm increments for 100 measurements.



#### **4.2.7 *Ex-vivo* sheep brain hemorrhage imaging study**

In *ex-vivo* study, we have tested the TFMPI probe's capability in detecting hemorrhages in adult sheep brain. The rationale for choosing a sheep model are (1) the brain size is closest in size to a human neonatal brain (especially preterm neonatal brain) and (2) skull anatomy is amenable to relatively easy surgical access [158-160]. Adult animals do not have a cranial fontanelle which is required for this imaging technique to work (requiring an "optical window" for an efficient light illumination and an "acoustic window" for efficient acoustic detection), and will require creation of a "closed" craniotomy in which the site will be covered by the scalp skin. Therefore, conducting *ex-vivo* studies on a sheep head with a surgically induced cranial window which represents fontanelle, will produce the most relevant results. Several freshly decapitated sheep heads were purchased from local slaughter house. Initially, excess fatty tissues and flesh was removed from the top of the head using scalpel which is followed by sterilizing the fontanelle area. Next, a 6 cm diameter hole was drilled into the skull with a hole saw. The TFMPI probe was held in place by a triaxial stage with clamp. The air gap between the transducer surface and the brain surface was filled with ultrasound gel (Aquasonic Inc., USA) for acoustic coupling.

Grade 1-4 intracranial intraventricular hemorrhages were created in the sheep brain. This *ex-vivo* hemorrhage model was created in two phases. Firstly, to realize the hemorrhage, the sheep head was dissected along the coronal plane. To mimic grade 1 and 2 hemorrhage, fresh sheep blood has been mixed with 8% gelatin and the 0.5~1ml solution is poured at base of the lateral ventricles. For Grade 3 and 4 hemorrhage, the cavity of lateral ventricles are filled with the injected blood and gelatin solution. Also, to

show the extension into the parenchymal region different size of (2-5mm) biopsy punches were used to create holes within the white matter near the lateral ventricles and filled with gelatin mixed blood solution. The dissected two pieces are carefully attached using skull adhesive. In the second phase, the fontanelle area has been realized. Since, we have used a decapitated sheep head, a 2mm diameter hollow tube is realized using 8% gelatin and filled with deoxygenated blood to mimic the superior sagittal sinus (SSS). Next, the dura is placed on top of the SSS layer. The dura and the SSS phantom was laid on top of the brain through the cranial window. A fibrous solution of 2% fiber and 8% gelatin dissolved in water is poured on top of the dura to hold it along with the SSS phantom and fill up any residual airgap within the cranial case. The overall thickness of the fibrous tissue mimicking phantom on top of the dura was 0.5cm.

Intraparenchymal blood/gelatin mixed injections were also evaluated at various depths in the sheep brain. Due to the presence of high intensity background PA signal from existing absorbing chromophores, the cross-sectional PA images were acquired before and after injecting sheep blood. The images acquired before injection were used as control signal and subtracted from the corresponding images after injection. One sheep head with injections was used to generate a PA compensation curve, which was then used on a subsequent sheep head.

#### **4.2.8 Vessel rupture and edema detection using Evans Blue contrast agent**

When a vessel ruptures in the brain and bleeds, this not only creates a blood clot but also generates edema. US imaging is insensitive [161] to differentiating edema from blood [162, 163]. Due to the lack of strong absorbing compartments in edematous regions, there is not a strong photoacoustic signal generated in these regions either.

Evan's Blue is an FDA-approved contrast agent that binds to plasma proteins and has been used in neonatology for the past several years [164]. It is frequently stated in blood-brain barrier studies that Evan's Blue binds rapidly, with good affinity to albumin [165, 166], associated with regions of edema. A key criterion for Evan's Blue dye is that, with a much smaller concentration it remains in the circulation at a constant level for 40 minutes [166]. Using this contrast agent, quantitative assessments of damage to the blood-brain barrier can be realized. The contrast agent also lights up the edematous regions. We investigated the use of Evan's Blue as a possible exogenous contrast agent for TFMPI to localize edematous regions as well as vascular rupture.

An agar-gelatin based bilayer phantom was made to model the rupture in a vessel was made. Initially, a 2cm thick 3% agar solution in a plastic, open-top box was created with two cylindrical inclusions. A larger diameter inclusion (4 mm) represented the main vessel and the smaller (2 mm) represented where the rupture occurred. A horizontally placed aluminum rod created the larger inclusion and a vertically placed hex key created the smaller, while the agar of the phantom was setting. The aluminum rod was placed in such a way that it barely touched the top layer of agar solution. Mold release (Smooth-on Inc., USA) was sprayed on the aluminum rod and hex key for easy release from agar. Once the agar solution was set, 8% gelatin solution was created to surround the main vessel and left at room temperature to be cured. After both the layers are set, the aluminum rod was carefully taken out to avoid any crack in the phantom layers and the large hollow space was filled with defibrinated sheep blood. Next, a slight vacuum was applied to exterior of the box to pull the blood into the smaller inclusion. The box was set upside down overnight to let the blood diffuse through the agar

phantom layer. The diffused blood from the smaller hollow space mimics the hemorrhage model as shown in Figure 37B.

Evan's Blue absorption is strongest at 690nm (Figure 37D) where oxygenated hemoglobin (HbO) and deoxy-hemoglobin (HbR) have much weaker absorption. Ultrasound gel is used to couple the probe to the phantom. After the hemorrhage model was realized, heparinized sheep blood was injected into the main vessel of the phantom and visualized at 750nm. The laser illumination wavelength was then changed to 690nm to reduce blood signal and increase Evan's Blue signal before a 1mg/mL solution of Evan's blue was injected.

In another experiment, the situation with an edema area was realized in a similar phantom as mentioned above with two smaller inclusions. In this experiment, 1mL egg white, which contains albumin, was implanted through one smaller inclusion to diffuse near the main vessel to create edema and other inclusion was used to create the hemorrhage model. 1mg/ml Evans Blue in saline solution was injected through the main vessel and using external vacuum we let the blood mixed with Evan's blue get into both inclusions. We imaged both the inclusion locations every 30 minutes for 3 hours.

## **4.3 Results**

### **4.3.1 Light delivery optimization through simulation**

Transcranial ultrasound imaging is challenging due to the strong distorting effects of the skull, i.e., signal attenuation, time-domain signal shift, broadening and longitudinal to shear wave mode conversion [167, 168]. In addition to ultrasound distortion, light attenuation is also significant when it travels through the skull due to the high scattering coefficient of the skull tissue compared to soft tissue. Photoacoustic imaging through

the fontanelle makes the detection of ultrasound waves possible without experiencing high acoustic and optical scattering caused by the skull. Since the probe should be placed on the fontanelle, the light source should also be expected to illuminate the area of the fontanelle. With that in mind, the main idea is to deliver light confined to the fontanelle area with an intensity distribution as close as possible to the uniform distribution and without intensity exceeding the allowable threshold at any point. Diameter of the optical fibers,  $D$ , numerical aperture,  $NA$ , bending angle,  $\theta$ , vertical distance of fiber with the tissue surface,  $H$ , and the arrangement of the optical fibers are the main parameters to optimize. Monte Carlo simulations, MCX software [47], was used to study the effect of these parameters on the intensity profile of the probe generated on the tissue surface; the results are shown in Figure 29A(i-v). The intensity profile of a single fiber with diameter  $D = 0.5$  mm,  $NA = 0.1$ , bending angle  $\theta = 0^\circ$  (perpendicular) and a distance from the surface  $H = 5$  mm is shown in Figure 29A(i). In Figure 29A(ii-v) only one of the above parameters is changed each time, (ii)  $\theta = 60^\circ$ , (iii)  $D = 2.5$ mm, (iv)  $NA = 0.4$  and (v)  $H = 10$  mm, while the other parameters kept constant. In addition to the number of rows of fibers, we introduce a parameter  $L$ , the distance between the first row and transducer axis, making the width of the probe ranging from 10 to 20mm. Note that, the width of the probe did not exceed 4 cm in any configuration. Figure 29B(i-iv) demonstrate examples of light intensity profiles. The green box shows the fontanelle area while the center green line indicates the axis of the transducer. Optimization was performed by maximizing the value of  $M$ , which is a value to represent both total light energy inside the fontanelle area, and, how close this profile is to a uniform distribution. The higher  $M$ , the more uniform intensity profile is. These results

are shown in the scatter plot of Figure 29C(i). Each configuration ID number refers to a specific probe configuration with known parameter sets. The ID with the highest  $M=0.7696$  refers to the probe configuration consisting of 4 rows (honeycomb) at each side of the transducer (total width = 10mm) with fibers with  $D=1.5\text{ mm}$ ,  $NA=0.5$ ,  $\theta=40^\circ$ ,  $H=5\text{ mm}$  and  $L=5\text{mm}$  (see Figure 29C(ii)). Although this optimal configuration was computed, we continued with the following experiments with the previously identified 2 illumination configurations defined in section 4.2.1.

To see the effect of skull in reducing the optical energy deposition, we considered two geometries in MCX simulations. Initially, a 3-layer slab model with first layer as scalp with thickness of 2 mm and second layer as skull with 4 mm thickness and a 2 cm thick layer as brain (see Figure 29D(i)). In the second case, we used the same geometry as before except replacing a  $2\times 2\text{ cm}$  region of skull with scalp to act as fontanelle opening (see Figure 29D(ii)). We illuminate both tissues on the surface with the same optimized probe configuration described above. Note that, the most efficient laser light wavelength was found to be 570nm. This was based on both a deeper penetration depth and a larger absorption peak for blood (total hemoglobin). The lower attenuation of light when through fontanelle as compared to that through the skull shows increased fluence of about 2.4 times (see Figure 29D(iii and iv)).

The TFMPI probe was also characterized and optimized from thermal point of view. For thermal calculations we used readings from a sensor array illustrated with black dots in Figure 29D(ii). Figure 29E(i) shows the highest sensor reading after 60s of illumination; 60s is considered a duration of a typical imaging session. It is evident that with higher repetition rates the temperature increases very fast even with lower pulse

energies since the tissue has less time to cool down; for instance, with 40Hz repetition rate even with 10mJ pulses of 532nm laser light (which is well below ANSI limit [169]) a considerable thermal dose is delivered in 60s. Different combinations of applied laser pulse rate and energy per pulse result in different effective thermal dose. Cumulative equivalent minutes at 43°C model (CEM43°C) [149] (the temperature at which the tissue is damaged) is used to calculate a single number representing a “thermal iso-effect dose” for each temperature profile providing a mean to compare them. CEM43°C model gives the equivalent exposure time with the same thermal effect as if the temperature was constant at 43°C. The dashed line in Figure 29E(i), corresponds to 1 min of equivalent thermal dose at 43°C. Any configuration that is below the 1 min threshold can be considered safe [170]. Figure 29E(ii) shows the highest temperature reached by the tissue after 200s illumination calculated based on CEM43°C model. Configurations resulting in lower temperatures closer to normal body temperature are much more attractive.

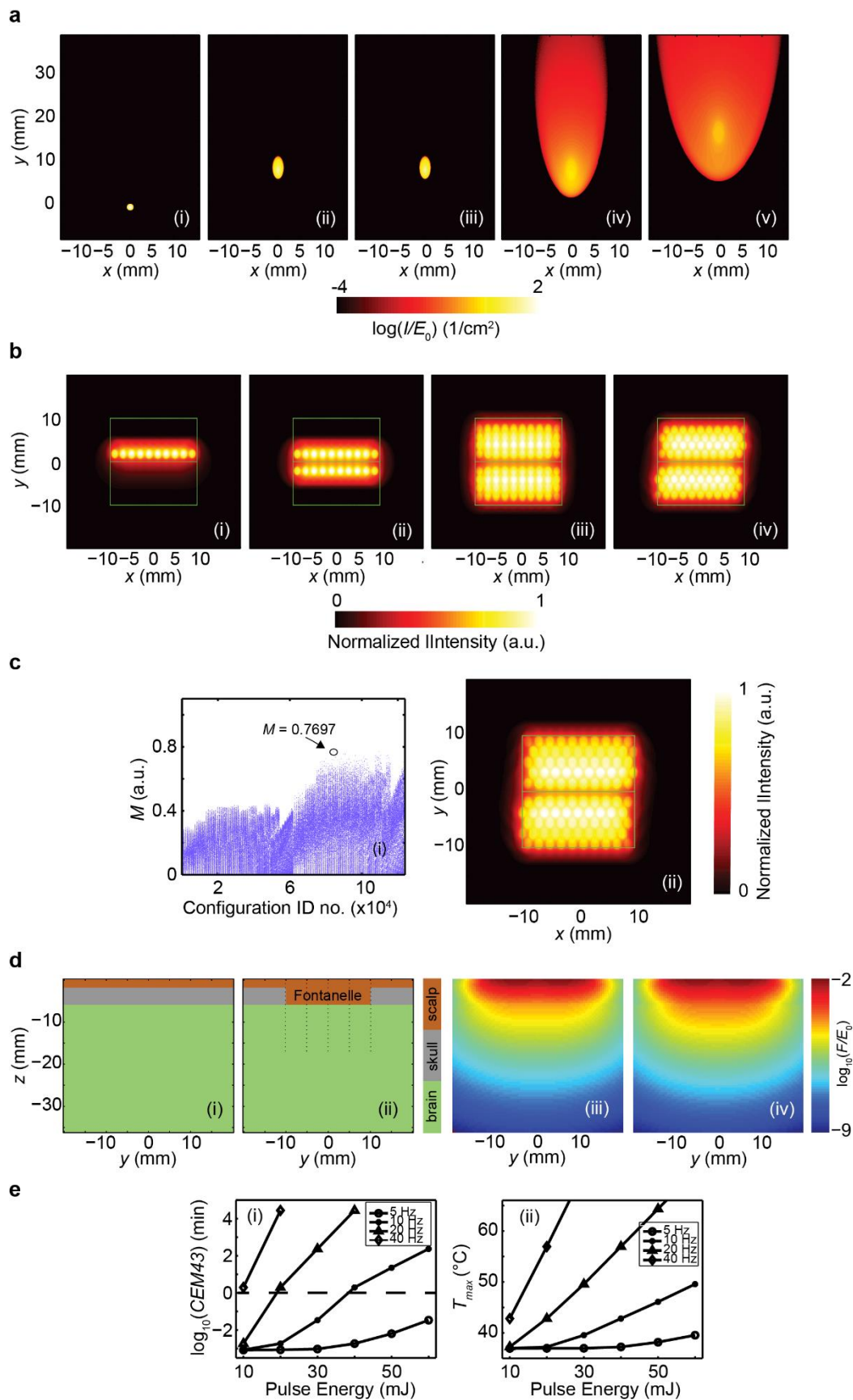




**Figure 29. TFMPI Simulation Study.** (A) Effects of changing the parameters of optical fiber on light intensity profile. (i) Intensity profile of a single fiber with diameter  $D = 0.5$  mm,  $NA = 0.1$ , bending angle  $\theta = 0^\circ$  (perpendicular) and distance from the surface  $H = 5$  mm. (ii) changing bending angle to  $\theta = 60^\circ$ , (iii) then core diameter changes to  $D = 2.5$  mm, (iv) numerical aperture changes to  $NA = 0.4$  and (v) distance from surface changes to  $H = 10$  mm. (B) Light intensity profiles for different probe configurations, (i) one row at one side, (ii) one row at each side, (iii) five rows at each side in a square configuration and (iv) in a honeycomb configuration. Intensity of each configuration is normalized by its own peak intensity meaning that these figures show the intensity if the total output light energy for different configurations is maintained in such a way that all peak intensities will be the same. This is important because the peak intensity is the limiting factor. Green boxes show the fontanelle area and the middle green line is the ultrasound transducer axis. (C) Calculated metric  $M$  for all ~124,000 possible probe configurations considered in this study.  $M$  is a combined measure of fraction of output light which illuminates fontanelle area and uniform distribution. The greater the value of the  $M$ , the better the performance of that configuration. Configuration ID number refers to a configuration with known parameter set. Largest value found to be  $M=0.7697$  and that configuration is shown at right. (D) Fluence inside the tissue and significance of fontanelle. (i) the geometry used for Monte Carlo light simulations with three layers of scalp (2 mm), skull (4 mm) and brain (20 mm), (ii) same geometry with only an  $20 \times 20$  mm area of the skull replaced by scalp to act as fontanelle. (iii) fluence inside the tissue for illumination through skull and (iv) for transFontanelle illumination. (E) Thermal study, (i) CEM43 model has been used to find a safe time limit (1min). For different configuration of pulse repetition rate and energy, operating points below the dashed line can be considered as a safe choice, (ii) temperature for different configurations after illuminating a tissue for 200s.

#### 4.3.2 Blood fluence decay curve quantification

When imaging hemorrhage it is important to understand the dynamic assortment of parameters contributing to the PA signal received from the hemorrhage. To better understand this interplay of parameters, we imaged blood of varying concentration at different imaging depths within different scattering media. Figure 30A demonstrates the schematic for the experiment in which the blood solution is continuously pumped through a capillary within a plastic box holding the intralipid/india ink solution. Figure 30(B-D) demonstrates the normalized blood signal curves received. These curves can be used for compensation of a known concentration of blood that is being imaged at different depths.

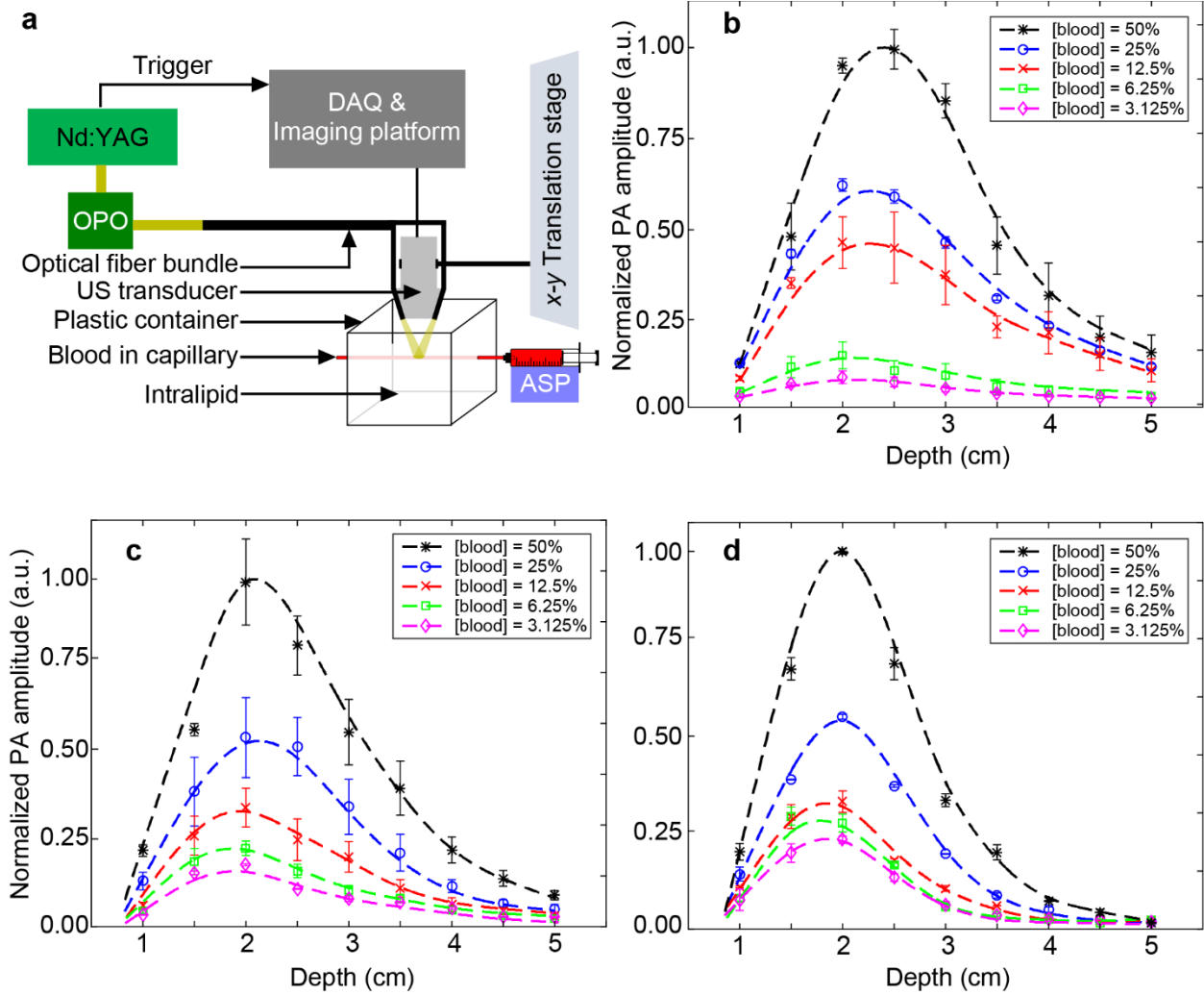


**Figure 30. Fluence decay characterization of the TMPI probe.** (A) Schematic of the intralipid phantom study, OPO: optical parametric oscillator, ASP: automatic syringe pump. Continuously flowing heparinized sheep blood diluted with saline at different concentration (50%, 25%, 12.5%, 6.25%, and 3.125%) was imaged at different concentration of intralipid surrounding solution (B) 25%, (C) 50%, and (D) 100%.

#### 4.3.3 Probe resolution analysis

We constructed a phantom in which a thin human hair (smaller than the resolution of the ultrasound transducer) was secured to the inside of an open-top, cubic, plastic box filled with deionized water. The hair was measured with light microscopy (Olympus BX-41) to be 75 $\mu$ m in diameter. The image of the hair provided a point spread function when taking a 1-dimensional intensity profile through the object in the image.

The experimental resolution was determined by generating 1-D intensity through the hair, vertically for axial resolution and horizontally for lateral resolution. Fitting a Gaussian function to the intensity discrete data and calculating the full width half maximum (FWHM) of the fit yielded the axial and lateral resolutions at different depths (0.5 to 5 cm with the steps 0.5 cm). The raw Gaussian fits can be seen in Figure 31.

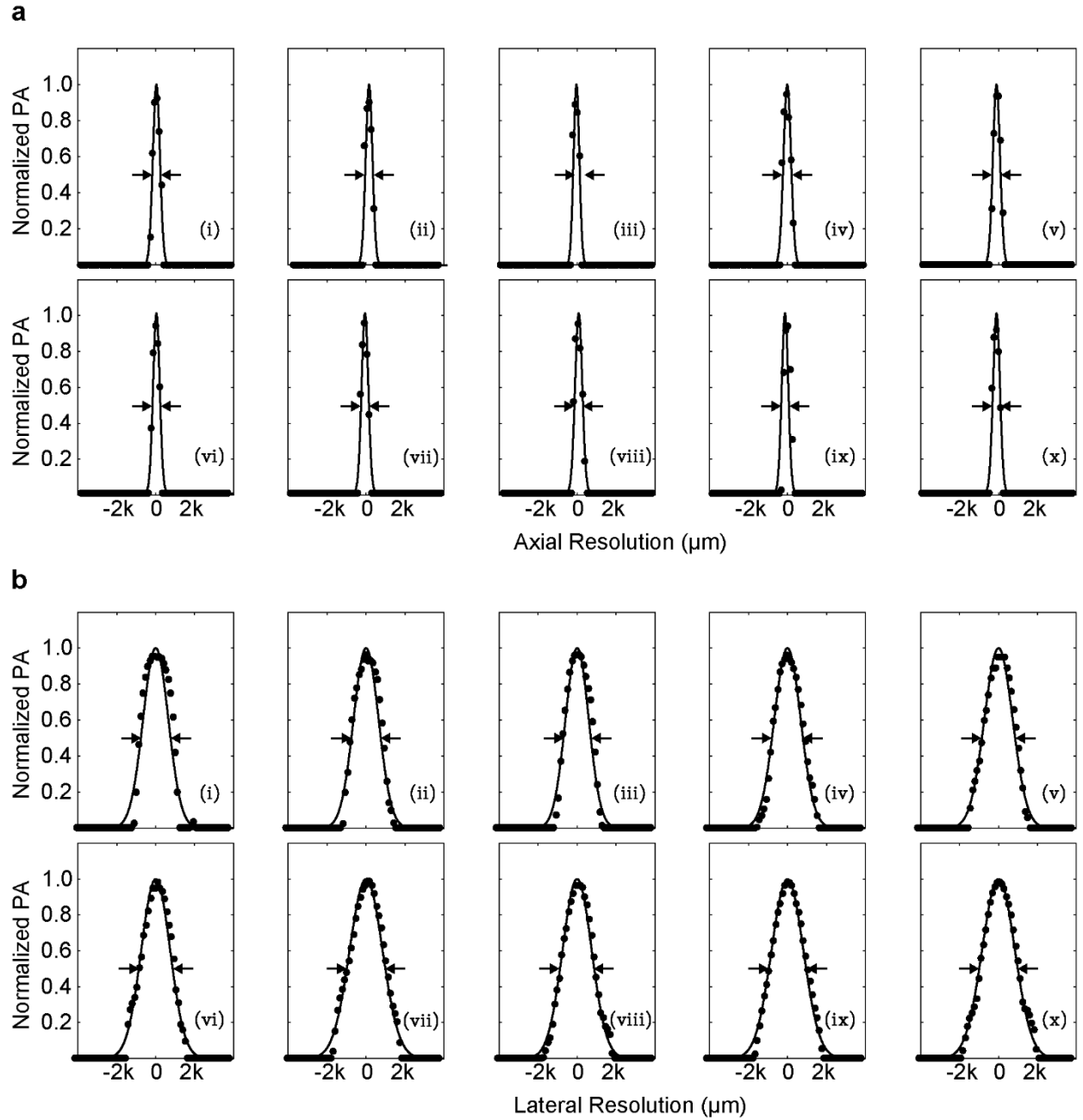


**Figure 31. Point spread function characterization for axial and lateral resolution.** (A) 1-dimensional (1-D) pixel intensity curves across 75 $\mu$ m human hair fit with Gaussian function at depths in cm (0.5, 1.0, 1.5, 2.0, 2.5, 3.0, 3.5, 4.0, 4.5, 5.0) to approximate axial resolution. (B) 1-D pixel intensity curves across 75 $\mu$ m human hair fit with Gaussian function at same depths as (a) to approximate lateral resolution.

Figure 32 quantifies the FWHMs of the Gaussian fits in Figure 31. From Figure 32, it can be seen that the linear regression of the axial resolution is a horizontal line, implying that it does not change with depth, while the lateral resolution grows with depth. The analysis suggested that the TFMPI probe has an axial resolution of 416 $\mu$ m and an average lateral resolution of 1.72mm.

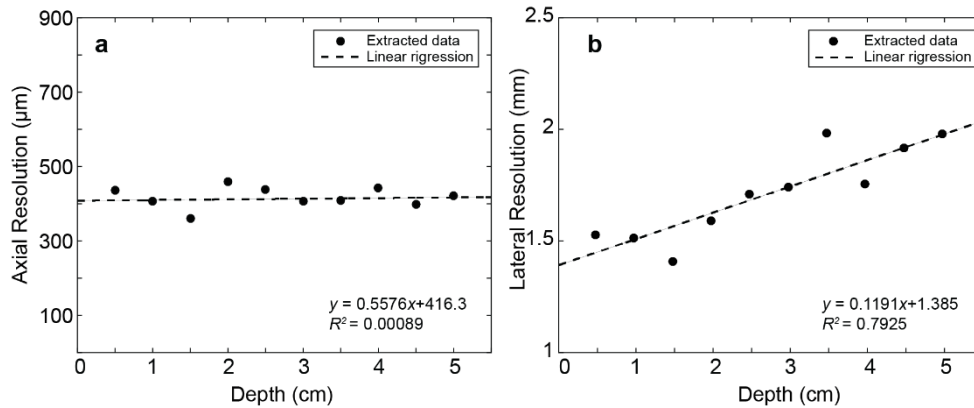


**Figure 32. TFMPI resolution summary.** The probe resolution (A) axial, (B) lateral was experimentally measured by imaging ~75 $\mu$ m diameter human hair immersed in deionized water at different depths in cm (0.5, 1, 1.5, 2, 2.5, 3, 3.5, 4, 4.5, 5). Point spread function of hair was characterized by Gaussian fit. Full width half max (FWHM) of the respective Gaussian fit was calculated to approximate the resolution.

#### 4.3.4 Sensitivity analysis

This study is designed to show the advantage of the photoacoustic method over conventional ultrasound technology to detect the severity of hemorrhage into ventricular space or resulting from an intraparenchymal hemorrhage, by utilizing the innate higher sensitivity of PA to identify wide-ranging blood concentrations. In Figure 33, the US and PA values were normalized to their minimum and maximum values in both graphs. In these graphs, it is evident that the PA signal exhibits a steep pattern of linear growth

with increasing blood concentration, even from very low concentration samples whereas, the US signal is incapable of providing a meaningful pattern at low concentrations of blood. In higher concentrations, the US signal was able to follow the same linear growth as PA signal did.

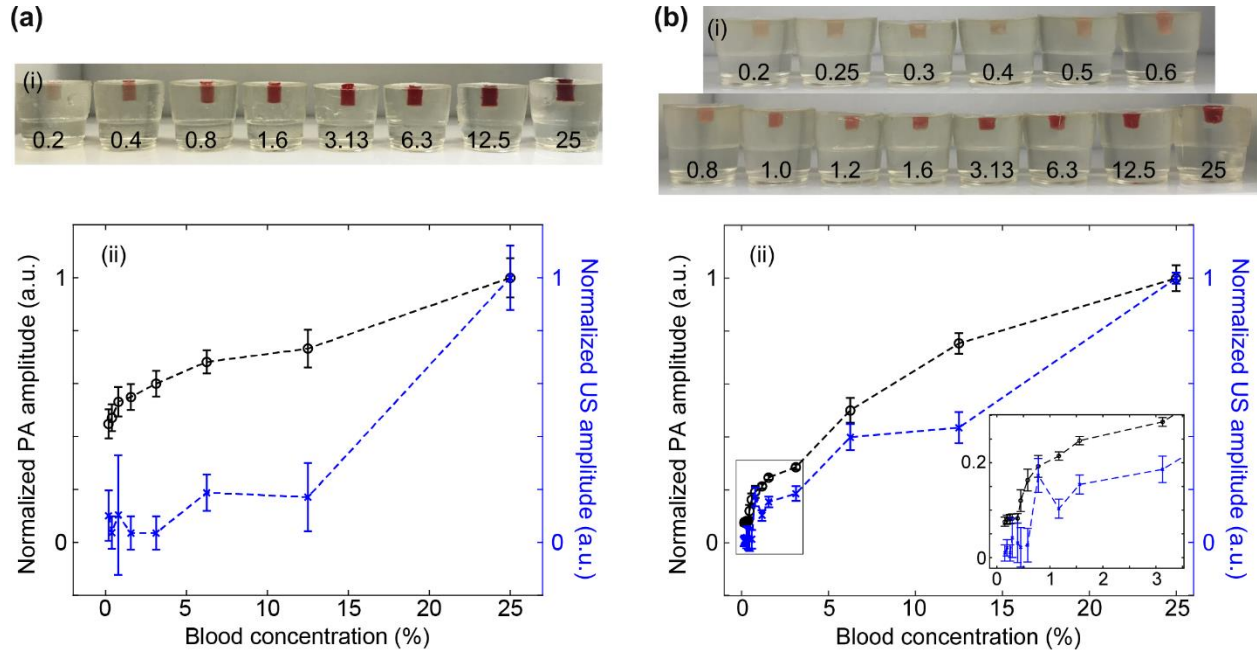


**Figure 33. TFMPI and US blood sensitivity.** (A) (i) Samples of heparinized sheep blood diluted with saline in gelatin phantom, (ii) PA and US signal amplitudes of samples in (i), (B) (i) Samples of heparinized sheep blood mixed with brain tissue in gelatin phantom, and (ii) PA and US signal amplitudes of samples in (i). Data points at lower concentrations (0.2%-3.13%) are magnified in the inset to show the PA signal pattern and US signal fluctuation.

#### 4.3.5 Oxygen saturation measurement

Comparison of the measurements performed by TFMPI and those done by BGA at different depths are provided in Figure 34. Each point in the graph is the average of 100 PA signal acquisitions that were normalized with respect to their corresponding laser optical energy. This summary demonstrates the ability of the TFMPI probe to accurately determine blood oxygenation in a vessel through tissue-like background.

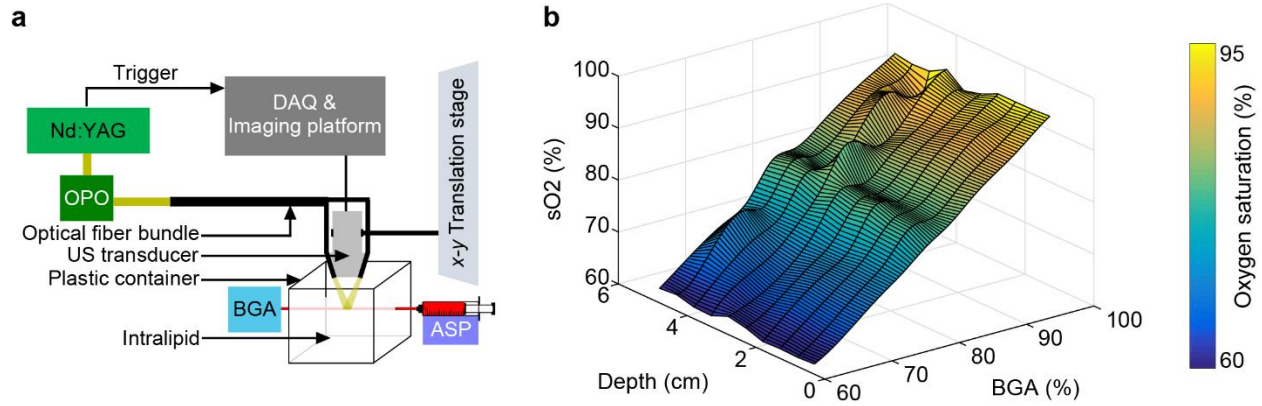


**Figure 34. Oxygenation evaluation summary.** (A) Schematic of the oxygen saturation measurement and validation setup, (B) oxygen saturation of continuously flowing heparinized sheep blood within the range of 60-97% measured by TFMPI at depths 0.5 cm to 5 cm with 0.5 cm increments; compared with and validated by the gold standard blood gas analyzer (BGA) measurement results.

A more detailed set of graphs is seen in Figure 35A that exhibits TFMPI probe accuracy in determining the oxygen saturation at different depths which were summarized into Figure 34B. In Figure 35B, the deviations from the expected values at different depths were plotted. The extracted oxygenation results showed less than 3.2% deviation from the BGA measurements, i.e., gold standard.

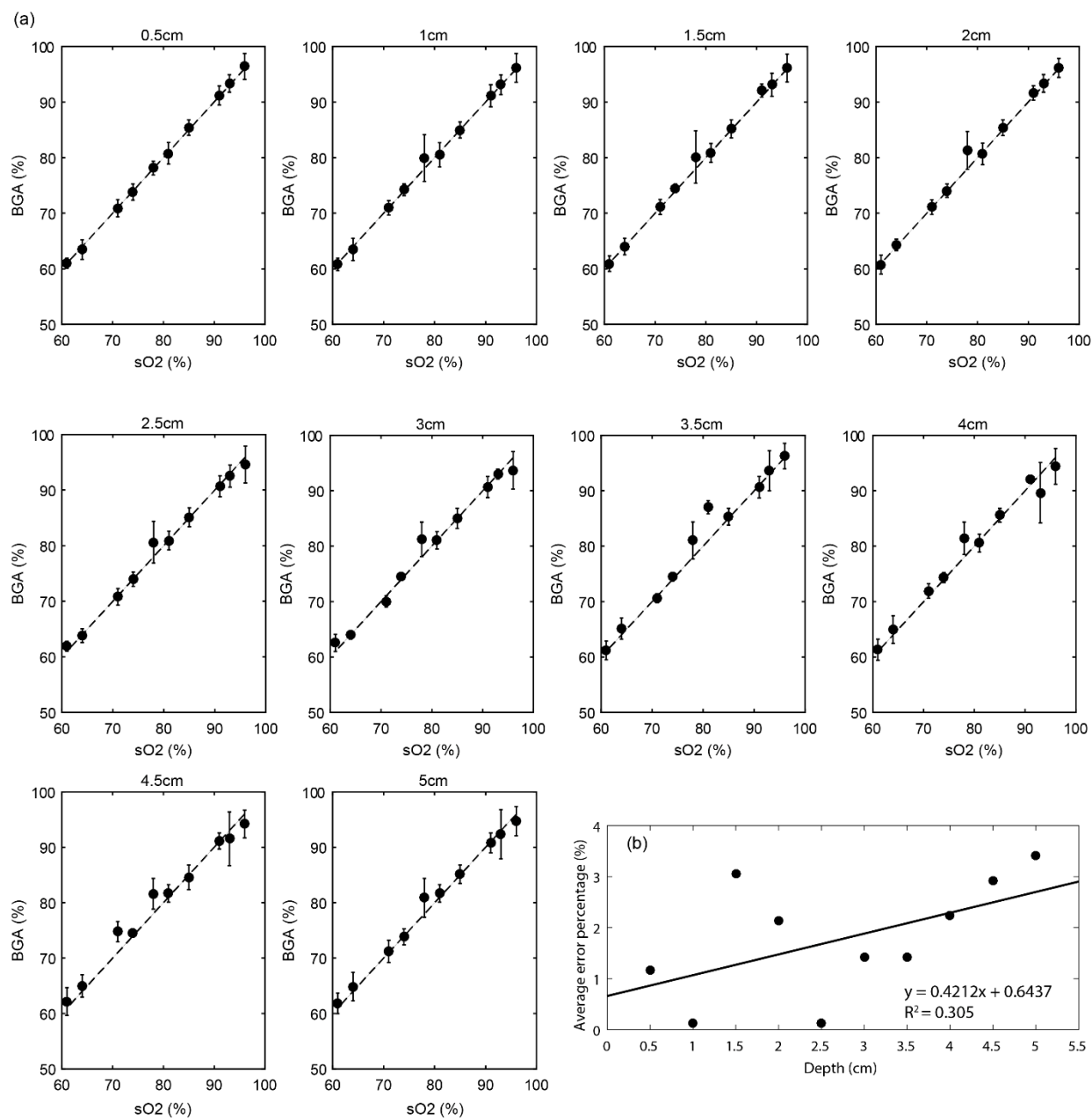


**Figure 35. More detailed oxygenation data.** (A) The oxygenation data collected at different depths, 0.5 cm, 1cm, 1.5cm, 2cm, 2.5cm, 3cm, 3.5cm, 4cm, 4.5cm, and 5cm were compared with and validated by the gold standard blood gas analyzer (BGA) measurement results, (B) average error percentage exhibited a linear increment with increasing depth and a maximum deviation of 3.2% from BGA results was observed at 5cm.

#### 4.3.6 *Ex-vivo* sheep brain hemorrhage imaging study

The size and the intensity of the intraventricular hemorrhages from PA signal was calculated based on the pixel area and intensity respectively using ImageJ software. US data was also collected simultaneously to compare with the PA data and shown in Figure 36B. It is evident that, the PA signal has a linear progression with increasing size of the hemorrhage, whereas the US signal provides lack of pattern at smaller hemorrhage size (<3mm). Five TFMPI images of hemorrhage lesion at different depths were superimposed on the corresponding ultrasound image slices of the sheep brain and are shown in Figure 36C. The data presented in Figure 36D is the absolute PA signal for hemorrhages from multiple depths and was used to generate a compensation curve. Figure 36E, uses the previously generated compensation curve on a new sheep head set of PA signals.. In this case, compensated PA signal exhibits a flat response at different depths and can be retraced to determine the actual depth, whereas, it is difficult to interpret the actual depth of the hemorrhage lesion from the US data due to the intensity fluctuation.



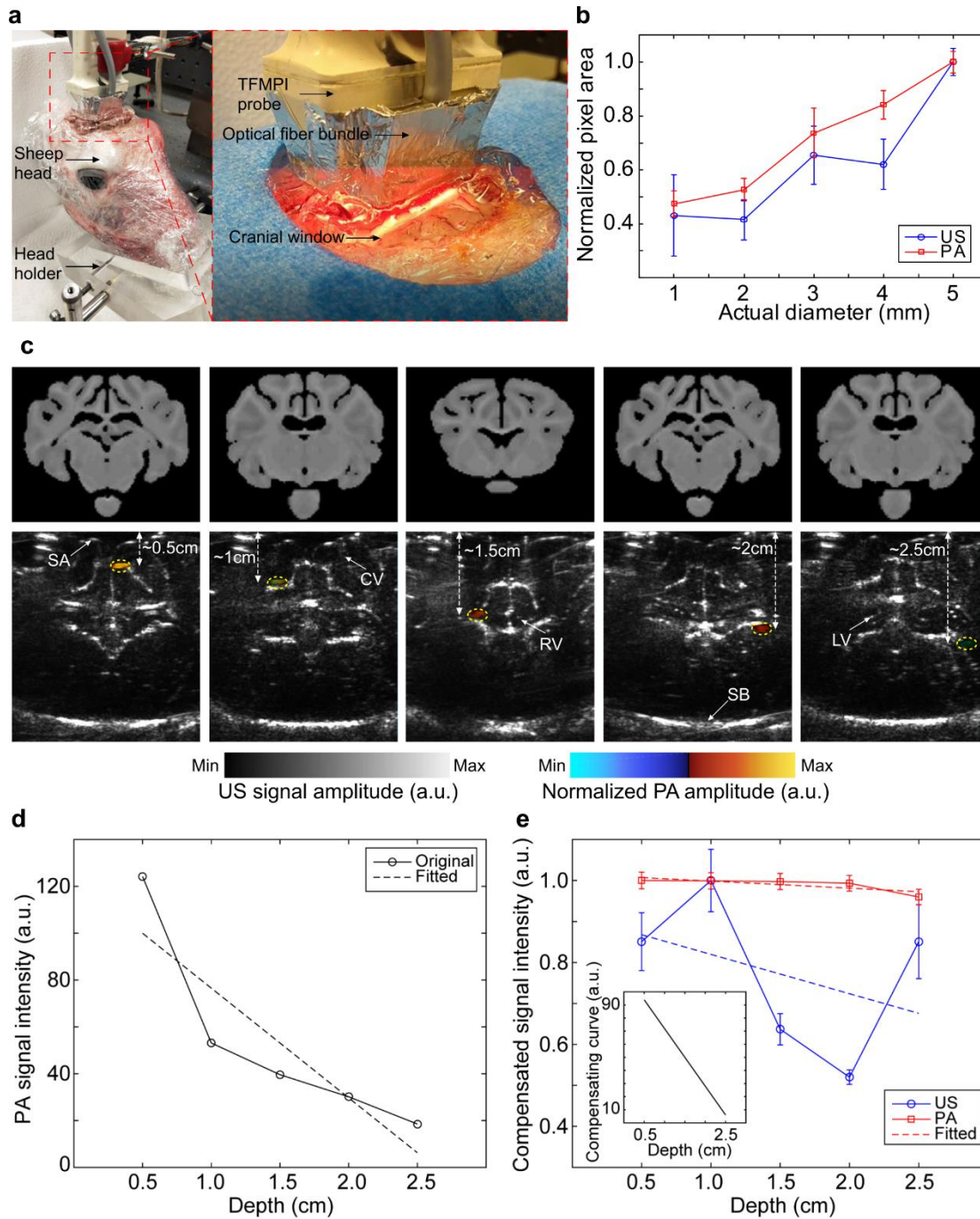


**Figure 36. Ex vivo feasibility study of the TFMPI in detecting pseudo-hemorrhage model.** (A) Experimental setup including sheep head, head holder, TFMPI probe, optical fiber bundle, (B) Normalized pixel area of the various hemorrhage sizes (1, 2, 3, 4, and 5mm diameter) extracted from PA and US images as a function of actual hemorrhage size. (C) PA images of injected hemorrhage at different depths (0.5-2.5cm) overlaid on US images and compared with respective brain slices, (D) Original PA amplitude from the induced hemorrhage at different depths and corresponding fitted curve, (E) Fluence decay compensated PA signal and original US signal along with

respective fitted curve. The compensating curve is shown as inset. SA: subarachnoid, CV: cortical vasculature, RV: right ventricle, LV: left ventricle, SB: skull base.

#### **4.3.7 Vessel rupture and edema detection using Evans Blue contrast agent**

After the hemorrhage model was realized, heparinized sheep blood was injected into the main vessel of the phantom and visualized at 750nm as seen in Figure 37C(i). With hemorrhage model created, it is clear that the signal generated from blood made it difficult to localize the rupture. Changing the wavelength of the incoming light to 690nm (~10 times higher absorption of Evan's Blue as compared to Hb) shows a reduction in blood signal seen in Figure 37C(ii). For the detection of rupture location, we created a 1mg/ml Evan's Blue in saline solution, slowly injected into the main vessel of the gelatin phantom, observed the movement of the dye in the vessel-like tube, and, where it came out of the tube, i.e., the rupture Figure 37C(iii).

The variation in PA signal intensity at both the inclusions are shown in Figure 37E. The dye flowing through the edema got bonded with the albumin molecules and provide higher intensity PA signal over time. Whereas, Evan's blue continued to diffuse through hemorrhage model and hence a decaying pattern of the PA intensity was observed at this location. This experiment establishes the proof of concept that the proposed TFMPI probe is capable of differentiating edema and hemorrhage model by utilizing commonly used exogenous contrast agent.

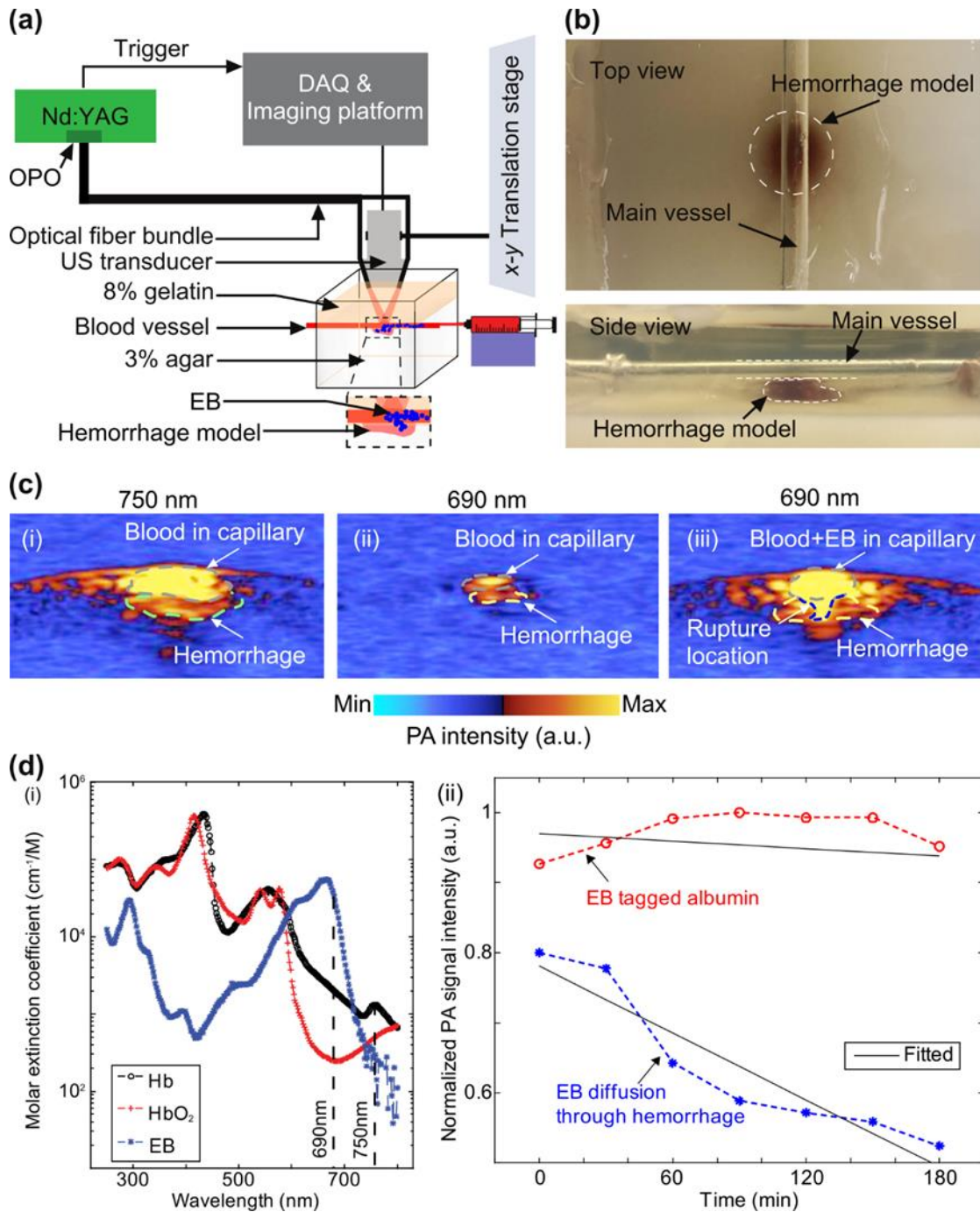


**Figure 37. Evaluation of use of Evan's Blue to identify edema.** (A) Schematic of setup of gelatin-agar phantom with injection of Evans Blue into a cylindrical inclusion, (B) Hemorrhage model created beneath the main vessel by diffusing blood in the agar phantom through smaller inclusion. (C) Photoacoustic live window recorded with screenshots (i) injection of blood in the main vessel and imaged at 750nm, (ii) reduction in blood PA signal when switching to 690nm (higher absorption of Evans Blue), (iii) signal increase in both main vessel and the rupture location shows up with injection of Evans Blue, imaged at 690nm, (D) (i) Evans Blue absorption spectrum showing two

wavelengths and corresponding absorption of Evan's Blue, Hb, and HbO<sub>2</sub>, (ii) Normalized PA signal intensity from Evan's Blue tagged Albumin (red) and Evan's Blue diffusing through hemorrhage location (blue) measured at the edema and hemorrhage model respectively

#### **4.4 Discussion and conclusions**

Preterm neonates (<32 weeks gestational age) and/or with low birth weight (<1500g) are at high risk for intracranial hemorrhage (ICH) with the incidence of 30%-35% [114]; many more sub-clinical cases (that do not manifest by obvious symptoms of neurological deficit) remain undiagnosed due to limitations of current instrumental techniques. Complications include long term structural changes: post-hemorrhagic hydrocephalus, periventricular leukomalacia, gliosis, and other neurological dysfunction [104]. Significance of brain injury is dependent on severity, duration and location of hemorrhage [129, 130]. Early detection, classification and diagnosis of ICH is essential to reduce brain injury which often leads to motor (e.g., cerebral palsy), visual or cognitive dysfunction [120, 133, 134].

Definitive diagnosis of ICH is made by detection of blood in CSF, which requires lumbar puncture, which is not used in neonates as a standard of care. Ultrasound imaging can detect large sub-ependymal, intracerebral, subdural, and epidural hematomas, which are usually accompanied by clinical symptoms of neurological deficit. CT is very sensitive to detection of blood in the brain, but is not ideal because of the ionizing radiation. MRI is very expensive and cumbersome. Both CT and MRI require sedation of neonates during the imaging procedure as well as for transportation from neonatal ward (or NICU) to the imaging center and back, which is complicated and costly as well.

Current standard of care for hemorrhage detection is ultrasound, which is often inconclusive and requires neuroradiological MRI in preterm neonates. MRI is a complicated procedure, requiring neonatal sedation (anesthesia), transportation from and to neonatal ward, which brings the cost of each study to about \$3500/each. The proposed TFMPI technology is planned to be a point-of-care diagnostic device, which can be implemented as early as in the delivery room or in the neonatal ward (or intensive care unit). The estimated cost of procedure is similar to the cost of conventional ultrasound, between \$100 and \$200, including physician's interpretation. Therefore, this technology should be cost-effective from the healthcare economics perspective, especially considering how much will be saved if future health complications of various ICHs will be prevented by early interventions, which otherwise are not implemented due to asymptomatic hemorrhages during the early post-natal period. Therefore, potential market for this technology is almost equal to the numbers of births per year in USA and other countries. Another advantage of the new probe is its high chance of acceptance in the clinic with a minimal training required for nurses and physicians. That is because the TFMPI probe can be built with small modifications to an existing ultrasound probe with almost the same look.

We ran a complete illumination optimization procedure, although not implemented due to what was available in the lab. The laser light fluence decay was also comprehensively studied in intralipid-ink phantoms with similar optical properties as those in the brain. Since the scattering characteristics of the brain tissue throughout is not varied so much, considering a single scattering coefficient model can be an acceptable approximation.

To demonstrate the capability of the TFMPI in the NICU, several gelatin phantom and *ex-vivo* experiments were performed. The major use of TFMPI will be in intraparenchymal hemorrhage and blood in CSF detection. The sensitivity of measuring blood using TFMPI was compared to US initially in several phantoms and demonstrated that TFMPI detects hemorrhages even if they have blood with concentrations below 5%. We then injected mixed-brain tissue blood into the brain of a freshly euthanized sheep and confirmed the gelatin phantom results. We also demonstrated that the detection of small hemorrhages below 5mm (the diameter of the top-view cross-section) can significantly be improved by TFMPI compared to US. To demonstrate the capability of the probe in measuring oxygen saturation, we performed phantom experiments and created an environment that is optically similar to the brain tissue. The *ex vivo* experiment was not performed since the control of the oxygenation of the blood in the brain tissue (or in the brain mixed tissue) at different depth was not feasible. With increased signal sensitivity, TFMPI will find wide acceptance and practice by clinical practitioners. TFMPI will more accurately diagnose brain hemorrhages and decrease the overall cost of complications, through detection of micro-hemorrhage and monitoring other post-operative complications. Currently, misdiagnosis leads to more medical procedures which increase expenses and are more invasive [171]. Overall, TFMPI has potential to improve the neonatal brain monitoring techniques that currently exist, leading to improved quality of life for neonates that would otherwise be misdiagnosed by traditional ultrasound imaging.

There are limitations for the current study. A more optimal fiber bundle made of borosilicate glass for light illumination could be chosen; different wavelengths than

570nm could be tested; a more sophisticated illumination scheme could be found; higher sensitivity ultrasound probes could be used; and most importantly the method should be tested *in vivo* in sheep head and then in neonate. Other limitations include limitations caused by the ultrasound transducer used in this study, the ATL/Philips L7-4. Ultrasound imaging will always be limited by the tradeoff between penetration depth and resolution. To increase the resolution, a higher frequency transducer must be used. The higher frequency sound waves are attenuated at shallower depths though. L7-4 transducer operates at a central frequency of 5MHz allowing for a maximum penetration depth of 6.5cm and an axial resolution of  $\sim 400\ \mu\text{m}$ . This depth allows for adequate imaging of full neonatal brains with a resolution that adequately images micro-hemorrhage. The L7-4 has 128 elements of 7mm height and 0.25mm width. A more comprehensive study on the temperature rise on the scalp could be conducted. When looking to apply this modality to the clinic, the effects of the laser radiation must be considered. The laser used is non-ionizing so the primary concern of this modality would be skin effects to the scalp of the newborn. Skin effects are determined by the absorption and scattering coefficients of the tissues at the laser wavelength, the irradiance of the laser beam, duration of the exposure and pulse repetition characteristics, extent of the local vascular flow, and size of the area. The next step would be to utilize the proposed TFMPI probe for live small and large animal fontanelle imaging.

## CHAPTER 5: TOWARD 3-DIMENSIONAL PHOTOACOUSTIC IMAGING FOR IMPROVED HEMORRHAGE DETECTION

Here, we investigate how element number effected reconstruction quality in terms of contrast to noise ratio (CNR) equidistantly spaced around a hemispherical array. We further evaluated image quality amongst multiple reconstruction methods. We experimentally imaged two *in-vitro* phantoms to confirm feasibility of 3D imaging within the hemisphere as well as compare two methods of illumination technique (single fiber overhead versus homogenous fiber bundle). We also implement a continuous sequential algorithm for element spatial placement optimization within the reconstruction.

### 5.1 Introduction

Among different implementations of PAI, photoacoustic computed tomography (PACT) has characteristics that help its clinical translatability. Some of these characteristics are: (i) deep penetration; compared to all-optical imaging methods such as Functional Near-Infrared Spectroscopy (fNIRS), where in both illumination and detection paths, travelling photons are involved, and compared to use of acoustic detection in PACT which has orders of magnitude smaller signal attenuation, (ii) high frame rate; compared to magnetic resonance imaging (MRI), PACT can generate faster frame-rate volumetric images. Of note that, in the current study, the channel data was averaged many times and worsened the temporal resolution. Ideally, PACTs are developed using high sensitivity transducers and fast repetition-rate (rep-rate) lasers; the frame rate is defined by the rep-rate of the laser or at least one-tenth of that if 10 iterations of acquired signals are averaged at each channel. The ability of PACT systems to render 3D volumetric images, i.e., 3D-PACT, relies on covering angles to



which the acoustic waves are traveling to [172]. Such an imaging configuration will produce adequate channel data for image reconstruction because reconstruction algorithms are developed based on the assumption that the entire imaging target is surrounded by transducers [173, 174]. 3D-PACT has been studied for volumetric mammography, neuroimaging in small animal, and human neonates [7, 146, 174-180].

As for ultrasound detection implementation, one way to perform 3D imaging is to use a 2D ultrasound matrix array [181]. However, these arrays consist of many ultrasonic transducer elements, significantly increasing the system's complexity and cost [181]. A cost-effective alternative method for 3D imaging is to use a linear array and stack multiple cross-sectional images; this method causes motion artifacts and usually it is not time efficient [182, 183]. Apart from 2D arrays, expensive arc-shaped [184, 185] or circular ring arrays [186-188] along with some mechanical translations have also been used for 3D-PACT; these acoustic detection configurations have not been optimized for the best temporal resolution and/or spatial resolution.

As for light illumination, an overhead illumination using a single large optical fiber or a full-field illumination using a fiber bundle, have been studied [28, 189, 190]. We have previously shown in [191, 192] that full-field illumination provides a more homogenous and deeper illumination than overhead illumination; using full-field illumination, we have access to a larger illumination area, and according to the literature [193], the larger the area of illumination, the more light we can couple to the tissue. This issue is of paramount importance especially in the areas of brain and breast imaging where there is a need for a large amount of fluence inside the tissue, to be maintained below the tissue damage threshold.

Different 3D photoacoustic imaging systems with their detection and illumination characteristics as well as their applications are listed in Table 10. In the 3D-PACT systems given in Table 10, it can be seen that either a costly transducer array is used that has not solved the problem of limited detection view completely, or spatially equidistant low-cost single element transducers have been used with non-uniform light illumination techniques.

**Table 10. Different 3D PA signal detection configuration.**

Authors	Configuration (Element no.)	Illumination configuration	Application	Ref
Ephrat, P., <i>et al.</i>	Spherically sparse array (15)	Center illumination from bottom guided by mirror	Imaging moving phantoms	[194]
Xiang, Liangzhong, <i>et al</i>	Spherical array (192)	Cylindrically- shaped guided by fiber bundle	Monitoring needle- based drug delivery, Monitoring hemodynamic changes, and temperature variation	[195]
Dean-Ben <i>et al</i>	Spherical array (256)	Custom-made optical fiber bundle through central opening	Measuring hemodynamic and oxygen parameters	[179]
Tang, Jianbo, <i>et al.</i>	2D rectangular array (3x64)	Center illumination from top using liquid light guide (LLG)	Measuring hemodynamic responses in the primary visual cortex	[196]
Xia, Jun, <i>et al</i>	Linear array scanning (512)	Center illumination guided by fiber bundle	Hair phantom and an <i>ex vivo</i> mouse embryo imaging	[197]
Gateau, Jérôme, <i>et al</i>	Linear array rotate/ translate scanning (128)	Side illumination using fiber bundle	<i>In-vitro</i>	[198]
Wang, Yu, <i>et al</i>	2D matrix array (50x50)	Top illumination using fiber	Mapping of the sentinel lymph	[174]

		bundle	node in rat model	
Wygant, I. O., <i>et al.</i>	2D CMUT array (synthetic aperture: 64x64)	Side illumination using diffuser	Phantom study	[199]

In this section, we demonstrate the feasibility of a stationary 3D hemispherical array PACT (HA-PACT) imaging system using 50 single element transducers with a full-field illumination scheme produced by a distributed optical fiber bundle. 3D HA-PACT mitigates the limited detection view problem by using the hemispherical ultrasound detection, and improves the penetration depth by increasing the signal-to-noise level of the detected signal utilizing a full-field illumination scheme.

For implementation, initially we performed a simulation study with parameters, close to those in practice, to determine the relationship between the number of transducer elements and the quality of the reconstructed image. We then used the greatest number of transducers possible on the hemisphere surface, and evaluated the performance of the resultant imaging system with two different illumination configurations, i.e., overhead and full-field illuminations, to image different imaging targets.

## 5.2 Materials and methods

In this section, initially, different number of elements in the hemispherical array and corresponding reconstructed images are simulated using k-wave toolbox in MATLAB to justify the use of maximum packing of transducers into the hemisphere. This was done to determine if a reduced number of transducers, below maximal packing method, would achieve satisfactory image quality. Next, the experimental setup and phantom preparation are explained, followed by a description of an image quality assessment protocol. The performance of different image reconstruction algorithms

were evaluated on the simulation data. The phantom study was mainly designed to assess the performance parameters of the 3D HA-PACT and optimize the light illumination and the image reconstruction algorithm.

### **5.2.1 Simulation study**

To understand the relation between the quality of the reconstructed images and number of transducers in the 3D HA-PACT, we have modeled a hemispherical cap in k-wave toolbox [102]. The diameter of the hemisphere was chosen to be 12cm based on the consideration of neonatal brain imaging as a potential application of the proposed system. Typically, the neonatal head circumference is between 20 cm to 35 cm [200]; we chose the maximum diameter and considered room for a thin layer of coupling medium inside the hemisphere. Based on the diameter of transducer and the thickness of the designed hemisphere, 50 transducers are the maximum number that can be placed. Any further number of transducers would result in hollow space overlap in the hemisphere model. Additionally, we have simulated 14, 26, 38, and 50 equidistant transducer elements on the hemisphere, and measured the quality of the reconstructed image. We modeled directivity, frequency range, size and the arrangement of transducers in our simulations. In all the above configurations, transducers with a diameter of 12.7mm, frequency of 3.5MHz, 63% -6dB fractional bandwidth, with an equidistant fashion from each other, center to center, were used. The reason that the transducers used in the simulations were 3.5MHz (lower than what was used in the experiment, i.e., 5MHz and 63% bandwidth) was because we did not have sufficient computational power to run the simulations with spatial sampling below the Nyquist limit. The difference between the simulation and experimental setup will not affect the

justification of using the maximum number of transducer on the hemisphere, because the presented results show relative difference in different number of transducers; using a higher frequency transducers will only improve the resolution of the resultant image. To model element size of the transducers, each point transducer was expanded to a neighborhood of 4000 omnidirectional point transducers to mimic the size of 12.7mm diameter. Transducer directivity was realized using spatial averaging on the surface of each single element transducer consistent of the 4000 point transducers. To place the transducers equidistant, we used the algorithm presented in [201]. The algorithm for the equidistant placement of transducers on a surface of the hemisphere was derived by first plotting a 2D curve of  $n$  points where the coordinates are determined using:

$(x, y) = \left( s \cdot a, \pi/2 \times \text{signum}(s) \times \left( 1 - \sqrt{1 - |s|} \right) \right)$  where  $s$  can be ranged from  $-1 + 1/(n-1)$  to  $-1 - 1/(n-1)$  in steps of  $(2 - 2/(n-1))/(n-1)$ ,  $a = 0.1 + 1.2n$ , and signum is a function that determines the sign of  $s$ . These 2D cartesian points are then converted into 3D Cartesian points using  $(x', y', z') = \{ \cos(x) \cos(y), \sin(x) \cos(y), \cos(y) \sin(y) \}$ .

The arrangement of the highest number (50) of equidistant elements on the hemisphere is shown in Figure 38A.

For generation of simulation data in a hemisphere with a diameter of 12cm, a k-wave volume of 12x12x12cm<sup>3</sup> was created using 750x750x750 voxels with 160μm width in every direction. Our simulation provides two spatial samples per wavelength and meets Nyquist's limit. Since k-wave is a pseudospectral method, for a completely accurate simulation it requires at least 10 grid points per wavelength, which is beyond our computational power. We, therefore, inspected the contrast to noise ratio (CNR) of

reconstructions of a simple triangle phantom with differing grid-sizes (i.e., 300x300x300, 400x400x400, 500x500x500, 750x750x750 voxels). CNR was calculated based on the formula provided in [85], as the absolute value of the difference between the average object and background pixels divided by the square root of the sum of the variances of the object and background pixels. Areas of greater signal with visually well-defined boundaries of the imaging target were chosen to be object pixels. Background area was chosen near the boundary of the reconstruction where object was known to not exist. From least-dense to most-dense grid-size, the CNR values were found to be: 1.07, 1.38, 1.44, and 1.45. From the result of negligible difference in CNR with further increasing grid-size and simplicity in our simulated environment (no scatterers) as well as maximal use of our computational power, our use of 750x750x750 voxels grid-size is justified. For the simulation study, an imaging target consisting of 3 thin orthogonal rectangular legs with length of 1cm and width of 2mm each, was defined in k-Wave simulation [102] as shown in Figure 38A. The simulated object is similar to the imaging target that we used in the experiments. The initial pressure was set to 10Pa and sampling frequency was set to 50MHz, same as what was used in the experiment.

Image reconstruction is a process through which transducer signals are transformed into an image. Our reconstruction volume for both simulation and experimental data was 3x3x3cm<sup>3</sup> made up of 400x400x400 voxels with 75μm width in every direction. Different beamformers treat transducer signals differently to generate an image [202]; some of them are simple to implement such as delay-and-sum (DAS), some are very accurate and exact such as universal back projection (UBP), and some are more robust to noise and artifacts such as delay-multiply-and-sum (DMAS). DAS is

the most commonly used beamforming method. It is popular due to its simplicity and that it can be used to reconstruct both US and PA images which is ideal for commercial products [86, 91, 203]. DAS is a blind beamforming method which treats all the detected pressure waves the same way. Mathematically, DAS is the simplified version of the UBP algorithm at which only the first term is used to backproject (see equation 20 in [90]); UBP algorithm is the exact time-domain back-projection method, as illustrated in [90]. The different frequencies accompanying UBP in Figure 38C are the cut-off frequencies of the filter used in UBP. This filter is utilized to mitigate the effects of the amplified noise by the ramp filter existing in UBP formula. In DAS, sidelobes of the radiation pattern of the US transducers affect the image quality. To suppress the effects of sidelobes and off-axis signals, coherence factor (CF) (defined as the ratio of the coherent and incoherent summation of the recorded signals [204]) can be used along with DAS, we call that DAS-CF. CF is an index to show focusing quality and works based on the ratio of mainlobe energy to the total energy.

While DAS, UBP and filtered back projection follow a general delay and sum procedure, Delay-multiply-and-sum (DMAS) is another beamforming method outperforming DAS in the terms of resolution and contrast that uses a correlation process between the received signals [204]. It should be noticed that all these algorithms are based on an ideal point transducer element with an infinite angular view. Figure 38C, demonstrates the performance of different reconstruction algorithms including DAS, DAS-CF, DMAS, and UBP with multiple cutoff frequencies in terms of CNR of the simulated imaging target consisting of 3 thin orthogonal rectangular legs with 50 transducer elements.

DMAS [204] algorithm was chosen in this study for image reconstruction because it provided images with the highest CNR. DMAS algorithm has several variations, we implemented fast DMAS following the method described in [205]. DMAS is conceived from the traditional DAS at which the detected signals are delayed proportional to the distance between the imaging target and the position of the elements. Summation of the delayed signal intensities is then performed, and an image is reconstructed. The equation for DAS, to determine each voxel intensity, is as follows:

$$y_{DAS}(k) = \sum_{i=1}^M x_i(k - \Delta_i) \quad (10)$$

where  $y_{DAS}(k)$  is the output of the beamformer,  $k$  is the time index,  $M$  is the number of elements.  $x_i(k)$  and  $\Delta_i$  are the detected signals and the corresponding time delay for detector  $i$ , respectively. The time delay for each transducer element is equal to the distance between the transducer and the focused imaging pixel (this imaging pixel is specified by time index  $k$ ) and is represented as:

$$\Delta_i = d_i / c \quad (11)$$

DMAS consists of time-shifting radio-frequency (RF) signals of each transducer element to align them in phase (delaying procedure), followed by multiplying and summing them.

DMAS can be represented as:

$$\begin{aligned} y_{DMAS}(k) = & \sum_{i=1}^{M-1} \sum_{j=i+1}^M x_{id}(k) x_{jd}(k) = \\ & \underbrace{[x_{1d}(k)x_{2d}(k) + x_{1d}(k)x_{3d}(k) + \dots + x_{1d}(k)x_{Md}(k)]}_{\text{first term}} + \underbrace{[x_{2d}(k)x_{3d}(k) + x_{2d}(k)x_{4d}(k) + \dots + x_{2d}(k)x_{Md}(k)]}_{\text{second term}} + \\ & \dots + \underbrace{[x_{(M-2)d}(k)x_{(M-1)d}(k) + x_{(M-2)d}(k)x_{Md}(k)]}_{\text{(M-2)th term}} + \underbrace{[x_{(M-1)d}(k)x_{Md}(k)]}_{\text{(M-1)th term}} \end{aligned} \quad (12)$$



where  $x_{id}(k)$  is the delayed signal corresponding to the  $i^{th}$  element of the array. The issue of the squared dimension of the output of equation (12) is also solved using the method introduced in [79].

### 5.2.2 Experimental setup

A Q-switched Nd:YAG laser (Changchun Industries Optoelectronics Tech. Co., Changchun Jilin province, China) with 10Hz, 8.5ns pulse width at 532nm wavelength has been used for illumination purpose. For full-field illumination, 40, 5mm diameter poly-methyl methacrylate (PMMA) (epef-10, Ever Heng Optical Co., Shenzhen, China) optical fibers were bundled into a custom-made aluminum fiber bundle holder and aligned to the laser beam using 1" round top-hat 20° diffuser (EDI-C20-MD, Thorlabs, USA). The overhead illumination was done using a single fiber with a 12mm-diameter, the bundle was removed and a single optical fiber was coupled to the laser.

The integral part of the system is the 3D printed hemisphere cap to hold the distal end of the optical fibers and transducer-amplifier units. Based on the simulation results, we developed this hemispherical dome shaped cap (Fusion 360, v2.0.5688-Year: 2019, USA) with a total of 90 equidistant cylindrically hollow spaces (Figure 38B): 50 for the transducers and 40 for optical fibers. The experimental setup is shown in Figure 39A. The cap has a diameter of 12cm and is made of polyactic acid (PLA). The cap has three holes at the base to hold it in upright position using three horizontal optical rods. These rods are connected to three vertical rods which are fixed to the optical table. Out of 90 hollow spaces, equally spaced 40 smaller holes around the hemisphere are dedicated to fit in the distal end of the 5mm PMMA optical fibers (length: 1.75m, NA: 0.70) for homogeneous illumination (see Figure 39A(ii)). These

holes were left empty when the single fiber (length: 1 m, NA: 0.35) overhead illumination was used, where the fiber was held in place directly above the center of the hemisphere (see Figure 39A(iii)). The other 50 equidistantly located hollow spaces (diameter: 16mm) throughout the cap are dedicated to hold 5MHz single element ultrasound transducers (ISL-0504-GP, Technisonic Research Inc., Connecticut, USA). These transducers are directional and would only provide decent imaging at the center due to the acoustic field overlap they create, as compared to that of focused transducers which is less homogenized but covers a larger field of view. The transducers were connected to low noise 24dB amplifiers (ZFL-500LN, Mini Circuits RF/Microwave Components, Brooklyn, USA) to amplify the raw signals. SMA cables were used to establish connection between transducer-amplifier units and the data acquisition (DAQ) system (NI PXIe-1078, National Instruments, USA). The NI system contains seven 8-channel 14-bit data acquisition cards (NI PXIe-5170R). All 50 transducer-amplifier units were sampled simultaneously with the sampling frequency of 50MHz. 200 frames of data were collected and averaged for SNR improvement, at each transducer location with a total acquisition time of 20s; considering that the laser repetition rate was 10Hz. The trigger management for the laser and DAQ unit synchronization was done in Labview. System specification details are provided in Table 11.

**Table 11. 3D HA-PACT System specification.**

<b>Parameter</b>	<b>Value</b>
Hemisphere radius	6cm
Transducer active aperture / number	12.7mm/ 50
Optical fiber diameter/ number – full-field illumination	5mm/ 40
Optical fiber numerical aperture – full-field illumination	0.70
Optical fiber diameter/ number – overhead	12mm/ 1

illumination	
Optical fiber numerical aperture – overhead	0.35
illumination	

To prepare the phantom, the hemisphere was held in place with the imaging target held by a 90° rod holder (RA90, ThorLabs, NJ, USA) inside the space of the hemisphere. Two objects were constructed for imaging, (1) triangle: an equilateral triangular shape with 2cm leg length (Figure 39B(i)), and (2) four leg: pyramid shape (without base) of 1.5cm leg length using 2mm diameter copper wire soldered together (Figure 39B(ii)). All copper rods were covered in black tape as an absorbing coating. The inner surface of the hemisphere was covered with transparent (both optically and acoustically) saran wrap (uBoxes, USA). We used a multibeam swept-source optical coherence tomography system (SS-OCT) (VivoSight, Michelson Diagnostic™ Inc., United Kingdom) and measured the thickness of the saran wrap to be 40μm [206]. The result is shown in Figure 39A(i). Next, 8% gelatin solution in distilled water was poured into the hemisphere and cured at room temperature. The transducer sensing surfaces were coated in ultrasound gel before placing into assigned positions in contact with the saran wrap.

Finally, based on the transducer diameter and central frequency, the target object in the hemisphere is within the near-field. Imaging within the near-field results in rapid oscillation in received pressure with distance away from the transducer. We have accounted for this oscillation by recording the received pressure profile by imaging a thin lead (with the diameter of 500 microns) from a distance of 4.5 to 7.5cm in 100μm increments and recording the PA signal. We used a digital moving stage (Applied Scientific Instrumentation, OR, USA) which travelled at 1mm/s during acquisition. A

complementary weighting profile was then constructed from the near-field profile for compensation. This experiment was repeated 10 times to reach sufficient precision. This profile was interpolated and applied to the raw data before reconstruction. It is possible to remove this step by utilizing highly focused transducers that have very short focal length.

## **5.3 Results**

### **5.3.1 Simulation results**

The simulated object was reconstructed and the reconstructed images using different number of equidistant transducers, i.e., 14, 26, 38, and 50, are shown in Figure 38D. The quality of the reconstructed images as a function of number of elements was quantitatively assessed by evaluating the CNR of the images, the results are given in Figure 38E. Additionally, we present a square root function fit to demonstrate the change in CNR with increasing number of elements. As defined previously, CNR was calculated using the square root of the sum of the variances of the object pixels and background pixels. Therefore, it was assumed that CNR was proportional to the square root of the number of elements in the system. Results of Figure 38E promoted the use of the maximum number of elements that can fit on the surface of the 12cm diameter hemisphere.

For light illumination we evaluated two configurations: (i) single fiber overhead illumination, in which a single large optical fiber was used on top of the sample and illuminated the entire sample, and (ii) full-field illumination using a bundled optical fiber, in which 40 optical fibers were uniformly distributed on the residual space between the transducer holes in the designed hemisphere using the same algorithm described in

[201]. This method was designed based on the fact that the larger the area of illumination, the more light we will be able to couple to the tissue [193]. The 3D projection model of the hemisphere showing the transducer and optical fiber locations are shown in Figure 38B. The fluence map of the two configurations are visualized using 3DSlicer software (Brigham and Women's Hospital, Harvard Medical School, USA) and presented in Figure 38F. The simulations were performed using Zemax. The parameters considered in the Zemax simulations are as follows: 1,000,000 rays, 10mJ input energy for both configurations, NA for the full field and overhead illuminations were 0.70 and 0.35 respectively, and diameters for the full field fibers and overhead fiber was 5mm and 12mm respectively. As shown in Figure 38F(i,ii), the full-field illumination configuration provides a more homogenous illumination with higher optical energy compared to single fiber illumination. We quantitatively compared these fluence maps within a sphere of 2cm diameter right above the center of the cap, where the imaging target is located at. The average fluence and standard deviation for the full-field illumination within this sphere were 0.038 and 0.003, while those were 0.078 and 0.01 for overhead illumination, which suggests a less homogeneous illumination by the overhead configuration and consequently lower quality images.

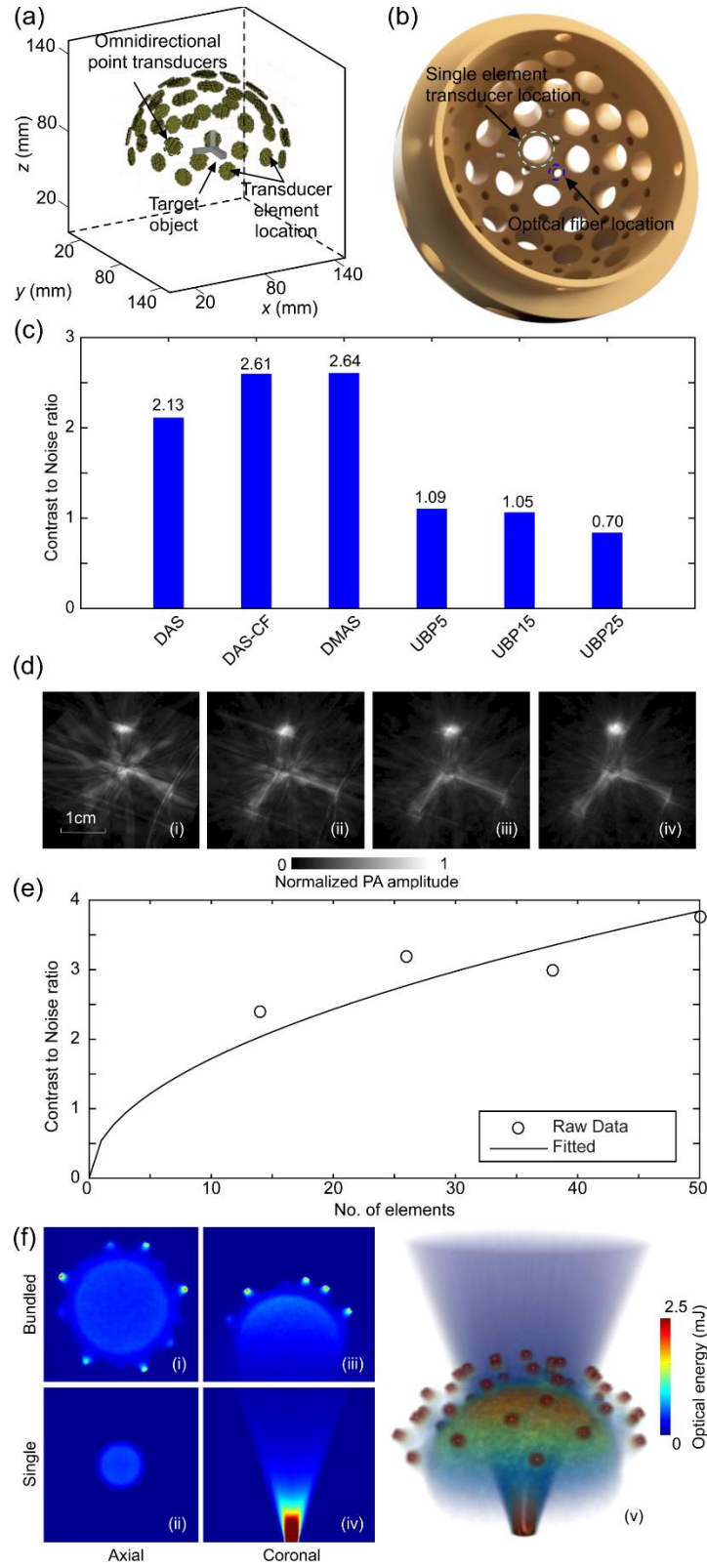


**Figure 38. Hemispherical simulation results.** (a) Simulated configuration of 50 equidistant transducers on a 12cm diameter hemisphere using k-Wave toolbox for

imaging a 3-leg phantom, (b) bottom view of the 3D model of 50 element hemisphere cap using Fusion 360 software, (c) image quality assessment in terms of contrast to noise ratio when different image reconstruction algorithms were used for reconstruction of the 3-leg phantom in a 50 element PACT; Delay-and-Sum, Delay-and-Sum Coherence Factor, Delay-Multiply-and-Sum, and Universal Back Projection with 5, 15, and 25MHz cutoff frequencies, (d) (i-iv) reconstructed images using 14, 26, 38, and 50 equidistant 12.7mm transducers; for image reconstruction DMAS algorithm was used, (e) quantitative evaluation of reconstructed images in terms of contrast to noise ratio with square root function fit, (f) fluence map of full-field and overhead configurations in axial (i-ii), and coronal plane (iii-iv), and (v) comparison of fluence homogeneity for full-field and overhead configurations.

### 5.3.2 Experimental results

Experimental setup of the data acquisition is shown in Figure 39A demonstrating our two methods of illumination: (ii) full-field illumination and (iii) single fiber overhead illumination. Fast DMAS reconstruction algorithm was used for image reconstruction with the near-field compensation curve applied prior. We demonstrated in Figure 39B that full-field illumination (v-vi) has significantly improved the reconstruction compared to overhead illumination (Figure 39B(vii-viii)). Simulated target object has also been reconstructed for comparison purpose as shown in Figure 39B(iii-iv). The main reason was that a more homogeneous fluence map was generated by full-field illumination compared to overhead illumination. CNR of the reconstructed images using both methods on two imaging targets were quantified, they are given in Figure 39C. As expected, the full-field illumination yielded improved image quality due to the even deposition of optical energy around the imaging target, thus a uniform initial induced pressure. The absolute CNRs were calculated for experimental images. For the triangle-shaped phantom, CNR of the image generated by the full-field illumination is 3.2 times greater than that generated by the overhead illumination. For the pyramid-shaped

phantom, the improvement is 1.6 times. In terms of spatial resolution, the developed system was able to reconstruct objects to be as close as 0.9 mm to each other.

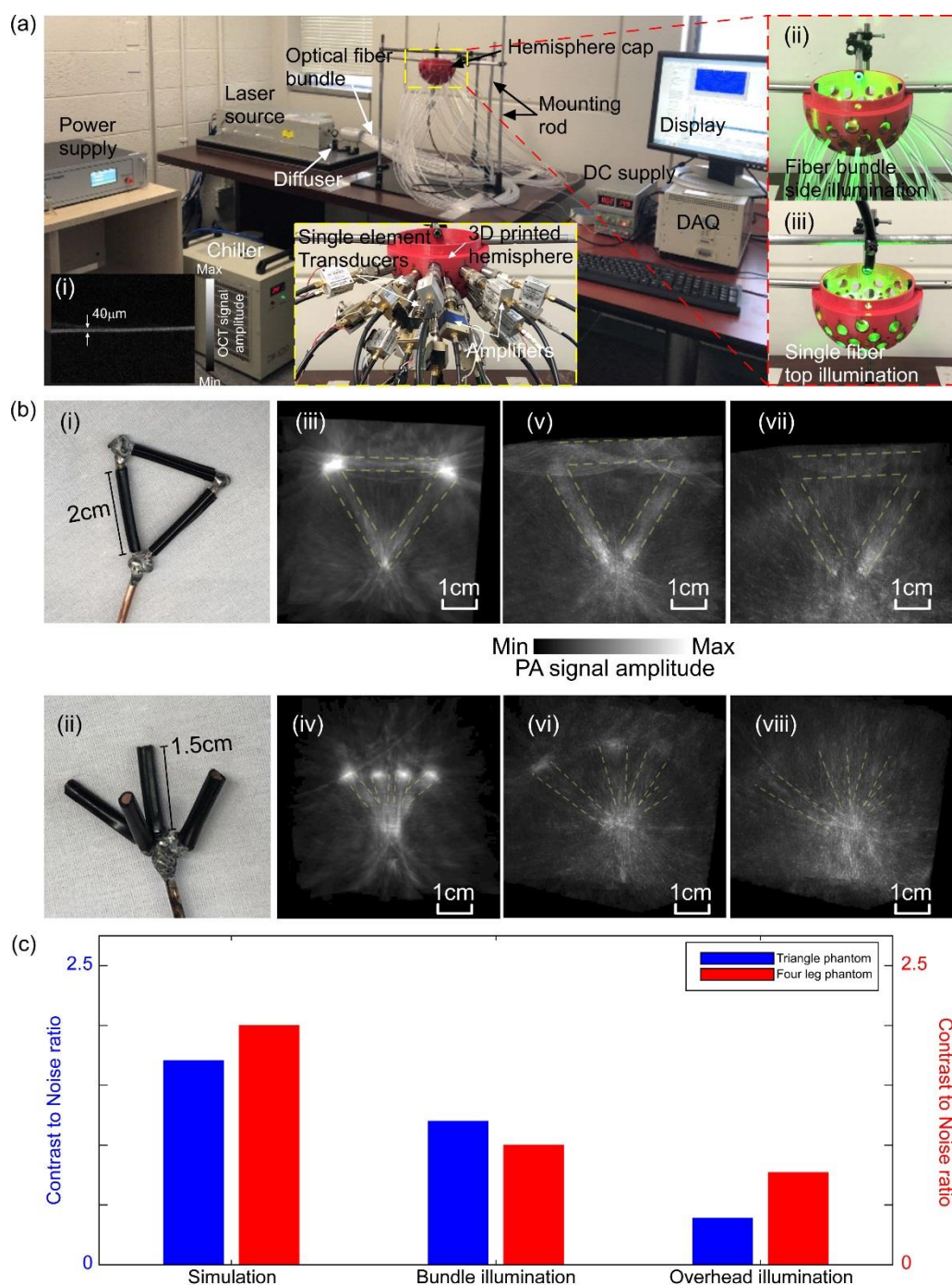


**Figure 39. Hemispherical experimental results.** (a) Experimental setup, (i) measurement of saran wrap thickness using OCT imaging system, (ii) full-field illumination, and (iii) overhead illumination, (b) two imaging targets used in



experimental configuration: photograph of (i) triangle phantom, (ii) four leg phantom, (iii, iv) simulation results of triangle and four leg phantoms, (v, vi) full-field illumination reconstruction results, (vii, viii) overhead illumination reconstruction results, and (c) relative values of contrast to noise ratio of the reconstructed images of the triangle (blue) and four leg (red) phantoms.

### 5.3.3 System calibration

Manual placement of the transducers in the hemisphere resulted in small deviations in the distance between each sensing surface and the target. Post-processing was performed to shift the signals of each channel in time domain. Using an optimization algorithm and an appropriate cost function, an automatic calibration can be performed. In this study, we used the continuous sequential (CS) optimization algorithm [207]. According to the Nyquist theorem, the step size should be smaller than half the wavelength. Considering the central frequency of the transducers, i.e., 5 MHz, its bandwidth and the speed of sound of 1500 m/s, an optimization step size of 100  $\mu\text{m}$  is adequate which is equivalent to 3 samples with a 50 MS/s DAQ sampling frequency. Flowchart of the continuous sequential algorithm is shown in Figure 40A. In this optimization algorithm (see Figure 40A), each channel was shifted with an increment of 100 $\mu\text{m}$  to a maximum displacement of 1.5mm forward and 1.5mm backward, creating 31 possible sets of shifted data per channel. These data were then reconstructed using DMAS algorithm. Due to the very large search space, i.e., 3150 combinations and lack of a reference image, an automatic optimization process will take a very long time. Therefore, optimality of channel data shift was determined by the user through visually assessing reduction in background signal and alignment of imaged object features. The best reconstructed image out of 31 for each of the 50 channels was chosen sequentially and corresponding signal shift was stored. The reconstructed image before and after

optimization are shown in Figure 40B(i-ii), and the quantification of the CNR for each volume is shown in Figure 40C. As seen in Figure 40C, CNR was improved by 30% after optimization.

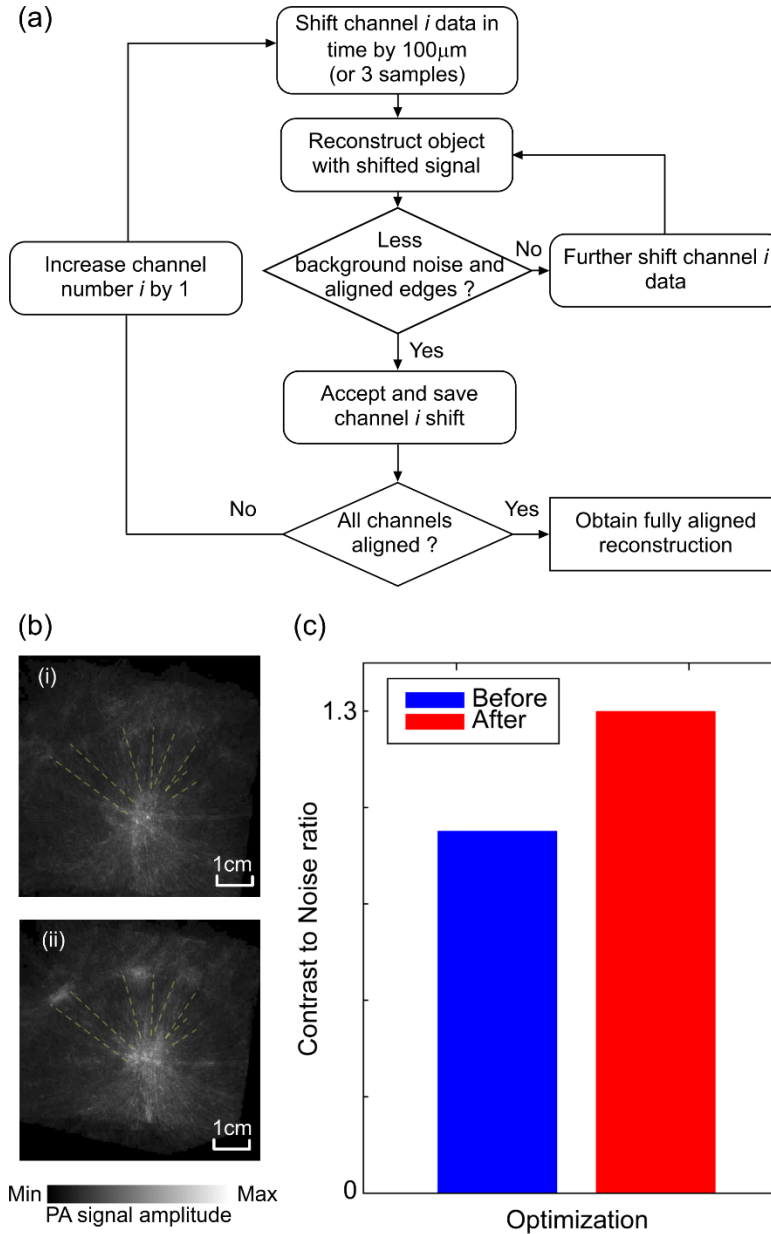


**Figure 40. Optimization of single element spatial location.** (a) Flowchart of the continuous sequential optimization algorithm, (b) reconstructed images of four leg phantom (i) before and (ii) after optimization, (c) bar chart demonstrating increase in the contrast to noise ratio of the reconstructed images before and after optimization.

## 5.4 Discussion and conclusions

Photoacoustic imaging has shown great promise in preclinical studies [1, 17, 28, 55, 146, 208-211]. It has also shown great potential for clinical translatability. Such translation especially for neonatal brain and breast imaging, require an imaging system with a large detection view, fast acquisition and volumetric imaging capability [7, 146, 174-178]. Towards clinical translation, we have tested the feasibility of a stationary 3D HA-PACT imaging system with a full-field illumination scheme. Through quantitative analysis of simulation results, we have demonstrated that using a greater number of transducers in the HA-PACT system results in higher quality images; this was expected as the greater number of view angles will provide the image reconstruction algorithm improved spatial averaging which aids in artifact removal [204]. Therefore, based on the diameter of transducers and the thickness of the designed hemispherical structure, 50 single element transducers are the maximum amount that can be placed on a 12cm diameter hemispherical dome. Although the physical increase in the number of transducers is limited by the space on the hemisphere, we ran a series of simulations (Figure 41(A-B)) to show that using a greater number of transducers with smaller size improve the CNR as shown in Figure 41C. Such configuration can be implemented using either smaller transducers or the same size transducers with a rotating scheme.

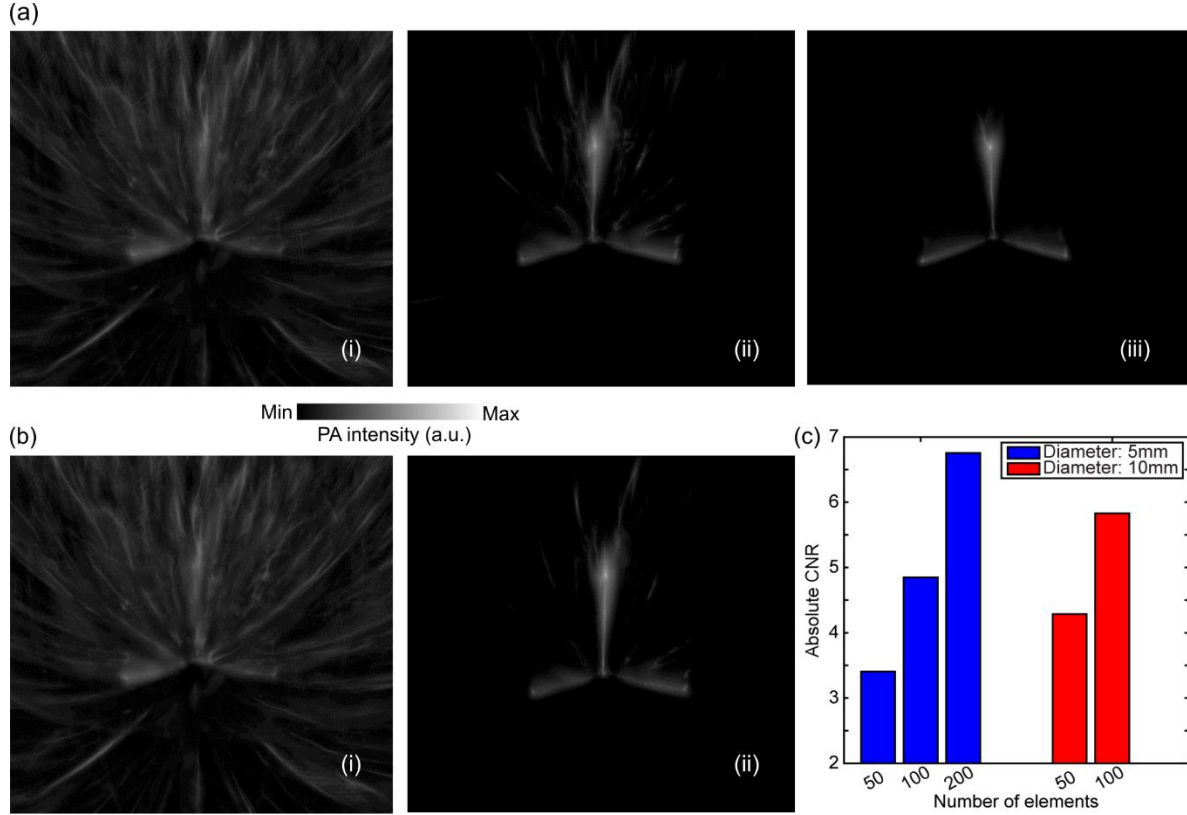


**Figure 41. Other simulations of varying number and sized transducer elements on reconstruction quality.** Simulated reconstruction of three-leg phantom using (a) 5mm diameter active area transducer with (i) 50, (ii) 100, and (iii) 200 elements, (b) 10mm diameter active area transducer with (i) 50, (ii) 100 element, and (c) absolute contrast to noise ratio of different numbers of elements with 5 and 10mm diameter transducer.

We tested two illumination configurations, full-field illumination and single fiber overhead illumination. Our experimental results (shown in Figure 39) demonstrated that the proposed homogeneous illumination outperforms the traditional overhead illumination. This was mainly because the overhead illumination is not providing uniform deposition of optical energy, especially on the underside of the objects where they are directly in the field of view of the transducer elements. This inadequate illumination induced a deteriorated signal at the propagation angle to the elements and, therefore, worsened the reconstructed image quality. According to the literature [193], the larger the area of illumination, the more light we can couple to the tissue. This justifies the use

of the entire area of the hemisphere and placement of fibers in an equidistant fashion on it.

Table 12 provides an estimated cost to develop the proposed system. The overall cost of the proposed hemispherical system is approximately \$42K. Other PACT systems such as the one developed by Upputuri et al costs \$15K using rotation of one single element and that by [212] that has used a ring array cost over \$100K.

**Table 12. Estimated cost of the proposed system.**

Parameter	Specifications	Cost (\$)
Transducers	50 single elements / 512 elements	~15K / ~65K
Amplifiers	Low-noise 24dB / customized	~7.5K / ~25K
DAQ	56 channel / 512 channel (or 64 channel with MUX)	~20K / ~50K

Our preliminary design was a proof of concept to investigate the feasibility of 3D imaging using single element transducers, in which we did not use the most optimum transducers in terms of size, type and sensitivity. The laser repetition rate was not optimum either. Our end goal is to develop a real-time 3D imaging system that is capable of hemodynamic imaging. One way to improve the proposed design is to rotate the hemisphere; such design will maintain inexpensive hardware, but virtually increase the number of view angles and hence dramatically improve the quality of the reconstructed image [213, 214]. Utilizing a laser with a rep-rate of 200 Hz with 20 rotation steps and 10 frame acquisition per step for averaging will allow for 1Hz frame rate full volume imaging, which will satisfy the hemodynamic imaging requirement [186].

We demonstrated (see Figure 38C), that implementation of a more sophisticated reconstruction algorithm, improved the quality of the reconstructed image [215]. This is because reconstruction methods such as DAS, UBP, and filtered back projection follow a general delay-and-sum procedure. These algorithms are based on an ideal point transducer element with an infinite angular view. Whereas more sophisticated algorithms such as the ones presented in [216-220] consider a more realistic acoustic field for the transducers in the image reconstruction process. Further, it is possible to utilize a speed of sound map in the reconstruction of the imaging targets, especially in biological tissue, and use iterative image reconstruction algorithms [214] for further improvement of the reconstructed images.

In regards to optimization, utilizing optimization methods such as simulated annealing algorithm, or Genetic algorithm along with an effective cost function will allow an automated and more effective calibration [207, 221-227].

In this chapter, we have developed a stationary 3D Hemispherical Array Photoacoustic Imaging System using 50 single element transducers. The performance of the system on several phantoms, using two light illumination configurations, i.e. overhead and full-field illumination, with different image reconstruction algorithms, were evaluated. CNR of the images were used for quantitative analysis of the results. DMAS reconstruction algorithm with full-field illumination produced the images with the best quality and quantitative results. In the future, utilizing techniques to increase the number of view angles for ultrasonic detection, a more sophisticated image reconstruction algorithm considering the speed of sound map of the biological tissue, and a fluence compensation algorithm will be explored.

## CHAPTER 6: CONCLUSIONS AND FUTURE WORK

### 6.1 Conclusions

To conclude, we have aimed to develop novel PAI systems towards the end of clinical translation for neonatal brain hemorrhage detection. We evaluated a common preclinical US hardware (Verasonics Vantage 128) for utility in PAI as well as explained methods of data processing and image reconstruction. We investigated PAI safety in a mouse model. We then designed and implemented a transFontanelle multispectral photoacoustic imaging (TFMPI) device for intracranial hemorrhage detection. We finally developed a stationary hemispherical array photoacoustic computed tomography (HA-PACT) system toward 3D neonatal brain hemorrhage detection. The major contributions that this dissertation provides, as outlined earlier, are:

- **Verasonics Vantage system comprehensive review.** Here, we precisely define all aspects of implementing a photoacoustic imaging linear array system in Verasonics architecture, a common preclinical photoacoustic imaging platform. This includes hardware and software discussion. Experimental design is discussed with a myriad of considerations – laser synchronization, frame averaging, illumination angle onto sample, display methods, US beam steering for improving reconstruction, 3<sup>rd</sup> party PA amplifier hardware for improving sensitivity, fluence compensation, and water as a PA couplant. We then characterized one of our systems and discuss image reconstruction.
- **Photoacoustic thermal Safety assessment.** Here, we evaluate thermal safety of photoacoustic imaging on mouse model. We briefly discuss a bio-heat transfer model. Thermal damage of irradiated spot was assessed by histology following

biopsy for different pulse repetition rate lasers (10Hz and 30Hz) for different durations (20s, 60s, 300s). Efficacy of using cooling bag during laser irradiation for improved thermal damage result was evaluated. Results of skin temperature increase throughout irradiation is compared to simulation.

- Development of TransFontanelle Multi-spectral Photoacoustic Imaging (TFMPI) probe for neonatal hemorrhage detection.** Here, we discuss linear array TFMPI probe development including light delivery optimization through optical simulation. We investigated fluence decay estimation of blood at various imaging depths. We characterize our probe for resolution throughout the imaging window. Experimentally we determine the sensitivity of PA to low blood concentrations compared to US to demonstrate sensitivity to detecting hemorrhage. We then create an intraventricular hemorrhage model in *ex-vivo* sheep head and demonstrated ability of detection. Finally, we demonstrate ability to differentiate edematous regions from hemorrhage through use of exogenous contrast agent Evan's Blue.
- 3D hemispherical array photoacoustic computed tomography (HA-PACT).** Here, we investigated how element number effected reconstruction quality in terms of contrast to noise ratio (CNR) equidistantly spaced around a hemispherical array. We further evaluated image quality amongst multiple reconstruction methods. We experimentally imaged two *in-vitro* phantoms to confirm feasibility of 3D imaging within the hemisphere as well as compare two methods of illumination technique (single fiber overhead versus homogenous



fiber bundle). We also implement a continuous sequential algorithm for element spatial placement optimization within the reconstruction.

## 6.2 Future Work

Despite the comprehensive work provided by this dissertation, there is much to be done to translate PAI to the clinic, especially toward intracranial hemorrhage detection. There includes much to be continued within the projects performed within this dissertation. Specifically, my understanding of the future work needed includes:

- **PAI system design:** Within design of PAI systems there is always the need for improved portability. The Verasonics system utilized in this dissertation for much data acquisition is bulky and would be more accepted in the clinic with reduced size and weight. In addition, the mechanism by which PA can be detected can have improved sensitivity through an all optical method. This may also improve complex coupling problems such as with our HA-PACT design.
- **Thermal safety of PAI:** To fully evaluate the safety of PAI toward utility in human clinical setting, there is a much higher degree of certainty needed. Therefore, there must be a much greater number of samples irradiated for different durations, pulse repetition rates, energy per pulse, and at different wavelengths. Simulation can provide an expectation for what will occur in an experimental setting, but the experimental evaluation must occur.
- **TFMPI evaluation:** This work has clearly shown the ability to fill a clinical need with TFMPI. Still, we must continue to test the device in more realistic situations. This includes live, large animal studies with realistic pathology. A large animal hemorrhage and edema IACUC protocol must be developed for TFMPI testing.

Further, optimization in illumination configuration can be performed to improve illumination to brain tissue.

**3D HA-PACT:** Our design of the 3D HA-PACT, had many limitations including: limited number of view angles for ultrasonic detection, lack of inclusion of speed of sound map of the biological tissue, and no fluence compensation component. To improve this method of imaging, a rotating arc or spiral design for transducer arrangement will allow for a completely filled volume of field of view. This will allow for keeping the number of elements low and therefore also the cost of the DAQ, but still virtually increase the number of view angles.

**APPENDIX**

American National Standards Institute	ANSI
Blood gas analyzer	BGA
Blood-oxygen-level dependent	BOLD
Cerebrospinal fluid	CSF
Coherence factor	CF
Computed tomography	CT
Continuous sequential	CS
Contrast to noise ratio	CNR
Cumulative equivalent minutes at 43°C	CEM43°C
Data acquisition	DAQ
Delay-and-sum	DAS
Delay-multiply-and-sum	DMAS
Deoxy-hemoglobin	HbR
Division of Laboratory Animal Resources	DLAR
Double-stage Delay-multiply-and-sum	DS-DMAS
Fast Fourier transform	FFT
Full width at half maximum	FWHM
Functional near infrared spectroscopy	fNIRS
Germinal matrix hemorrhage	GMH
Graphical user interface	GUI
Half width at half max	HWHM
Hardware abstraction layer	HAL

Hemispherical-array photoacoustic computed tomography	HA-PACT
Infrared	IR
Institutional Animal Care and Use Committee	IACUC
Intracranial hemorrhage	ICH
Intraparenchymal hemorrhage	IPH
Intraventricular hemorrhage	IVH
Liquid light guide	LLG
Magnetic resonance imaging	MRI
Maximum permissible level of exposure	MPLE
Minimum variance	MV
Monte Carlo	MC
Near infrared spectroscopy	NIRS
Neodymium-doped yttrium aluminum garnet	Nd:YAG
Neonatal intensive care unit	NICU
One-dimensional	2D
Optical parametric oscillator	OPO
Oxygen saturation	SO <sub>2</sub>
Oxy-hemoglobin	HbO
Photoacoustic	PA
Photoacoustic computed tomography	PACT
Photoacoustic imaging	PAI
Polyactic acid	PLA
Poly-methyl methacrylate	PMMA

Positron emission tomography	PET
Radio frequency	RF
Region of interest	ROI
Signal to noise ratio	SNR
Subarachnoid hemorrhage	SAH
Sub-ependymal hemorrhage	SEH
Superior sagittal sinus	SSS
Swept-source optical coherence tomography	SS-OCT
Three-dimensional	3D
Time gain compensation	TGC
Transfontanelle multispectral photoacoustic imaging	TFMPI
Transfontanelle ultrasound imaging	TFUSI
Transmit power controller	TPC
Two-dimensional	2D
Ultrasound	US
Universal back projection	UBP

## REFERENCES

1. Zhou, Y., J. Yao, and L.V. Wang, *Tutorial on photoacoustic tomography*. Journal of biomedical optics, 2016. **21**(6): p. 061007.
2. Pan, D., et al., *A brief account of nanoparticle contrast agents for photoacoustic imaging*. Wiley Interdisciplinary Reviews: Nanomedicine and Nanobiotechnology, 2013. **5**(6): p. 517-543.
3. Kim, C., C. Favazza, and L.V. Wang, *In vivo photoacoustic tomography of chemicals: high-resolution functional and molecular optical imaging at new depths*. Chemical reviews, 2010. **110**(5): p. 2756-2782.
4. Li, C. and L.V. Wang, *Photoacoustic tomography and sensing in biomedicine*. Physics in medicine and biology, 2009. **54**(19): p. R59-R97.
5. Kratkiewicz, K., et al., *Development of a Stationary 3D Photoacoustic Imaging System Using Sparse Single-Element Transducers: Phantom Study*. Applied Sciences, 2019. **9**(21): p. 4505.
6. Wang, L.V., *Tutorial on photoacoustic microscopy and computed tomography*. IEEE Journal of Selected Topics in Quantum Electronics, 2008. **14**(1): p. 171-179.
7. Kruger, R.A., et al., *Dedicated 3D photoacoustic breast imaging*. Medical physics, 2013. **40**(11).
8. Ku, G. and L.V. Wang, *Deeply penetrating photoacoustic tomography in biological tissues enhanced with an optical contrast agent*. Optics letters, 2005. **30**(5): p. 507-509.

9. Chitgupi, U., et al., *Surfactant-Stripped Micelles for NIR-II Photoacoustic Imaging through 12 cm of Breast Tissue and Whole Human Breasts*. *Advanced Materials*, 2019: p. 1902279.
10. Zhang, H.F., et al., *Functional photoacoustic microscopy for high-resolution and noninvasive in vivo imaging*. *Nature biotechnology*, 2006. **24**(7): p. 848.
11. Mallidi, S., G.P. Luke, and S. Emelianov, *Photoacoustic imaging in cancer detection, diagnosis, and treatment guidance*. *Trends in biotechnology*, 2011. **29**(5): p. 213-221.
12. Yang, S., et al., *Functional imaging of cerebrovascular activities in small animals using high-resolution photoacoustic tomography*. *Medical physics*, 2007. **34**(8): p. 3294-3301.
13. Gamelin, J., et al., *A real-time photoacoustic tomography system for small animals*. *Optics express*, 2009. **17**(13): p. 10489-10498.
14. Zhang, E., et al., *In vivo high-resolution 3D photoacoustic imaging of superficial vascular anatomy*. *Physics in medicine and biology*, 2009. **54**(4): p. 1035.
15. Brecht, H.-P., et al., *Whole-body three-dimensional optoacoustic tomography system for small animals*. *Journal of biomedical optics*, 2009. **14**(6): p. 064007-064007-8.
16. Wang, L.V. and S. Hu, *Photoacoustic tomography: in vivo imaging from organelles to organs*. *Science*, 2012. **335**(6075): p. 1458-1462.
17. Zhang, E.Z., J. Laufer, and P. Beard. *Three-dimensional photoacoustic imaging of vascular anatomy in small animals using an optical detection system*. in

- Biomedical Optics (BiOS) 2007*. 2007. International Society for Optics and Photonics.
18. Wang, X., et al., *Noninvasive laser-induced photoacoustic tomography for structural and functional in vivo imaging of the brain*. Nature biotechnology, 2003. **21**(7): p. 803-806.
  19. Li, C., et al., *Real-time photoacoustic tomography of cortical hemodynamics in small animals*. Journal of biomedical optics, 2010. **15**(1): p. 010509-010509-3.
  20. Lu, W., et al., *Photoacoustic imaging of living mouse brain vasculature using hollow gold nanospheres*. Biomaterials, 2010. **31**(9): p. 2617-2626.
  21. Laufer, J., et al., *In vivo preclinical photoacoustic imaging of tumor vasculature development and therapy*. Journal of biomedical optics, 2012. **17**(5): p. 0560161-0560168.
  22. Sethuraman, S., et al., *Spectroscopic intravascular photoacoustic imaging to differentiate atherosclerotic plaques*. Optics express, 2008. **16**(5): p. 3362-3367.
  23. Wang, B., et al., *Intravascular photoacoustic imaging*. IEEE Journal of selected topics in Quantum Electronics, 2010. **16**(3): p. 588-599.
  24. Sethuraman, S., et al., *Intravascular photoacoustic imaging using an IVUS imaging catheter*. IEEE transactions on ultrasonics, ferroelectrics, and frequency control, 2007. **54**(5): p. 978-986.
  25. Hu, S., et al., *Functional transcranial brain imaging by optical-resolution photoacoustic microscopy*. Journal of biomedical optics, 2009. **14**(4): p. 040503-040503-3.



26. Wang, X., et al., *Noninvasive imaging of hemoglobin concentration and oxygenation in the rat brain using high-resolution photoacoustic tomography*. Journal of biomedical optics, 2006. **11**(2): p. 024015.
27. Ku, G., et al., *Imaging of tumor angiogenesis in rat brains in vivo by photoacoustic tomography*. Applied Optics, 2005. **44**(5): p. 770-775.
28. Zafar, M., et al., *Development of Low-Cost Fast Photoacoustic Computed Tomography: System Characterization and Phantom Study*. Applied Sciences, 2019. **9**(3): p. 374.
29. Kratkiewicz, K., et al., *Photoacoustic/Ultrasound/Optical Coherence Tomography Evaluation of Melanoma Lesion and Healthy Skin in a Swine Model*. Sensors, 2019. **19**(12): p. 2815.
30. Zhang, E.Z., et al., *Multimodal photoacoustic and optical coherence tomography scanner using an all optical detection scheme for 3D morphological skin imaging*. Biomedical optics express, 2011. **2**(8): p. 2202-2215.
31. Chen, Z., et al., *Non-invasive multimodal optical coherence and photoacoustic tomography for human skin imaging*. Scientific Reports, 2017. **7**(1): p. 17975.
32. Xu, D., et al., *Noninvasive and high-resolving photoacoustic dermoscopy of human skin*. Biomedical optics express, 2016. **7**(6): p. 2095-2102.
33. Li, M., et al., *Simultaneous Molecular and Hypoxia Imaging of Brain Tumors In Vivo Using Spectroscopic Photoacoustic Tomography*. Proceedings of the IEEE, 2008. **96**(3): p. 481-489.
34. Nie, L., et al., *Photoacoustic tomography through a whole adult human skull with a photon recycler*. Journal of biomedical optics, 2012. **17**(11): p. 110506-110506.

35. Ermilov, S.A., et al., *Laser optoacoustic imaging system for detection of breast cancer*. Journal of biomedical optics, 2009. **14**(2): p. 024007-024007-14.
36. Copland, J.A., et al., *Bioconjugated gold nanoparticles as a molecular based contrast agent: implications for imaging of deep tumors using optoacoustic tomography*. Molecular Imaging & Biology, 2004. **6**(5): p. 341-349.
37. Manohar, S., et al., *Initial results of in vivo non-invasive cancer imaging in the human breast using near-infrared photoacoustics*. Optics express, 2007. **15**(19): p. 12277-12285.
38. Oraevsky, A.A., et al. *Laser optoacoustic imaging of breast cancer in vivo*. in *BiOS 2001 The International Symposium on Biomedical Optics*. 2001. International Society for Optics and Photonics.
39. Hu, S., et al., *Label-free photoacoustic ophthalmic angiography*. Optics letters, 2010. **35**(1): p. 1-3.
40. Jiao, S., et al., *Photoacoustic ophthalmoscopy for in vivo retinal imaging*. Optics express, 2010. **18**(4): p. 3967-3972.
41. Wang, B., et al., *Detection of lipid in atherosclerotic vessels using ultrasound-guided spectroscopic intravascular photoacoustic imaging*. Optics express, 2010. **18**(5): p. 4889-4897.
42. Jansen, K., et al., *Lipid detection in atherosclerotic human coronaries by spectroscopic intravascular photoacoustic imaging*. Optics Express, 2013. **21**(18): p. 21472-21484.

43. Deng, Y., et al., *Ultrasonic Shear Wave Elasticity Imaging Sequencing and Data Processing Using a Verasonics Research Scanner*. IEEE transactions on ultrasonics, ferroelectrics, and frequency control, 2017. **64**(1): p. 164-176.
44. Xia, J., *Case Study: Photoacoustic Imaging of Hand Vasculature Using the Verasonics Vantage system*. 2019, Verasonics Inc.: Verasonics Inc.
45. Freudenrich, C., *How ultrasound works*. How Stuff Works, 2001. **22**.
46. Feldman, Y., et al., *Dielectric Relaxation Phenomena in Complex Materials*. Advances in chemical physics, 2006. **133**(A): p. 1.
47. Pennes, H., *Analysis of tissue and arterial blood temperature in the resting human forearm*. Int. J. Radiation Oncology Biol. Phys., 1948. **25**: p. 289-297.
48. Cole, R.W., T. Jinadasa, and C.M. Brown, *Measuring and interpreting point spread functions to determine confocal microscope resolution and ensure quality control*. Nature protocols, 2011. **6**(12): p. 1929.
49. Blanton, H., *Transducers*.
50. Ivanov, V., *Analog White Paper*, K. Kratkiewicz, Editor. 2018, PhotoSound Technologies Inc: PhotoSound Technologies Inc. p. 20.
51. Yuan, Z. and H. Jiang, *Quantitative photoacoustic tomography: Recovery of optical absorption coefficient maps of heterogeneous media*. Applied physics letters, 2006. **88**(23): p. 231101.
52. Arridge, S.R., *Optical tomography in medical imaging*. Inverse problems, 1999. **15**(2): p. R41.

53. Paulsen, K.D. and H. Jiang, *Spatially varying optical property reconstruction using a finite element diffusion equation approximation*. Medical Physics, 1995. **22**(6): p. 691-701.
54. Prahl, S. *Mie Scattering Calculator*. 2018 [cited 2019; Available from: [https://omlc.org/calc/mie\\_calc.html](https://omlc.org/calc/mie_calc.html)].
55. Zhao, L., et al., *Optical fluence compensation for handheld photoacoustic probe: An in vivo human study case*. Journal of Innovative Optical Health Sciences, 2017. **10**(04): p. 1740002.
56. Fang, Q. and D.A. Boas, *Monte Carlo simulation of photon migration in 3D turbid media accelerated by graphics processing units*. Optics express, 2009. **17**(22): p. 20178-20190.
57. Nyholt, J. and G.N. Langlois, *Dry-coupled permanently installed ultrasonic sensor linear array*. 2013, Google Patents.
58. Curcio, J.A. and C.C. Petty, *The near infrared absorption spectrum of liquid water*. JOSA, 1951. **41**(5): p. 302-304.
59. Matcher, S., M. Cope, and D. Delpy, *Use of the water absorption spectrum to quantify tissue chromophore concentration changes in near-infrared spectroscopy*. Physics in Medicine & Biology, 1994. **39**(1): p. 177.
60. Sogandares, F.M. and E.S. Fry, *Absorption spectrum (340–640 nm) of pure water. I. Photothermal measurements*. Applied Optics, 1997. **36**(33): p. 8699-8709.

61. Chung, S., et al., *Non-invasive tissue temperature measurements based on quantitative diffuse optical spectroscopy (DOS) of water*. Physics in Medicine & Biology, 2010. **55**(13): p. 3753.
62. Bakhsheshi, M.F. and T.-Y. Lee, *Non-invasive monitoring of brain temperature by near-infrared spectroscopy*. 2015, Taylor & Francis.
63. Tam, A. and C. Patel, *Optical absorptions of light and heavy water by laser optoacoustic spectroscopy*. Applied Optics, 1979. **18**(19): p. 3348-3358.
64. Sullivan, S.A., *Experimental study of the absorption in distilled water, artificial sea water, and heavy water in the visible region of the spectrum*. JOSA, 1963. **53**(8): p. 962-968.
65. Abran, M., et al., *Development of a photoacoustic, ultrasound and fluorescence imaging catheter for the study of atherosclerotic plaque*. IEEE transactions on biomedical circuits and systems, 2014. **8**(5): p. 696-703.
66. Harrison, T. and R.J. Zemp, *The applicability of ultrasound dynamic receive beamformers to photoacoustic imaging*. IEEE transactions on ultrasonics, ferroelectrics, and frequency control, 2011. **58**(10).
67. Kim, J., et al., *Programmable real-time clinical photoacoustic and ultrasound imaging system*. Scientific reports, 2016. **6**: p. 35137.
68. Mercep, E., et al., *Hybrid optoacoustic tomography and pulse-echo ultrasonography using concave arrays*. IEEE transactions on ultrasonics, ferroelectrics, and frequency control, 2015. **62**(9): p. 1651-1661.

69. Mozaffarzadeh, M., et al., *Double-stage delay multiply and sum beamforming algorithm applied to ultrasound medical imaging*. Ultrasound in medicine & biology, 2018. **44**(3): p. 677-686.
70. Sivasubramanian, K., V. Periyasamy, and M. Pramanik, *Non-invasive sentinel lymph node mapping and needle guidance using clinical handheld photoacoustic imaging system in small animal*. Journal of biophotonics, 2018. **11**(1): p. e201700061.
71. Taruttis, A. and V. Ntziachristos, *Advances in real-time multispectral optoacoustic imaging and its applications*. Nature Photonics, 2015. **9**(4): p. 219.
72. Wei, C.-W., et al., *Real-time integrated photoacoustic and ultrasound (PAUS) imaging system to guide interventional procedures: ex vivo study*. IEEE transactions on ultrasonics, ferroelectrics, and frequency control, 2015. **62**(2): p. 319-328.
73. Mozaffarzadeh, M., et al., *Enhanced contrast acoustic-resolution photoacoustic microscopy using double-stage delay-multiply-and-sum beamformer for vasculature imaging*. Journal of biophotonics, 2019. **12**(11): p. e201900133.
74. Karaman, M., P.-C. Li, and M. O'Donnell, *Synthetic aperture imaging for small scale systems*. IEEE transactions on ultrasonics, ferroelectrics, and frequency control, 1995. **42**(3): p. 429-442.
75. Chen, M.-C., et al., *A pixel pitch-matched ultrasound receiver for 3-D photoacoustic imaging with integrated delta-sigma beamformer in 28-nm UTBB FD-SOI*. IEEE Journal of Solid-State Circuits, 2017. **52**(11): p. 2843-2856.

76. Park, S., et al., *Adaptive beamforming for photoacoustic imaging*. Optics letters, 2008. **33**(12): p. 1291-1293.
77. Synnevag, J.F., A. Austeng, and S. Holm, *Adaptive beamforming applied to medical ultrasound imaging*. IEEE transactions on ultrasonics, ferroelectrics, and frequency control, 2007. **54**(8).
78. Wagner, N., Y.C. Eldar, and Z. Friedman, *Compressed beamforming in ultrasound imaging*. IEEE Transactions on Signal Processing, 2012. **60**(9): p. 4643-4657.
79. Matrone, G., et al., *The delay multiply and sum beamforming algorithm in ultrasound B-mode medical imaging*. IEEE transactions on medical imaging, 2015. **34**(4): p. 940-949.
80. Paridar, R., et al., *Validation of Delay-Multiply-and-Standard-Deviation Weighting Factor for Improved Photoacoustic Imaging of Sentinel Lymph Node*. Journal of biophotonics, 2018: p. e201800292.
81. Asl, B.M. and A. Mahloojifar, *A low-complexity adaptive beamformer for ultrasound imaging using structured covariance matrix*. IEEE transactions on ultrasonics, ferroelectrics, and frequency control, 2012. **59**(4).
82. Bae, M., S.B. Park, and S.J. Kwon, *Fast minimum variance beamforming based on Legendre polynomials*. IEEE transactions on ultrasonics, ferroelectrics, and frequency control, 2016. **63**(9): p. 1422-1431.
83. Mehdizadeh, S., et al., *Minimum variance beamforming applied to ultrasound imaging with a partially shaded aperture*. IEEE transactions on ultrasonics, ferroelectrics, and frequency control, 2012. **59**(4).

84. Mozaffarzadeh, M., A. Mahloojifar, and M. Orooji. *Medical photoacoustic beamforming using minimum variance-based delay multiply and sum*. in *Digital Optical Technologies 2017*. 2017. International Society for Optics and Photonics.
85. Mozaffarzadeh, M., et al., *Double-stage delay multiply and sum beamforming algorithm: Application to linear-array photoacoustic imaging*. IEEE Transactions on Biomedical Engineering, 2018. **65**(1): p. 31-42.
86. Mozaffarzadeh, M., et al., *Linear-array photoacoustic imaging using minimum variance-based delay multiply and sum adaptive beamforming algorithm*. Journal of biomedical optics, 2018. **23**(2): p. 026002.
87. Rabinovich, A., A. Feuer, and Z. Friedman, *Multi-line transmission combined with minimum variance beamforming in medical ultrasound imaging*. IEEE transactions on ultrasonics, ferroelectrics, and frequency control, 2015. **62**(5): p. 814-827.
88. Synnevag, J.-F., A. Austeng, and S. Holm, *Benefits of minimum-variance beamforming in medical ultrasound imaging*. IEEE transactions on ultrasonics, ferroelectrics, and frequency control, 2009. **56**(9).
89. Mozaffarzadeh, M., et al., *Eigenspace-based minimum variance combined with delay multiply and sum beamformer: Application to linear-array photoacoustic imaging*. IEEE Journal of Selected Topics in Quantum Electronics, 2019. **25**(1): p. 1-8.
90. Xu, M. and L.V. Wang, *Universal back-projection algorithm for photoacoustic computed tomography*. Physical Review E, 2005. **71**(1): p. 016706.



91. Yin, B., et al., *Fast photoacoustic imaging system based on 320-element linear transducer array*. Physics in Medicine & Biology, 2004. **49**(7): p. 1339.
92. Park, J., et al., *Delay-multiply-and-sum-based synthetic aperture focusing in photoacoustic microscopy*. Journal of biomedical optics, 2016. **21**(3): p. 036010.
93. Szabo, T.L. and P.A. Lewin, *Ultrasound transducer selection in clinical imaging practice*. Journal of Ultrasound in Medicine, 2013. **32**(4): p. 573-582.
94. Angelsen, B.A., et al., *Which transducer array is best?* European Journal of Ultrasound, 1995. **2**(2): p. 151-164.
95. Lund, D.J. *The co-evolution of the ANSI Z136. 1 standard for safe use of lasers and the underlying bioeffects data base*. in *International Laser Safety Conference*. 2017. Laser Institute of America.
96. Niemz, M.H., *Interaction mechanisms*, in *Laser-Tissue Interactions*. 2002, Springer. p. 45-149.
97. Ma, J., et al., *Thermal damage in three-dimensional vivo bio-tissues induced by moving heat sources in laser therapy*. Scientific reports, 2019. **9**(1): p. 1-13.
98. Mixon, D.G. and W.P. Roach. *A thermal model of laser absorption*. in *Optical Interactions with Tissue and Cells XVIII*. 2007. International Society for Optics and Photonics.
99. Lin, X.E. *Laser pulse heating*. in *Proceedings of the 1999 Particle Accelerator Conference (Cat. No. 99CH36366)*. 1999. IEEE.
100. Nourhashemi, M., M. Mahmoudzadeh, and F. Wallois, *Thermal impact of near-infrared laser in advanced noninvasive optical brain imaging*. Neurophotonics, 2016. **3**(1): p. 015001.

101. Jacques, S.L., *Optical properties of biological tissues: a review*. Physics in Medicine & Biology, 2013. **58**(11): p. R37.
102. Treeby, B.E. and B.T. Cox, *k-Wave: MATLAB toolbox for the simulation and reconstruction of photoacoustic wave fields*. Journal of biomedical optics, 2010. **15**(2): p. 021314.
103. Heron, M., et al., *Annual summary of vital statistics: 2007*. Pediatrics, 2010. **125**(1): p. 4-15.
104. Lekic, T., et al., *Neonatal brain hemorrhage (NBH) of prematurity: translational mechanisms of the vascular-neural network*. Current medicinal chemistry, 2015. **22**(10): p. 1214-1238.
105. Griffiths, R., *The abilities of babies: a study in mental measurement*. 1954.
106. Luiz, D., C. Foxcroft, and R. Stewart, *The construct validity of the Griffiths Scales of Mental Development*. Child: Care, health and development, 2001. **27**(1): p. 73-83.
107. M, L., *Intracranial haemorrhage at term*. 4th ed. Robertson's textbook of neonatology, ed. R. JM. 2005, Philadelphia: Elsevier.
108. Perrin, R.G., et al., *Management and outcomes of posterior fossa subdural hematomas in neonates*. Neurosurgery, 1997. **40**(6): p. 1190-1200.
109. Van Rooij, L.G., et al., *Cardiac arrhythmias in neonates receiving lidocaine as anticonvulsive treatment*. European journal of pediatrics, 2004. **163**(11): p. 637-641.

110. Morgan, T., et al., *Intracranial hemorrhage in infants and children with hereditary hemorrhagic telangiectasia (Osler-Weber-Rendu syndrome)*. Pediatrics, 2002. **109**(1): p. e12-e12.
111. Osterman, M.J., et al., *Annual summary of vital statistics: 2012–2013*. Pediatrics, 2015: p. peds. 2015-0434.
112. Papile, L.-A., et al., *Incidence and evolution of subependymal and intraventricular hemorrhage: a study of infants with birth weights less than 1,500 gm*. The Journal of pediatrics, 1978. **92**(4): p. 529-534.
113. Tsiantos, A., et al., *Intracranial hemorrhage in the prematurely born infant: Timing of clots and evaluation of clinical signs and symptoms*. The Journal of pediatrics, 1974. **85**(6): p. 854-859.
114. Brouwer, A.J., et al., *Intracranial hemorrhage in full-term newborns: a hospital-based cohort study*. Neuroradiology, 2010. **52**(6): p. 567-576.
115. Glass, H.C., et al., *Outcomes for extremely premature infants*. Anesthesia and analgesia, 2015. **120**(6): p. 1337.
116. Lantos, J.D. and D.S. Lauderdale, *What is behind the rising rates of preterm birth in the United States?* Rambam Maimonides medical journal, 2011. **2**(4).
117. Gupta, S.N., A.M. Kechli, and U.S. Kanamalla, *Intracranial hemorrhage in term newborns: management and outcomes*. Pediatric neurology, 2009. **40**(1): p. 1-12.
118. Ou-Yang, M.-C., et al., *Clinical manifestations of symptomatic intracranial hemorrhage in term neonates: 18 years of experience in a medical center*. Pediatrics & Neonatology, 2010. **51**(4): p. 208-213.

119. Michael J. Acarregui, M. *Intracranial Hemorrhage*. Iowa Neonatology Handbook, University of Iowa Stead Family Children's Hospital; Available from: <https://uichildrens.org/health-library/intracranial-hemorrhage>.
120. Tan, A.P., et al., *Intracranial Hemorrhage in Neonates: A review of etiologies, patterns and predicted clinical outcomes*. European Journal of Paediatric Neurology, 2018.
121. Aguilar, M.I. and T.G. Brott, *Update in intracerebral hemorrhage*. The Neurohospitalist, 2011. **1**(3): p. 148-159.
122. Garton, T., et al., *Brain iron overload following intracranial haemorrhage*. Stroke and vascular neurology, 2016. **1**(4): p. 172-184.
123. Bu, Y., et al., *Mechanisms of hydrocephalus after intraventricular haemorrhage in adults*. Stroke and vascular neurology, 2016. **1**(1): p. 23-27.
124. Robinson, S., *Neonatal posthemorrhagic hydrocephalus from prematurity: pathophysiology and current treatment concepts: a review*. Journal of Neurosurgery: Pediatrics, 2012. **9**(3): p. 242-258.
125. Joyce A. Martin, B.E.H., Michelle J.K. Osterman, Anne K. Driscoll, and Patrick Drake, *Births: Final Data for 2016*, U.S.D.O.H.H. SERVICES, Editor. 2018, National Vital Statistics Reports. p. Table I-21.
126. Inder, T.E., J.M. Perlman, and J.J. Volpe, *Chapter 24 - Preterm Intraventricular Hemorrhage/Posthemorrhagic Hydrocephalus*, in *Volpe's Neurology of the Newborn (Sixth Edition)*. 2018, Elsevier. p. 637-698.e21.

127. Joyce A. Martin, B.E.H., Michelle J.K. Osterman, Anne K. Driscoll, and Patrick Drake, *Births: Final Data for 2016*, U.S.D.O.H.H. SERVICES, Editor. 2018, National Vital Statistics Reports. p. Table I-19.
128. Volpe, J.J., *Neurology of the Newborn E-Book*. 2008: Elsevier Health Sciences.
129. McKee, A.C. and D.H. Daneshvar, *The neuropathology of traumatic brain injury*, in *Handbook of clinical neurology*. 2015, Elsevier. p. 45-66.
130. Vieira, R.d.C.A., et al., *Diffuse axonal injury: epidemiology, outcome and associated risk factors*. *Frontiers in neurology*, 2016. **7**: p. 178.
131. Lekic, T., et al., *Neonatal Brain Hemorrhage (NBH) of Prematurity: Translational Mechanisms of the Vascular-Neural Network*. *Current medicinal chemistry*, 2015. **22**(10): p. 1214-1238.
132. Little, J.R., G.A. Blomquist, and R. Ethier, *Intraventricular hemorrhage in adults*. *Surgical neurology*, 1977. **8**(3): p. 143-149.
133. Inder, T.E., J.M. Perlman, and J.J. Volpe, *Intracranial Hemorrhage: Subdural, Subarachnoid, Intraventricular (Term Infant), Miscellaneous*, in *Volpe's Neurology of the Newborn (Sixth Edition)*. 2018, Elsevier. p. 593-622. e7.
134. Uehara, E., et al., *Slow Elevation in Protein C Activity without a PROC Mutation in a Neonate with Intracranial Hemorrhage*. *AJP reports*, 2018. **8**(2): p. e68.
135. Carson, S.C., et al., *Value of sonography in the diagnosis of intracranial hemorrhage and periventricular leukomalacia: a postmortem study of 35 cases*. *American Journal of Neuroradiology*, 1990. **11**(4): p. 677-683.
136. Malaeb, S.N., et al., *Noninvasive monitoring of brain edema after hypoxia in newborn piglets*. *Pediatric research*, 2018. **83**(2): p. 484.

137. Volpe, J.J., et al., *Positron emission tomography in the asphyxiated term newborn: Parasagittal impairment of cerebral blood flow*. Annals of Neurology, 1985. **17**(3): p. 287-296.
138. Hall, R.W. and R.M. Shbarou, *Drugs of Choice for Sedation and Analgesia in the NICU*. Clinics in perinatology, 2009. **36**(1): p. 15-26.
139. Tkach, J.A., et al., *MRI in the Neonatal ICU: Initial Experience Using a Small-Footprint 1.5-T System*. American Journal of Roentgenology, 2013. **202**(1): p. W95-W105.
140. Bucher, H.U., et al., *Comparison between Near Infrared Spectroscopy and <sup>133</sup>Xenon Clearance for Estimation of Cerebral Blood Flow in Critically Ill Preterm Infants*. Pediatric Research, 1993. **33**: p. 56.
141. Edwards, A.D., et al., *COTSIDE MEASUREMENT OF CEREBRAL BLOOD FLOW IN ILL NEWBORN INFANTS BY NEAR INFRARED SPECTROSCOPY*. The Lancet, 1988. **332**(8614): p. 770-771.
142. Shankar P. Gopinath, et al., *Early detection of delayed traumatic intracranial hematomas using near-infrared spectroscopy*. Journal of Neurosurgery, 1995. **83**(3): p. 438-444.
143. Aslin, R.N. and J. Mehler. *Near-infrared spectroscopy for functional studies of brain activity in human infants: promise, prospects, and challenges*. 2005. SPIE.
144. Demene, C., et al., *Functional ultrasound imaging of brain activity in human newborns*. Sci Transl Med, 2017. **9**(411).
145. Yang, J.-M., et al., *Simultaneous functional photoacoustic and ultrasonic endoscopy of internal organs in vivo*. Nature medicine, 2012. **18**(8): p. 1297.

146. Yao, J., et al., *Noninvasive photoacoustic computed tomography of mouse brain metabolism in vivo*. Neuroimage, 2013. **64**: p. 257-266.
147. Bashkatov, A., et al., *Optical properties of human skin, subcutaneous and mucous tissues in the wavelength range from 400 to 2000 nm*. Journal of Physics D: Applied Physics, 2005. **38**(15): p. 2543.
148. Ugryumova, N., S.J. Matcher, and D.P. Attenburrow, *Measurement of bone mineral density via light scattering*. Physics in Medicine & Biology, 2004. **49**(3): p. 469.
149. Sapareto, S.A. and W.C. Dewey, *Thermal dose determination in cancer therapy*. International Journal of Radiation Oncology\* Biology\* Physics, 1984. **10**(6): p. 787-800.
150. Barber, T.W., J.A. Brockway, and L.S. Higgins, *The density of tissues in and about the head*. Acta neurologica Scandinavica, 1970. **46**(1): p. 85-92.
151. Giering, K., I. Lamprecht, and O. Minet. *Specific heat capacities of human and animal tissues*. in *Laser-Tissue Interaction and Tissue Optics*. 1996. International Society for Optics and Photonics.
152. Holmes, K.R., *Thermal properties*. cortex (dog), 2009. **491**: p. 16.
153. Beck, T.J., et al. *Clinical determination of tissue optical properties in vivo by spatially resolved reflectance measurements*. in *European Conference on Biomedical Optics*. 2003. Optical Society of America.
154. Driver, I., C. Lowdell, and D. Ash, *In vivo measurement of the optical interaction coefficients of human tumours at 630 nm*. Physics in Medicine & Biology, 1991. **36**(6): p. 805.

155. Wilson, B., P. Muller, and J. Yanch, *Instrumentation and light dosimetry for intra-operative photodynamic therapy (PDT) of malignant brain tumours*. Physics in Medicine & Biology, 1986. **31**(2): p. 125.
156. Avanaki, M.R., et al., *Quantitative evaluation of scattering in optical coherence tomography skin images using the extended Huygens–Fresnel theorem*. Applied optics, 2013. **52**(8): p. 1574-1580.
157. Wang, X., D.L. Chamberland, and G. Xi, *Noninvasive reflection mode photoacoustic imaging through infant skull toward imaging of neonatal brains*. Journal of neuroscience methods, 2008. **168**(2): p. 412-421.
158. Mallard, C. and Z.S. Vexler, *Modeling ischemia in the immature brain: how translational are animal models?* Stroke, 2015. **46**(10): p. 3006-3011.
159. Stevenson, D.K., et al., *Fetal and neonatal brain injury*. 2017: Cambridge University Press.
160. Williams, C.E., et al., *Outcome after ischemia in the developing sheep brain: an electroencephalographic and histological study*. Annals of neurology, 1992. **31**(1): p. 14-21.
161. Shen, W., J.-H. Pan, and W.-D. Chen, *Comparison of transcranial ultrasound and cranial MRI in evaluations of brain injuries from neonatal asphyxia*. International journal of clinical and experimental medicine, 2015. **8**(10): p. 18319.
162. DiVittorio, R., E.I. Bluth, and M.A. Sullivan, *Deep vein thrombosis: diagnosis of a comon clinical problem*. The Ochsner Journal, 2002. **4**(1): p. 14-17.
163. Karande, G.Y., et al., *Advanced imaging in acute and chronic deep vein thrombosis*. Cardiovascular diagnosis and therapy, 2016. **6**(6): p. 493.



164. Jacobson, O., D.O. Kieseewetter, and X. Chen, *Albumin-binding Evans Blue derivatives for diagnostic imaging and production of long-acting therapeutics*. Bioconjugate chemistry, 2016. **27**(10): p. 2239-2247.
165. Kang, E., et al., *Blood–brain barrier opening to large molecules does not imply blood–brain barrier opening to small ions*. Neurobiology of disease, 2013. **52**: p. 204-218.
166. Saunders, N.R., et al., *Markers for blood-brain barrier integrity: how appropriate is Evans blue in the twenty-first century and what are the alternatives?* Frontiers in neuroscience, 2015. **9**: p. 385.
167. Mohammadi, L., et al. *Skull's acoustic attenuation and dispersion modeling on photoacoustic signal*. in *Photons Plus Ultrasound: Imaging and Sensing 2018*. 2018. International Society for Optics and Photonics.
168. Rayyan Anwar, K.K.a.M.R.N.A., *Photoacoustic Imaging: A Promising Alternative to Transcranial Ultrasound*. Editorial Res J Photonics, 2018. **2**(1).
169. Institute, A.N.S., *American national standard for safe use of lasers*. 2007: Laser Institute of America.
170. Van Rhoon, G.C., et al., *CEM43° C thermal dose thresholds: a potential guide for magnetic resonance radiofrequency exposure levels?* European radiology, 2013. **23**(8): p. 2215-2227.
171. Balogh, E.P., et al., *Overview of Diagnostic Error in Health Care*. 2015.
172. Meimani, N., et al., *A numerical analysis of a semi-dry coupling configuration in photoacoustic computed tomography for infant brain imaging*. Photoacoustics, 2017. **7**: p. 27-35.

173. Beard, P., *Biomedical photoacoustic imaging*. Interface focus, 2011. **1**(4): p. 602-631.
174. Wang, Y., et al., *In vivo three-dimensional photoacoustic imaging based on a clinical matrix array ultrasound probe*. Journal of Biomedical Optics, 2012. **17**(6): p. 061208.
175. Kitai, T., et al., *Photoacoustic mammography: initial clinical results*. Breast Cancer, 2014. **21**(2): p. 146-153.
176. Piras, D., et al., *Photoacoustic imaging of the breast using the twente photoacoustic mammoscope: present status and future perspectives*. IEEE Journal of Selected Topics in Quantum Electronics, 2010. **16**(4): p. 730-739.
177. Nasiriavanaki, M., et al., *High-resolution photoacoustic tomography of resting-state functional connectivity in the mouse brain*. Proceedings of the National Academy of Sciences, 2014. **111**(1): p. 21-26.
178. Nasiriavanaki, M. *Resting-state functional connectivity measurement in the mouse brain using a low cost photoacoustic computed tomography*. in *Frontiers in Optics*. 2016. Optical Society of America.
179. Dean-Ben, X.L. and D. Razansky, *Localization optoacoustic tomography*. Light: Science & Applications, 2018. **7**(4): p. 18004.
180. Mohammadi, L., et al. *Skull's aberration modeling: towards photoacoustic human brain imaging*. in *Photons Plus Ultrasound: Imaging and Sensing 2019*. 2019. International Society for Optics and Photonics.

181. Tan, Y., et al., *Three-dimensional photoacoustic imaging via scanning a one dimensional linear unfocused ultrasound array*. Optics express, 2017. **25**(7): p. 8022-8028.
182. Niederhauser, J.J., et al., *Combined ultrasound and optoacoustic system for real-time high-contrast vascular imaging in vivo*. IEEE transactions on medical imaging, 2005. **24**(4): p. 436-440.
183. Singh, M.K.A., W. Steenbergen, and S. Manohar, *Handheld probe-based dual mode ultrasound/photoacoustics for biomedical imaging*, in *Frontiers in Biophotonics for Translational Medicine*. 2016, Springer. p. 209-247.
184. Dima, A., N.C. Burton, and V. Ntziachristos, *Multispectral optoacoustic tomography at 64, 128, and 256 channels*. Journal of biomedical optics, 2014. **19**(3): p. 036021.
185. Brecht, H.-P.F., et al., *Whole-body three-dimensional optoacoustic tomography system for small animals*. Journal of biomedical optics, 2009. **14**(6): p. 064007.
186. Li, C., et al., *Real-time photoacoustic tomography of cortical hemodynamics in small animals*. Journal of biomedical optics, 2010. **15**(1): p. 010509.
187. Xia, J., et al., *Whole-body ring-shaped confocal photoacoustic computed tomography of small animals in vivo*. Journal of biomedical optics, 2012. **17**(5): p. 050506.
188. Wang, X., et al., *Three-dimensional laser-induced photoacoustic tomography of mouse brain with the skin and skull intact*. Optics letters, 2003. **28**(19): p. 1739-1741.

189. Laufer, J., et al., *In vivo photoacoustic imaging of mouse embryos*. Journal of biomedical optics, 2012. **17**(6): p. 061220.
190. Razansky, D., A. Buehler, and V. Ntziachristos, *Volumetric real-time multispectral optoacoustic tomography of biomarkers*. Nature protocols, 2011. **6**(8): p. 1121.
191. Mahmoodkalayeh, S., et al. *Optimization of light illumination for photoacoustic computed tomography of human infant brain*. in *Photons Plus Ultrasound: Imaging and Sensing 2018*. 2018. International Society for Optics and Photonics.
192. Mahmoodkalayeh, S., M.A. Ansari, and M. Nasiriavanaki. *A new illumination scheme for photoacoustic computed tomography*. in *Photons Plus Ultrasound: Imaging and Sensing 2018*. 2018. International Society for Optics and Photonics.
193. Li, M., et al., *Internal-illumination photoacoustic computed tomography*. Journal of biomedical optics, 2018. **23**(3): p. 030506.
194. Ephrat, P., et al., *Four-dimensional photoacoustic imaging of moving targets*. Optics express, 2008. **16**(26): p. 21570-21581.
195. Xiang, L., et al., *4-D photoacoustic tomography*. Scientific reports, 2013. **3**: p. 1113.
196. Tang, J., et al., *Wearable 3-D photoacoustic tomography for functional brain imaging in behaving rats*. Scientific reports, 2016. **6**: p. 25470.
197. Xia, J., et al., *Three-dimensional photoacoustic tomography based on the focal-line concept*. Journal of biomedical optics, 2011. **16**(9): p. 090505.
198. Gateau, J., et al., *Single-side access, isotropic resolution and multispectral 3D photoacoustic imaging with rotate-translate scanning of ultrasonic detector array*. arXiv preprint arXiv:1501.06931, 2015.

199. Wygant, I., et al. *Photoacoustic imaging using a two-dimensional CMUT array*. in *IEEE Ultrasonics Symposium, 2005*. 2005. IEEE.
200. Freeborn, D., H. Trevino, and L.C. Adler, *Newborn Measurements*, in *Health Encyclopedia*. 2019, University of Rochester Medical Center.
201. Kogan, J., *A New Computationally Efficient Method for Spacing  $n$  Points on a Sphere*. Rose-Hulman Undergraduate Mathematics Journal, 2017. **18**(2): p. 5.
202. Omid, P., et al., *A novel dictionary-based image reconstruction for photoacoustic computed tomography*. Applied Sciences, 2018. **8**(9): p. 1570.
203. Yang, D., et al., *Fast full-view photoacoustic imaging by combined scanning with a linear transducer array*. Optics express, 2007. **15**(23): p. 15566-15575.
204. Mozaffarzadeh, M., et al., *Enhanced linear-array photoacoustic beamforming using modified coherence factor*. Journal of biomedical optics, 2018. **23**(2): p. 026005.
205. Mozaffarzadeh, M., et al., *Efficient nonlinear beamformer based on the root of detected signals for linear-array photoacoustic tomography: application to sentinel lymph node imaging*. Journal of biomedical optics, 2018. **23**(12): p. 121604.
206. Xu, Q., et al., *Swept-Source Optical Coherence Tomography–Supervised Biopsy*. Dermatologic Surgery, 2018. **44**(6): p. 768-775.
207. Fayyaz, Z., et al., *A Comparative Study of Optimization Algorithms for Wavefront Shaping*. Journal of Innovative Optical Health Sciences, 2019.
208. Yao, J., et al., *High-speed label-free functional photoacoustic microscopy of mouse brain in action*. Nature methods, 2015. **12**(5): p. 407.

209. Yao, J. and L.V. Wang, *Photoacoustic brain imaging: from microscopic to macroscopic scales*. Neurophotonics, 2014. **1**(1): p. 011003.
210. Zafar, M., et al. *Photoacoustic signal enhancement using a novel adaptive filtering algorithm*. in *Photons Plus Ultrasound: Imaging and Sensing 2019*. 2019. International Society for Optics and Photonics.
211. Zhang, E., et al., *In vivo high-resolution 3D photoacoustic imaging of superficial vascular anatomy*. Physics in Medicine & Biology, 2009. **54**(4): p. 1035.
212. Upputuri, P.K. and M. Pramanik, *Performance characterization of low-cost, high-speed, portable pulsed laser diode photoacoustic tomography (PLD-PAT) system*. Biomedical optics express, 2015. **6**(10): p. 4118-4129.
213. He, H., et al., *Improving optoacoustic image quality via geometric pixel super-resolution approach*. IEEE transactions on medical imaging, 2015. **35**(3): p. 812-818.
214. Mandal, S., et al., *Optimal self-calibration of tomographic reconstruction parameters in whole-body small animal optoacoustic imaging*. Photoacoustics, 2014. **2**(3): p. 128-136.
215. Mozaffarzadeh, M., et al., *Double Stage Delay Multiply and Sum Beamforming Algorithm: Application to Linear-Array Photoacoustic Imaging*. IEEE Transactions on Biomedical Engineering, 2017. **PP**(99): p. 1-1.
216. Wang, K., et al., *An imaging model incorporating ultrasonic transducer properties for three-dimensional optoacoustic tomography*. IEEE transactions on medical imaging, 2010. **30**(2): p. 203-214.

217. Shao-Hua, W., T. Chao, and L. Xiao-Jun, *Effects of size and arrangement of virtual transducer on photoacoustic tomography*. Chinese Physics B, 2013. **22**(7): p. 074303.
218. Haltmeier, M. and G. Zangerl, *Spatial resolution in photoacoustic tomography: effects of detector size and detector bandwidth*. Inverse Problems, 2010. **26**(12): p. 125002.
219. Drozdov, G. and A. Rosenthal, *Analysis of negatively focused ultrasound detectors in optoacoustic tomography*. IEEE transactions on medical imaging, 2016. **36**(1): p. 301-309.
220. Wang, K. and M.A. Anastasio, *Photoacoustic and thermoacoustic tomography: image formation principles*. Handbook of Mathematical Methods in Imaging, 2015: p. 1081-1116.
221. Fayyaz, Z., et al., *Simulated annealing optimization in wavefront shaping controlled transmission*. Applied optics, 2018. **57**(21): p. 6233-6242.
222. Manwar, R., et al., *An Application of Simulated Annealing in Compensation of Nonlinearity of Scanners*. Applied Sciences, 2019. **9**(8): p. 1655.
223. Fayyaz, Z., et al. *Wavefront shaping using simulated annealing algorithm for focusing light through turbid media*. in *Photons Plus Ultrasound: Imaging and Sensing 2018*. 2018. International Society for Optics and Photonics.
224. Avanaki, M.R.N., et al., *Sensor-less aberration correction in optical imaging systems using blind optimization*. Asia Pacific Optical Sensors Conference. Vol. 8351. 2012: SPIE.

225. Avanaki, M.R.N., A. Bradu, and A. Podoleanu, *Optimization of excitation of fiber Fabry–Perot tunable filters used in swept lasers using a phase-correction method*. Applied Optics, 2017. **56**(12): p. 3378-3382.
226. Avanaki, M.R.N., et al., *Algorithm for Excitation Optimization of Fabry–Pérot Filters Used in Swept Sources*. IEEE Photonics Technology Letters, 2013. **25**(5): p. 472-475.
227. Avanaki, M.R., et al. *Genetic algorithm for optimization of optical systems*. in *2010 18th Iranian Conference on Electrical Engineering*. 2010. IEEE.



**ABSTRACT****DEVELOPMENT OF PHOTOACOUSTIC TOMOGRAPHIC SYSTEMS FOR BRAIN  
HEMORRHAGE DETECTION**

by

**KARL JOHN KRATKIEWICZ****August 2020****Advisor:** Dr. Kamran Avanaki**Major:** Biomedical Engineering**Degree:** Doctor of Philosophy

Preterm neonates (<32 weeks gestational age) and/or with low birth weight (<1500g) are at high risk for intracranial hemorrhage (ICH) with the incidence of 30%-35%. TransFontanelle Ultrasound Imaging (TFUSI) is the routine diagnostic method of diagnosis, yet autopsy findings reveal that conventional TFUSI underdiagnoses ICH in 8–34% of cases. Magnetic Resonance Imaging (MRI), Computed Tomography (CT), Positron Emission Tomography (PET), and Near InfraRed Spectroscopy (NIRS) are other imaging modalities that have potential use in diagnosing intracranial hemorrhage but are not suited for use with patients in the NICU. Therefore, there is a clinical need to develop novel imaging methods for early diagnosis of preterm infant hemorrhage. Improved diagnosis will hasten treatment and potentially limit neurological deficit in the patient.

Photoacoustic imaging (PAI) is an imaging modality which derives its contrast from differences in optical absorption coefficients of tissue through laser irradiation and acoustic detection. Therefore, PAI derives its signal directly from optical absorbers such as blood; the critical component in a hemorrhage. We discuss operation and processing

methods of our Verasonics Vantage system. We then investigate thermal safety of PAI in mouse model for various laser pulse repetitions rates and illumination duration. We then develop two photoacoustic tomographic systems for eventual translation to clinic for hemorrhage detection. One system being a novel TransFontanelle Multispectral Photoacoustic Imaging (TFMPI) probe. The TFMPI probe was developed and tested on, ex-vivo and in-vitro scenarios to demonstrate improved sensitivity over traditional ultrasound. The other being a 3D hemispherical array photoacoustic computed tomography (HA-PACT) system for 3D volumetric imaging of infant brain. The system is designed and tested for feasibility on in-vitro samples.

**AUTOBIOGRAPHICAL STATEMENT**

Karl Kratkiewicz graduated with an M.S. in biomedical engineering from Wayne State University, Detroit, Michigan, in 2018. He also graduated summa cum laude with a B.S. in biomedical physics from the Wayne State University Honors College in 2017. He has been pursuing his Ph.D. in Biomedical Engineering with a research focus in multimodal (ultrasound/ photoacoustic/ elastography) imaging and photoacoustic neonatal brain imaging.